ATOMKI

ANNUAL REPORT

2004

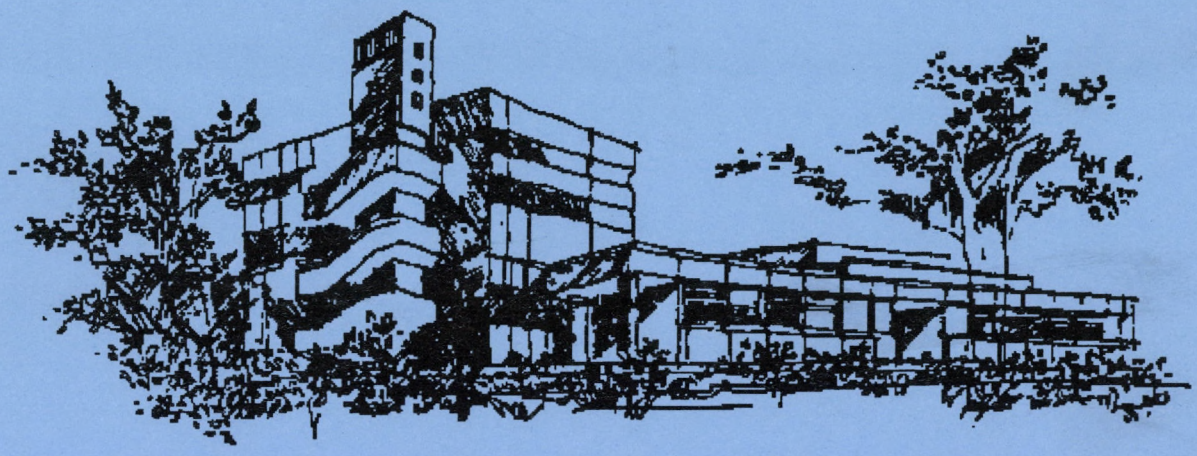

INSTITUTE OF NUCLEAR RESEARCH
OF THE HUNGARIAN ACADEMY OF SCIENCES
DEBRECEN, HUNGARY

INSTITUTE OF NUCLEAR RESEARCH
OF THE HUNGARIAN ACADEMY OF SCIENCES
DEBRECEN, HUNGARY

ANNUAL REPORT
2004

ATOMKI

Postal address:
P.O. Box 51
H-4001 Debrecen,
Hungary

Editor:
I. Rajta

HU ISSN0 0231-3596

Preface

2004 was the semi-centenary year of the foundation of this Institute. The Prefaces to our Annual Reports do usually mention various celebrations, but now the impression of the reader will be that the staff was doing absolutely nothing throughout the year but celebrating themselves. That is actually not quite correct; what explains my enlarging so much upon celebrations and suchlike is that this is the only medium in which we summarise these events for the public and record them for posterity.

We prepared five publications on this occasion. We put together a special number of Fizikai Szemle (edited by Zs. Fülöp), a brochure of the Institute (both in Hungarian and in English, edited by Z. Máté) and a folded album on the 'Radiations from Atomki' in Hungarian (Z. Máté). Finally, we compiled a booklet of stories and anecdotes from the past of the Institute (edited by B. Gyarmati). The really original stuff is of course the last one. The level of the stories is uneven, but most are enjoyable for outsiders as well. The equilibrium between piquancy and modesty is reasonable, and there are a number of stories very characteristic of the times past. Some may be used even as source materials for history in a view-from-the-bottom approach.

We started the celebrations with a scientific meeting on 14th January, which reviewed the research activity of Prof. Dénes Berényi (Director of the Insitute 1976–1989) from β-spectroscopy along surface physics to atomic collisions, on the occasion of his 75th birthday. The three review talks were given by D. Varga, L. Kövér and L. Sarkadi.

The next occasion was the Physics Days in March, the local 'public feast' of physics. The unifying subject was, surpisingly, scientific research in Atomki. This time, exceptionally, the public lectures were given solely by members of Atomki. The titles were the following: *Gigamicroscopes* on giant accelerators by Z. Trócsányi, *Ping-pong Games in Nature* on atomic collisions by B. Sulik, *Buried for Eternity?* on radioactive wastes by É. Svingor and *Creation of Elements* on astrophysical nucleosynthesis by Zs. Fülöp and *Empty, cold, complicated ..., but what for?* on the indirect impacts of physics research by S. Mészáros. Fülöp's talk was an introduction to the debut of the Hungarian version of the Japanese scientific film 'Element Genesis: Solving the Mystery'. The Hungarian adaptation was made here by Fülöp and his colleagues.

The summit of the celebrations was a picnic in May, with the participation of many active and retired members of the Institute. At the Bem tér entrance of the Institute, we set up the skeleton of our old cascade accelerator, which had been dissembled one and a half decade ago. It was inaugurated on this May morning as a public monument or a sculpture of our science. To mark the occasion, we also planted a tree, and what a tree it is! We were presented a Japanese cherry tree (*Sakura tree 'Yoko'*) on this occasion by our sister institution, the Faculty of Science, Niigata University.

The memorial stone erected near the tiny tree bears the following Hungarian and English inscriptions written in the form of haiku:

Japán cseresznye:	Japanese cherry:
nígata–debreceni	a Niigata–Debrecen
közös kísérlet	joint experiment

As is shown by the photos at http://www.atomki.hu/atomki/Kepek/foto.html, the experiment seems successful.

There were two international scientific workshops held in Debrecen during the silver jubilee year: the *IUVSTA Workshop on Electron Scattering in Solids – From Fundamental Concepts*

to Practical Applications (ESS'04), 4–8 June, 2004, and *8th Workshop on Fast Ion–Atom Collisions*, 1–3 September. Partly coinciding with the latter meeting, we had an exhibition of paintings by Kazuko Mukoyama in the Ceremonial Hall of the University of Debrecen. Mrs. Mukoyama is the wife of our old friend and partner scientist, Professor Takeshi Mukoyama. At the opening of the exhibition the artist and her work—traditional Japanese brush painting as well as European style painting—were introduced by myself. To give a feeling for her art, let me put my haiku on her demonstration here:

Mukoyama Kazuko's Art	**Mukoyama Kazuko művészete**
Wind-blown flower-shadows	Repdeső ecset
come to life as the brush is	lengő virágárnyakat
flitting in the void.	kelt a semmiből.

In November we commemorated the deceased members of the Institute, and laid a flower wreath on the grave of the founder, Professor Szalay. A few days later, the Mayor of Debrecen gave a reception in Atomki to the public of the Institute. On this occasion I gave a comprehensive lecture entitled *Life and Science in Atomki.* The commemorative events were concluded by a meeting of the Section of Physical Sciences of the Academy of Sciences, which was held in Atomki. The participants were entertained by talks by members of Atomki: B. Sulik, K. Tőkési, Gy. Gyürky, A. Krasznahorkay, M. Molnár and Z. Berényi, and by guided tours to some laboratories.

Not only Atomki but also CERN celebrated its silver jubilee last year. Atomki contributed to the commemorative event held in Budapest in September by a talk by Z. Trócsányi. The fifth anniversary of the death of Ede Hertelendi, head of the Section of Environmental and Earth Sciences, was marked by a one-day symposium in September, entitled *From the Stone Age to Nuclear Power Stations.* The PET Centre of the University of Debrecen, situated in Atomki, also had a jubilee: it celebrated the 10 year's anniversary of its foundation in November. Members of Atomki contributed to the scientific program of the yearly General Assembly of the Academy by two talks, those by S. Ricz and B. Sulik.

The 'Honours List' was especially long in 2004. Dr. L. Sarkadi won the Academy Award. Young scientists' awards were granted to Dr. Gy. Gyürky and Dr. D. Novák, Jr., by the Academy and by the Institute, respectively. The Szalay Prize of the Institute was received by Dr. S. Ricz, and the Szalay Prize and Selényi Prize of the Roland Eötvös Physical Society were given to Dr. L. Gulyás and Dr. Zs. Fülöp, respectively. Dr. T. Vertse acquired a 'habilitation' title at the University of Debrecen, while Dr. A. Krasznahorkay was decorated with a titular professorship at the University of Szeged. Prof J. Pálinkás was elected an ordinary member of the Academy of Sciences, and I was elected a corresponding member.

The instrumentation of our laboratories has been improved by the installation of two mass spectrometers: a secondary-ion mass spectrometer (SIMS), which is also operated so as to produce secondary neutral atoms (SNMS mode of operation), and a mass spectrometer for measuring isotope ratios of stable isotopes in gas samples. The former is used in thin layer physics, while the latter is used in environmental analyses. Both are owned jointly: the former with the Department of Solid State Physics, University of Debrecen, and the latter with Isotoptech Co.. The laboratory for radiochemistry has been refurbished so as to satisfy the criteria of 'good manufacturing practice' for pharmaceuticals. A major technical improvement is made possible by a grant received last year for the technical updating of the beam lines of the 5-MeV electrostatic accelerator. That project is in the phase of commissioning now.

To show that we did work thoughout the jubilee year as well, I mention a few recent results.

We published our comprehensive study of the nucleus ^{16}C, which is based on our experiments performed at RIKEN (Japan). This nucleus is very interesting since its neutron excess is built upon an oblate ^{12}C core and it populates partly the sd-shell, which usually gives rise to prolate deformation. The first excited state, which is usually a collective 2^+ state, has been studied and found to live extremely long. The behaviour of this state can be explained by assuming that it involves (almost) purely neutron excitation.

As members of the LUNA collaboration, the nuclear astrophysics group contributed to making the age of the Universe more precise. This was done by measurement of the cross section of the reaction ^{14}N(p,γ)^{15}O at extremely low energies. From the results it was concluded that the oldest globular clusters known are slightly older than believed earlier.

The Fermi shuttle mechanism of ionization has been studied for some time by the Debrecen physicists. This mechanism can be visualized as a ping-pong-like multiple scattering of electrons between the nuclei of the colliding atoms, and has been demonstrated to exist by a surplus of high-energy (10–200 eV) electrons. Recent experiments have shown that this mechanism is dominant in the process of ionization induced by slow heavy ions. This mechanism bears on the manner in which biological tissues are being damaged when subjected to irradiation. Since in heavy-ion therapy the cancerous cells are killed mostly by the slowed-down ions, it must be this kind of ionization that is responsible for the major damage, and that calls for further studies of the process.

The radiocarbon group has examined the recently found remains of the first (wooden) bridge over river Tisza, the major river in Eastern Hungary. They found that it had been built in the 16th century. By dating replacement beams, they also established that the bridge must have been in use at least up to the second half of the 18th century.

For the sake of completeness, I mention that my appointment as Director has been prolonged until the end of 2009.

The financial and personnel conditions in 2004 are given in the pie charts to follow this Preface.

This Report, prepared in LaTeX, is available on the web at www.atomki.hu in PDF format.

Debrecen, 11 July 2005

Rezső G. Lovas
Director

Organizational structure of ATOMKI

Director:	R.G. Lovas, corresponding member of the HAS
Deputy directors:	Á.Z. Kiss, D.Sc.
	S. Mészáros, C.Sc.
Finance director:	Dr. M. Pálinkás

- Secretariat (Scientific Secretary: Á. Kovách, C.Sc.)
- Library (Librarian: Mrs. M. Nagy)
- Accounting (Head: Mrs. J. Sass)
- Basic Services and Maintenance (Head: Mr. I. Katona)
- Mechanical Workshop (Head: Mr. I. Gál)

Scientific Sections

Division of Nuclear Physics (Head: J. Cseh, D.Sc.)

- Section of Experimental Nuclear Physics (Head: A. Krasznahorkay, D.Sc.)
- Section of Electrostatic Accelerators (Head: Zs. Fülöp. Ph.D.)
    - Nuclear Astrophysics Group
    - Ion Beam Analysis Group
- Section of Theoretical Physics (Head: T. Vertse, D.Sc.)

Division of Atomic Physics (Head: Á. Kövér, D.Sc.)

- Section of Atomic Collisions (Head: L. Sarkadi, D.Sc.)
- Section of Electron Spectroscopy (Head: D. Varga, C.Sc.)

- Section of Environmental and Earth Sciences (Head: Á.Z. Kiss, D.Sc.)
    - Laboratory of Environmental Studies
    - Radon Group
    - K-Ar Laboratory
    - Radiation- and Environmental Protection Group
    - QMS Laboratory
- DE TTK - ATOMKI Department of Environmental Physics (Head: S. Sudár, C.Sc.)
- Cyclotron Section (Head: F. Tárkányi, C.Sc.)
- Section of Electronics (Head: J. Gál, C.Sc.)

Data on ATOMKI

At present the Institute employs 205 persons. The affiliation of personnel to units of organization and the composition of personnel are given below.

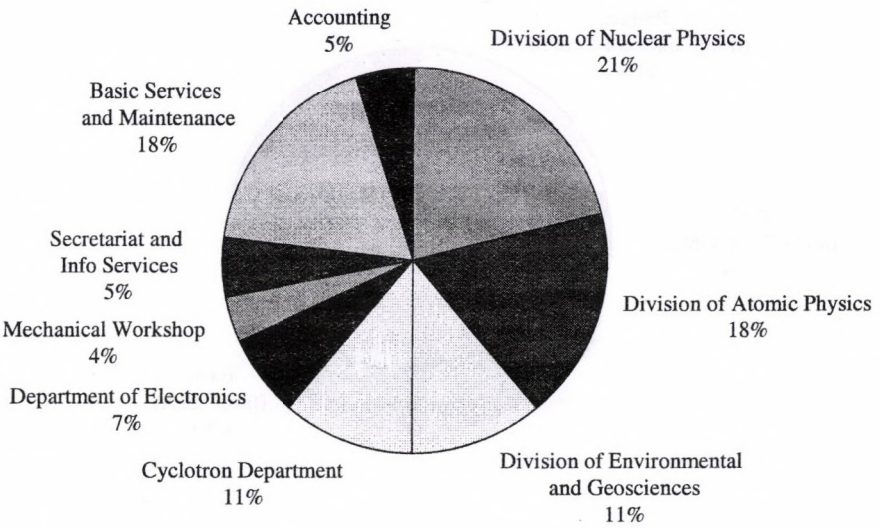

Figure 1. Affiliation of personnel to units of organization

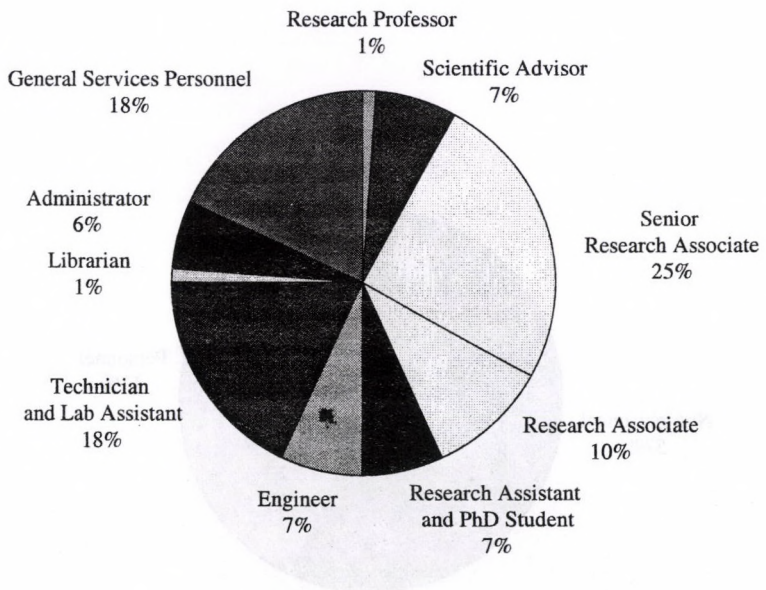

Figure 2. Composition of personnel

Finance

The total budget of the Institute for the year 2004 was 1232 million Hungarian Forints. The composition of the budget and the share of personnel expenditure within the budget are shown below.

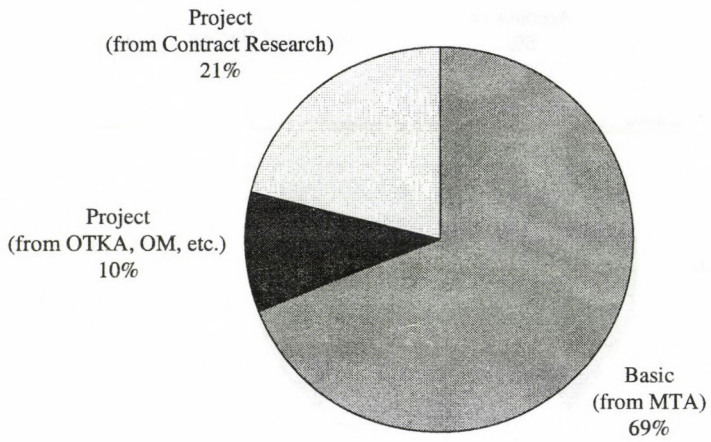

Figure 3. Composition of the budget of the Institute

MTA: Hungarian Academy of Sciences
OTKA: National Fund for Scientific Research
OM: Ministry of Education

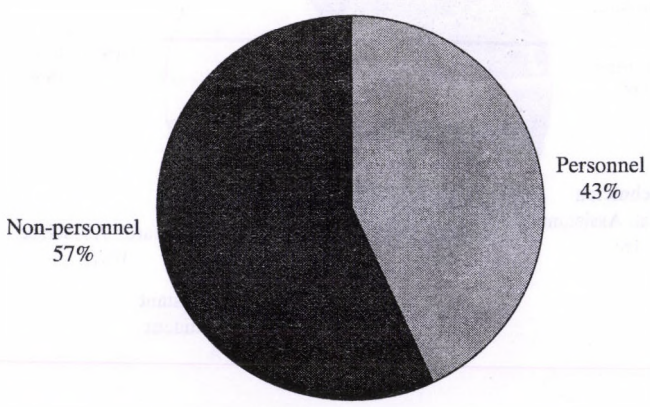

Figure 4. Breakdown of expenditure into personnel and non-personnel expenditures

Table of contents

1.1 General conditions for the $\mathcal{PT}$ symmetry of supersymmetric partner potentials

G. Lévai

A common feature of symmetries of quantum systems is that they restrict the form of the Hamiltonian, and consequently they also influence the structure of the energy spectrum. This is also the case with two symmetry concepts that are typically applied in nonrelativistic quantum mechanics: supersymmetric quantum mechanics (SUSYQM) and $\mathcal{PT}$ symmetry.

SUSYQM connects one-dimensional potentials pairwise via the relation

$$V^{(\pm)}(x) = W^2(x) \pm \frac{\mathrm{d}W}{\mathrm{d}x} + \varepsilon \,, \qquad (1)$$

where ε is the factorization energy, $V^{(-)}(x)$ and $V^{(+)}(x)$ are the SUSY partner potentials, while $W(x)$ is the superpotential. In the simplest case, when supersymmetry is unbroken, $W(x)$ is defined in terms of the ground-state wavefunction of $V^{(-)}(x)$ as $W(x) = -\frac{\mathrm{d}}{\mathrm{d}x} \ln \psi_0^{(-)}(x)$, and the factorization energy is chosen as $\varepsilon = E_0^{(-)}$. Under these conditions the SUSY partner potentials possess the same energy levels, except that $E_0^{(-)}$ is missing from the spectrum of $V^{(+)}(x)$, and the degenerate levels are connected by the SUSY ladder operators $A = \frac{\mathrm{d}}{\mathrm{d}x} + W(x)$ and $A^\dagger = -\frac{\mathrm{d}}{\mathrm{d}x} + W(x)$.

The $\mathcal{PT}$ symmetry of a Hamiltonian prescribes its invariance under *simultaneous* space and time inversion, which boils down to the condition $V(x) = V^*(-x)$ in the case of one-dimensional potentials. The unusual feature of this new symmetry concept is that $\mathcal{PT}$-symmetric potentials are *complex* in general, nevertheless, they possess *real* energy eigenvalues, unless $\mathcal{PT}$ symmetry is spontaneously broken, in which case the energy spectrum consists of complex conjugate energy pairs.

The interplay of these two symmetry concepts has been analyzed in a number of works (see [1] and references), and it has been found that when $V^{(-)}(x)$ has unbroken $\mathcal{PT}$ symmetry, then the same applies to $V^{(+)}(x)$, while the spontaneous breakdown of the $\mathcal{PT}$ symmetry of $V^{(-)}(x)$ implies the manifest breakdown of the $\mathcal{PT}$ symmetry of $V^{(+)}(x)$ [1]. The factorization energy ε was found to be real in the former case, and imaginary in the latter one. The examples analyzed to date, however, were restricted to some well-known exactly solvable potentials, which might not reveal some aspects of general situation. In order to gain a deeper insight, we separated the superpotential functions into real(R)/imaginary(I) and even(e)/odd(o) components

$$W(x) = W_{\mathrm{Re}}(x) + W_{\mathrm{Ro}}(x) + \mathrm{i}\, W_{\mathrm{Ie}}(x) + \mathrm{i}\, W_{\mathrm{Io}}(x) \qquad (2)$$

and implemented the condition for $\mathcal{PT}$ symmetry of $V^{(-)}(x)$ [2]. This resulted in an inhomogeneous system of linear first-order differential equations for $W_{\mathrm{Re}}(x)$ and $W_{\mathrm{Io}}(x)$:

$$W'_{\mathrm{Re}} - 2W_{\mathrm{Ro}}W_{\mathrm{Re}} + 2W_{\mathrm{Ie}}W_{\mathrm{Io}} = 0$$

$$W'_{\mathrm{Io}} - 2W_{\mathrm{Ie}}W_{\mathrm{Re}} - 2W_{\mathrm{Ro}}W_{\mathrm{Io}} = \mathrm{Im}(\varepsilon) \,, \qquad (3)$$

which has two specific properties: *i)* the inhomogeneity is represented by a constant, $\mathrm{Im}(\varepsilon)$; *ii)* the coefficients in the two equations are the same: $W_{\mathrm{Ro}}(x)$ and $W_{\mathrm{Ie}}(x)$.

Once $W_{\mathrm{Ro}}(x)$ and $W_{\mathrm{Ie}}(x)$ is selected, the solution of this system can be given in a straightforward way. It is also clear that in the presence of a real factorization energy the inhomogeneous system reduces to an homogeneous one. In [2] the inhomogeneous system was solved, while in [3] the general solutions were given with illsutrative examples for unbroken and spontaneously broken $\mathcal{PT}$ symmetry. It was found that in general the SUSY partner potential $V^{(+)}(x)$ can be $\mathcal{PT}$-symmetric only for the trivial solution $W_{\mathrm{Re}}(x) = W_{\mathrm{Io}}(x) = 0$.

[1] G. Lévai, M. Znojil, J. Phys. A **35** (2002) 8793.

[2] G. Lévai, J. Phys. A **37** (2004) 10179.

[3] G. Lévai, Czech. J. Phys. **54** (2004) 1121.

1.2 Scintillation detectors as self organized critical systems?

G. Kalinka, Z. Elekes, Zs. Fülöp, T. Motobayashi[a)], A. Saito[b)], Y. Yanagisawa[a)]

Recently we have constructed a 312 element scintillation detector (SD) system for nuclear physics experiments [1]. Both manufacture and the quality test were carried out under well controlled conditions. One of the main issues during manufacture was the uniformity of performance of the elements. Performance is determined by the signal amplitude delivered (a product of light creation, collection and detection) and the resolution (dispersion of amplitude). It is the mean and the standard deviation of these two parameters, which can be used to characterize the quality of the detector system [2]. More careful analysis of the amplitude and resolution data, taken with 5.5 MeV α particles, in addition, reveals fundamental features of scintillation detectors. Those, familiar with electrical noises, easily recognize from the time order series of data (Fig.a,b) the presence of $1/f^{\alpha}$, or flicker noise. This can be confirmed by Fourier analysis, which provides the spectral density distribution of the fluctuations, resulting in α=1.85±0.05 for amplitude and resolution alike (Fig.c). For resolution, however, at higher frequencies there is a transition to white noise.

It is well known that $1/f^{\alpha}$ noise has been observed in several systems having temporal, spatial or spatiotemporal degrees of freedom. Earlier examples are electric current in conductors, rotation of Earth, flow of rivers, heartbeat, stock exchange price indices, etc., recent ones are DNA sequence, human cognition, prime numbers, dynamic images, etc., and now scintillation detectors.

Despite extensive research, no universal theory for this ubiquitous phenomenon yet exists. One successful explanation, self organized criticality (SOC) [4], seems, however to fit to our case. Systems, with SOC are characterised by strong interdependence between their constituents. This dynamics results in collective behavior which cannot be understood by studying individual constituents in isolation. They exhibit, as a characteristic fingerprint, flicker noise, which is in fact not noise but reflects the intrinsic dynamics.

Light transport in SDs is, to large extent, a random and complicated process [5,6]. SDs can be considered as being composed of large number of interacting optical units of wavelength size. Changing the optical properties (reflection, transmission, absorption, polarisation, etc.) of one such unit brings about definitive, but hardly predictable change in the overall performance. Although, for the time being, strict theoretical or further convincing experimental arguments are still lacking, intuition tends to accept analogy with SOC systems.

a) RIKEN, Wako, Saitama, Japan

b) Rikkyo University, Tokyo, Japan

[1] Z. Elekes *et al.*, Nucl. Phys. A719 (2003) 316C

[2] G. Kalinka, ATOMKI Ann. Rep. 2003 (2004) 71

[3] P. Bak *et al.*, Phys. Rev. A38 (1988) 364

[4] E. Breitenberger, Prog. Nucl. Phys. 4 (1955) 56

[5] S.V. Naydenov, J. Appl. Spectr. 69 (2002) 535

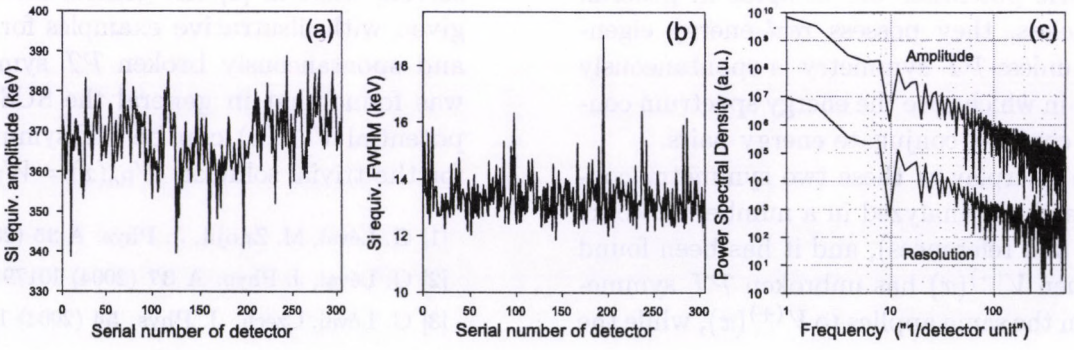

2.1 Internal pairs observed in a forbidden $0^- \rightarrow 0^+$ transition: a sign for a neutral boson?

A. Krasznahorkay, F.W.N. de Boer[a], J. Gulyás, Z. Gácsi, T.J. Ketel[a], M. Csatlós, L. Csige, M. Hunyadi, J. van Klinken[b], A. Krasznahorkay Jr, A. Vitéz

Although various experimental studies have provided constraints on the existence of elusive light neutral gauge bosons, with the revival of MeV-scale physics, a supersymmetric U-boson with lifetime of order 10^{-15} s is still a feasible candidate [1,2].

In order to search for the existence of such a ($J^\pi = 0^-$) boson a $0^- \rightarrow 0^+$ transition was chosen. Such transitions are strictly forbidden for emitting γ-rays or for emitting electron-positron pairs via the conventional Internal Pair Creation (IPC), but an emission of a light neutral particle which in turn decays into an e^+e^- pair is still a possible form of the deexcitation, which can be detected.

The 10.95 MeV 0^- state in ^{16}O was populated by the ^{14}N(^{3}He,p) reaction at E(^{3}He) = 2.4 MeV, and we measured coincidences with the low energy proton group populating the 0^- state. For high statistics measurements of the e^+ - e^- pairs, five ΔE - E detector telescopes from the IKF spectrometer [3] with large solid angles were used. The telescope detectors were placed outside of a thin wall vacuum chamber made of carbon fiber. The γ-rays were also measured in coincidence with the protons with a highly efficient clover type Ge detector.

Fig. 1. shows a γ-ray and an $e^+ + e^-$ sum spectrum measured in coincidence with the protons populating the 10.95 MeV 0^- state. As it should be, the γ-ray spectrum at the top does not show a peak at 10.96 MeV and is in fact nearly background-free above 10 MeV. It offers the best desirable conditions to search for the M0 transition in a simultaneously observed pair spectrum. Indeed we did observe for the first time this $0^- \rightarrow 0^+$ transition in ^{16}O by observing e^+e^- pairs. The energy sum of the pairs corresponds to the energy of the transition (10.95 MeV) and the observed branching ratio, $B = (20 \pm 5) \times 10^{-5}$, agrees with the expected axion branching ratio.

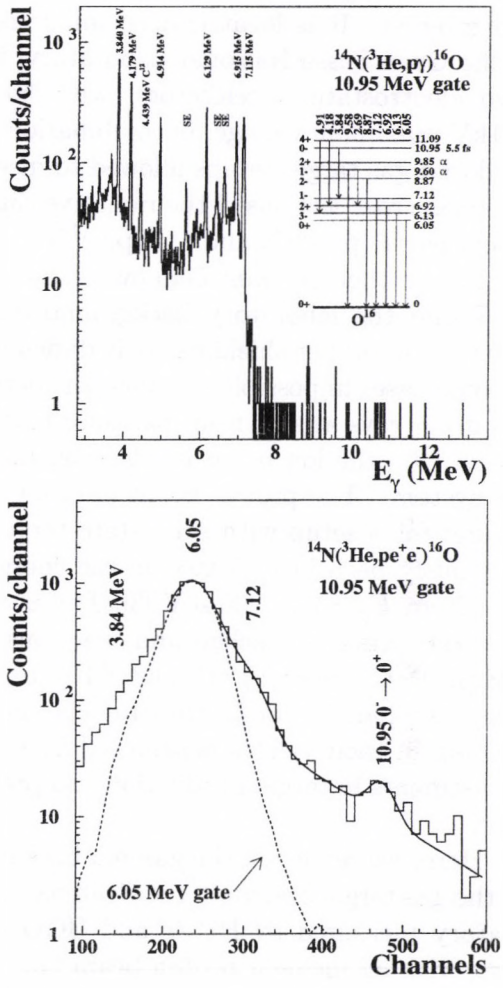

Figure 1. γ-ray and internal pair creation spectra obtained from the ^{14}N(^{3}He,p)^{16}O reaction. See text for the details.

a) NIKHEEF, Amsterdam, The Netherlands.

b) KVI, Groningen, The Netherlands.

[1] P. Fayet, Nucl. Phys. **B187** (1981) 187.

[2] C. Boehm, et al., Phys. Rev. Lett. **92** (2004) 101301.

[3] K.E. Stiebing et al., J. Phys. G: Nucl. Part. Phys. **30**, 165 (2004).

2.2 Background studies at the LUNA underground accelerator facility

Zs. Fülöp, Gy. Gyürky, E. Somorjai for the LUNA Collaboration

The LUNA (Laboratory Underground for Nuclear Astrophysics) facility has been designed to study nuclear reactions of astrophysical interest. It is located deep underground in the Gran Sasso National Laboratory, Italy. Two electrostatic accelerators, with 50 and 400 kV maximum voltage, in combination with solid and gas target setups allowed to measure the total cross sections of the radiative capture reactions ^{2}H(p,γ)^{3}He and ^{14}N(p,γ)^{15}O within or close to their relevant Gamow peaks [1,2].

While the laboratory background can be reduced by proper shielding, it is difficult and in some cases impossible to shield the detector against γ rays arising from parasitic reactions induced by the ion beam incident on the target system. The proton beam induced background for a setup with solid state target has previously been investigated in the energy region from $E_{\rm p} = 140$ - 400 keV [3]. It was found that the principal background reactions were ^{11}B(p,γ)^{12}C, ^{18}O(p,γ)^{19}F, and ^{19}F(p,$\alpha\gamma$)^{16}O. They originated from the target itself, and a reduction in their yield was achieved by making adjustments in target production and preparation.

Here, we report on the gamma background at the gas target system in the Gran Sasso Laboratory measured by HPGe and BGO detectors, with an incident proton beam [4].

A spectrum obtained with the HPGe detector at $E_{\rm p} = 200$ keV proton energy and with 1 mbar of nitrogen gas is shown at the top of Fig. 1. In the spectrum, the most important background lines as well as the lines from the ^{14}N(p,γ)^{15}O reaction are identified.

At the bottom of Fig. 1, two spectra obtained with the BGO detector at $E_{\rm p} = 200$ keV are shown: one denoted as 'nitrogen' with 1 mbar nitrogen as target gas, the other denoted as 'helium' with 1 mbar helium as target gas. It is clear that high resolution germanium detector is needed in order to identify the background visible in the spectra taken with the BGO detector.

The localisation of the background sources has been done using the Doppler shift of the γ lines. For a given transition and beam energy, the sign and magnitude of the shift depend only on the angle of emission θ, as measured from the beam direction. This allowed to localize in several cases the source of the γ rays.

In conclusion, the intensities and the sources of the beam induced background lines have been determined at the gas target system of LUNA. These results help to design further underground experiments and reach even lower background at LUNA.

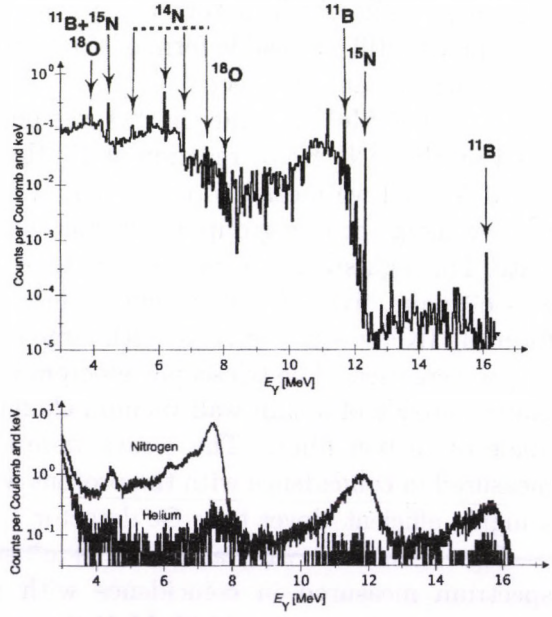

Figure 1. Spectra for $E_{\rm p} = 200$ keV with 1 mbar gas in the target. – Top panel: Germanium detector, nitrogen gas. – Bottom panel: BGO detector, one run with nitrogen gas and one run with helium gas.

[1] C. Casella, LUNA Collaboration, Nucl. Phys. A706 (2002) 203.

[2] A. Formicola, LUNA Collaboration, Phys. Lett. B591, (2004) 61.

[3] F. Strieder, LUNA Collaboration, Nucl. Phys. A718 (2003) 135c.

[4] D. Bemmerer, LUNA Collaboration, Eur. Phys. J. A in press.

2.3 Temperature dependence of electron screening in the d(d,p)t reaction

Zs. Fülöp, Gy. Gyürky, E. Somorjai for the LUNA Collaboration

We continued our systematic study on the anomalous enhancement of electron screening potential (U_e) for the d(d,p)t reaction in deuterated metals. The electron screening in d(d,p)t was studied previously for deuterated metals, insulators, and semiconductors [1]. As compared to measurements performed with a gaseous D_2 target ($U_e = 25\,eV$), a large screening was observed in the metals (of order $U_e = 300\,eV$), while a small (gaseous) screening was found for the insulators and semiconductors. An exception was found for the metals of groups 3 and 4 of the periodic table and the lanthanides, which showed a small screening; this is related to their high hydrogen solubility, of the order of one, that gives the deuterated targets of these metals the properties of insulators. Since the hydrogen solubility in metals decreases with increasing temperature, at higher temperatures the solubility of the metals of groups 3 and 4 and the lanthanides may be low enough that large U_e values can be observed. We report on studies aiming at the determination of the $U_e(T)$ dependence at the 100 kV accelerator of the Dynamitron-Tandem-Laboratorium at the Ruhr University Bochum, Germany [2].

All metals of groups 3 and 4 and the lanthanides have been studied at T = 200°C. The beam current on target was kept below 2μA leading to a negligible influence on the target temperature. As an example, the astrophysical S(E) factor obtained at T = 200°C for Hf is compared in Fig. 1 with that obtained at T = 20°C: at T = 200°C the solubility is reduced to a few percent and a large screening became observable. In fact, all metals exhibited a large reduction in solubility and thus showed a large screening, as expected.

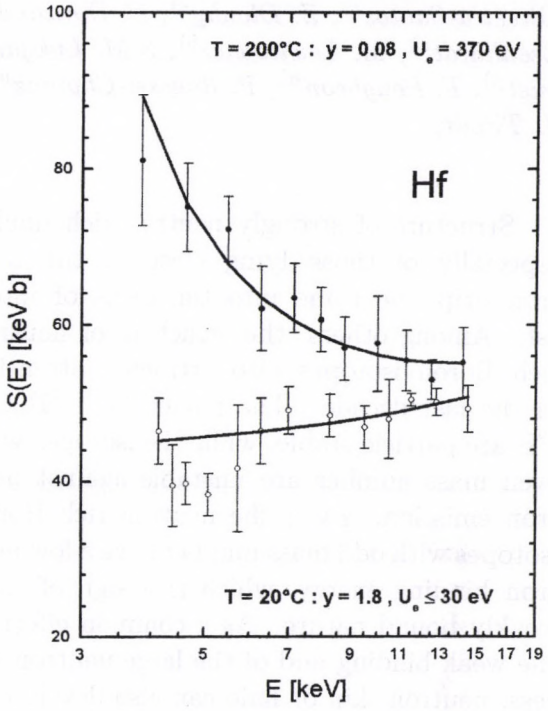

Figure 1. S(E) factor of d(d,p)t for Hf at T = 200°C and T = 20°C, with the deduced solubilities y. The curve for T = 20°C represents well the bare S(E) factor, while the curve for T = 200°C includes the electron screening with the U_e value given.

As a consistency test we also studied the insulator C at T = 200°C: the solubility decreased from 0.35 (T = 20°C) to 0.15, but no enhanced screening was observed, as expected for an insulator. Finally, we measured the screening for the metals Co and Pt as a function of sample temperature between T = 20°C and 340°C. The astrophysical S(E) factor obtained shows a decrease of the screening, with increasing temperature. The data represent the first observation of a temperature dependence of a nuclear cross section [3].

[1] F. Raiola et al, Phys. Lett B547 (2002) 193.

[2] F. Raiola et al, Eur. Phys. J. A19 (2004) 283.

[3] F. Raiola et al, Phys. Lett B, submitted

2.4 First observation of bound excited states in the A/Z=3 nucleus ^{15}B

Zs. Dombrádi, D. Sohler, F. Azaiez[a], M. Belleguic[a], M.J. Lopez-Jimenez[b], M.G. Saint-Laurent[b], O. Sorlin[a], N.L. Achouri[c], J.C. Angelique[c], C. Borcea[d], C. Bourgeois[a], J.M. Daugas[b], F. De Oliveira-Santos[b], Z. Dlouhy[e], C. Donzaud[a], J. Duprat[a], S. Grevy[c], D. Guillemaud-Mueller[a], S. Leenhardt[a], M. Lewitowicz[b], S.M. Lukyanov[f], W. Mittig[b], Yu.-E. Penionzhkevich[f], M.G. Porquet[g], F. Pougheon[a], P. Roussel-Chomaz[b], H. Savajols[b], Y. Sobolev[f], C. Stodel[b], M. Stanoiu[a,b], J. Timár,

Structure of strongly neutron rich nuclei, especially of those lying close to the neutron drip line came into the focus of interest. Among others, the structure of neutron rich Boron isotopes also attracted attention in the last decade. The nuclei ^{15}B, ^{17}B and ^{19}B are particle stable, while the isotopes with even mass number are unstable against neutron emission. Even the neutron rich Boron isotopes with odd mass number have a low neutron binding energy, which is a sign of their weakly bound nature. As a common effect of the weak binding and of the large neutron excess, neutron skin or halo can also develop already in the isotope ^{15}B with $A/Z = 3$.

Structure of the nucleus ^{15}B has been investigated by in-beam γ-spectroscopic study of the ^{9}Be + ^{36}S fragmentation reaction at GANIL, France. The emerging fragments were identified by use of a standard ΔE-time-of-flight technique with help of the SPEG spectrograph. γ-ray energies, intensities and $\gamma\gamma$ coincidences have been measured in coincidence with the projectile like fragments by 74 BaF_2 detectors of the Chateau de crystal. On the basis of the γ-spectroscopic information the level scheme presented in Figure 1 was constructed.

The level scheme is shown together with the results of different model calculations. The common in predictions of these models is that all of them suggest a ground state band with the spin sequence $3/2^-$, $5/2^-$ and $7/2^-$, as well as a $1/2^-$ state, which involves a proton single particle excitation. The shell model calculations (SM) predict similar moments of inertia, strongly different from that of the antisymmetrized molecular dynamics calculations (AMD).

The experimentally observed states can be assigned to the members of the rotational band on the basis of their decay properties. The experimental results confirm the predictions of the shell model.

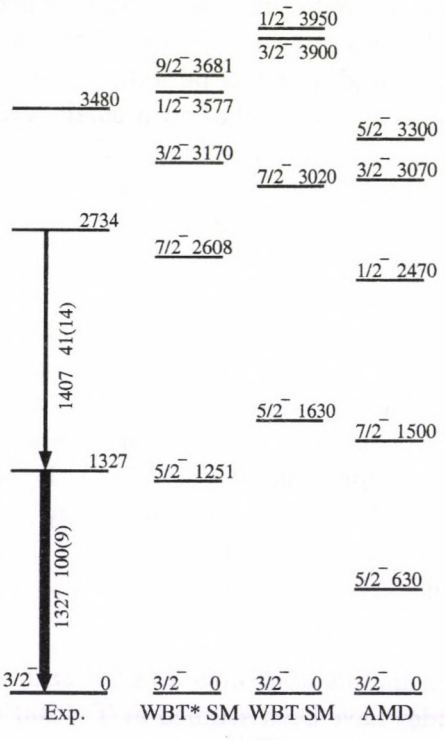

Figure 1. The level scheme of ^{15}B with the results of the shell and AMD model calculations. The unbound state at 3480 keV is taken from Ref. 1.

a) IPN, IN2P3-CNRS, Orsay, France

b) GANIL, Caen, France

c) Lab. de Phys. Corpusculaire, Caen, France

d) IFIN-HH, Bucarest, Romania

e) Nucl. Phys. Inst., Rez, Czech Republic

f) FLNR, JINR, Dubna, Russia

g) CSNSM, IN2P3-CNRS, Orsay, France

[1] R. Kalpakchieva et al, Eur. Phys. J. A 7(2000)451.

2.5 Low-lying bound excited states of ^{17}C and ^{19}C

Z. Elekes, Zs. Dombrádi, R. Kanungo[a], H. Baba[b], Zs. Fülöp, J. Gibelin[c], Á. Horváth[d], E. Ideguchi[e], Y. Ichikawa[e], N. Iwasa[f], H. Iwasaki[e], S. Kanno[b], S. Kawai[b], Y. Kondo[g], T. Motobayashi[a], M. Notani[e], T. Ohnishi[e], A. Ozawa[h], H. Sakurai[e], S. Shimoura[e], E. Takeshita[b], S. Takeuchi[a], I. Tanihata[i], Y. Togano[b], C. Wu[a], Y. Yamaguchi[b], Y. Yanagisawa[a], A. Yoshida[a], K. Yoshida[a]

Theoretical calculations predict two low-lying excited states of both ^{17}C and ^{19}C, but only one excited state has been found in ^{17}C. Recently, indications of two γ transitions of ^{17}C have been reported, suggesting that both predicted excited states are bound in ^{17}C. In addition, a γ peak in ^{19}C was also observed.

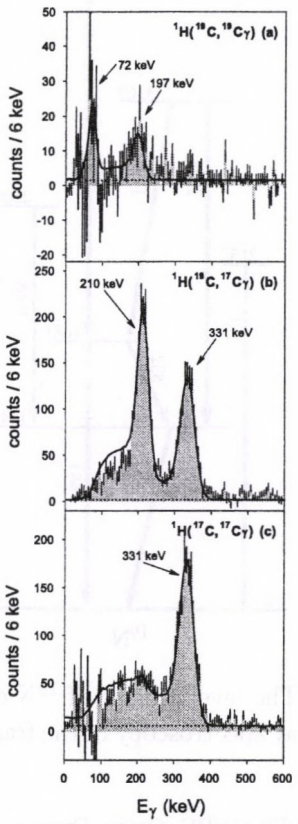

Figure 1. Doppler-corrected spectra of γ rays emerging from ^{1}H(^{19}C,^{19}C) (a), ^{1}H(^{19}F,^{17}C) (b) and ^{1}H(^{17}C,^{17}C) (c) reactions.

To obtain more information on the excited states in neutron rich odd carbon nuclei we have studied them by the (p,p'γ) process in inverse kinematics. The experiment was carried out at the RIKEN radioactive isotope separator RIPS. A ^{22}Ne primary beam of 100 pnA intensity and 110 A·MeV energy hits a ^{9}Be production target of 0.8 cm thickness. For optimizing the ^{19}C beam, the secondary cocktail beam included 20% ^{19}C and 25% ^{17}B. By tuning the ^{17}C beam, practically 100% purity could be achieved. On an event-by-event basis, the identification of the incoming beam was performed by energy-loss, time-of-flight (TOF) and magnetic rigidity ($B\rho$) measurements. The secondary beam bombarded a liquid hydrogen target of 3 cm diameter. A NaI(Tl) array surrounded the liquid hydrogen target to detect de-excited γ rays. A silicon telescope with layers of 0.5, 2 and 2 mm thicknesses was inserted in air atmosphere to identify scattered particles. To produce γ ray spectra, one fold events in the NaI(Tl) setup were selected (Fig. 1). In the (a) panel, two peaks are clearly visible at 72(4) and 197(6) keV which can be associated with the prompt decays of excited states of ^{19}C. Fig. 1 (b) shows two distinct peaks at 210(4) and 331(6) keV confirming two low-lying excited states of ^{17}C. In the (c) panel of the ^{1}H(^{17}C,^{17}C) reaction, the higher energy peak is clearly visible, while the 210 keV peak is very faint, if it exists at all, and is situated on the Compton background of the 331 keV peak. The counting statistics in Fig. 1 (b) allowed us to perform a γ-γ coincidence analysis, which showed that the two observed transitions of ^{17}C are not in coincidence. The analyses of the spectra and the cross sections are now in progress.

a) RIKEN
b) Rikkyo University
c) Institut de Physique Nucléaire
d) Eötvös Lóránd University
e) University of Tokyo
f) Tohoku University
g) Tokyo Institute of Technology
h) University of Tsukuba
i) Argonne National Laboratory

2.6 In beam γ-ray spectroscopy of the neutron rich isotope ^{19}N

Zs. Dombrádi, D. Sohler, F. Azaiez[a)], M. Belleguic[a)], M.J. Lopez-Jimenez[b)], M.G. Saint-Laurent[b)], O. Sorlin[a)], N.L. Achouri[c)], J.C. Angelique[c)], C. Borcea[d)], C. Bourgeois[a)], J.M. Daugas[b)], F. De Oliveira-Santos[b)], Z. Dlouhy[e)], C. Donzaud[a)], J. Duprat[a)], S. Grevy[c)], D. Guillemaud-Mueller[a)], S. Leenhardt[a)], M. Lewitowicz[b)], S.M. Lukyanov[f)], W. Mittig[b)], Yu.-E. Penionzhkevich[f)], M.G. Porquet[g)], F. Pougheon[a)], P. Roussel-Chomaz[b)], H. Savajols[b)], Y. Sobolev[f)], C. Stodel[b)], M. Stanoiu[a,b)], J. Timár,

Structure of nuclei close shell closures can give information on the nature of the shell model effective interaction. Recently, it has been observed that the USD interaction [1] working well in the *sd* shell does not describe the binding energy of the heavy carbon isotopes [2]. It has also been observed that the magnetic moment of heavy istopes cannot be desribed by use of the shell model with the USD interaction, only if the neutron binding energy is decreased by about 20% [3]. Study of the structure of nitroge isotopes lying to the single closed shell oxygen nuclei may reveal information on wether the enrgy structure of shell model nuclei is perurbed relative to the USD prediction. In a recent study we have shown that the experimental level energies are in a nice agreement with the USD prediction up to the heaviest bound oxygen isotope ^{24}O.

Structure of the nucleus ^{19}N has been investigated by in-beam γ-spectroscopic study of the ^{9}Be + ^{36}S fragmentation reaction at GANIL, France. The emerging fragments were identified by use of a standard ΔE-time-of-flight technique with help of the SPEG spectrograph. γ-ray energies, intensities and $\gamma\gamma$ coincidences have been measured in coincidence with the projectile like fragments by 74 BaF_2 detectors of the Chateau de crystal and four hyperpure Ge detectors. On the basis of the γ-spectroscopic information the level scheme presented in Figure 1 was constructed. The level scheme is very similar to that of the ^{17}N isotope in the sense that we have the band like structure shown in the middle together with proton cross shell excitations decaying to the ground and first excited states.

Comparing the experimental energies observed to those calculated by use of the shell model with USD interaction, it was observed, that the band structure is more compressed than calculated. A 25% compression of the calculated band corrects for the deviations. This defect of the USD interaction is in agreement with the previous observation.

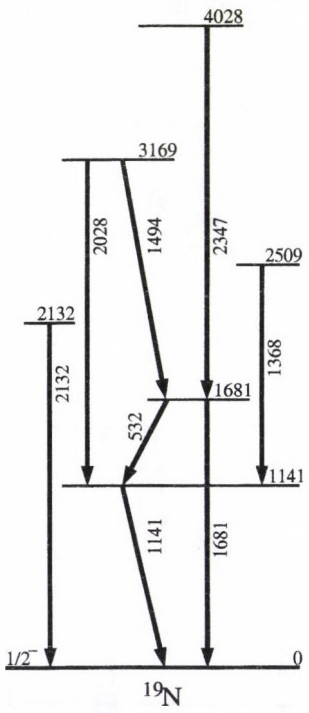

Figure 1. The level scheme of ^{19}N obtained from in beam γ-ray spectroscopy of the fragmentation of a ^{36}S beam.

a) IPN, IN2P3-CNRS, Orsay, France
b) GANIL, Caen, France
c) Lab. de Phys. Corpusculaire, Caen, France
d) IFIN-HH, Bucarest, Romania
e) Nucl. Phys. Inst., Rez, Czech Republic
f) FLNR, JINR, Dubna, Russia
g) CSNSM, IN2P3-CNRS, Orsay, France

[1] E. K. Warburton and B. A. Brown, Phys. Rev. C 46, 923 (1992).
[2] D. Bazin et al., Phys. Rev. Lett. 74, 3569 (1995).
[3] H. Ueno et al., Phys. Rev. C 53, 2142 (1996).
[4] M. Stanoiu et al., Phys. Rev. C 69, 034312 (2004).

2.7 Core excited states in neutron rich nuclei ^{23,25}F

Zs. Dombrádi, D. Sohler, B.A. Brown[a], F. Azaiez[b], M. Belleguic[b], M.J. Lopez-Jimenez[c], M.G. Saint-Laurent[c], O. Sorlin[b], N.L. Achouri[d], J.C. Angelique[d], C. Borcea[e], C. Bourgeois[b], J.M. Daugas[c], F. De Oliveira-Santos[c], Z. Dlouhy[f], C. Donzaud[b], J. Duprat[b], S. Grevy[d], D. Guillemaud-Mueller[b], S. Leenhardt[b], M. Lewitowicz[c], S.M. Lukyanov[g], W. Mittig[c], Yu.-E. Penionzhkevich[g], M.G. Porquet[h], F. Pougheon[b], P. Roussel-Chomaz[c], H. Savajols[c], Y. Sobolev[g], C. Stodel[c], M. Stanoiu[b,c], J. Timár,

Since the discovery of erosion of shell closures at extreme proton to neutron ratios, a renewed interest has been shown in searching for emerging new magic numbers and disappearance of old ones in different regions of the nuclide chart. Recently signs of a subshell closure at N=16 have been observed in Oxygen isotopes by analyzing mass and total reaction cross section data. Recent γ-spectroscopic results on ^{22}O show a high $E_{2_1^+}$ energy and a low B(E2;$2_1^+ \rightarrow 0_1^+$) transition probability indicating a subshell closure also at N=14. The situation is similar to the Z=14,16 case of ^{34}Si and ^{36}S at N=20. In spite of having a strongly bound ground state in ^{24}O its first excited state is unbound. On the other hand, excited states in ^{25}F arising from the coupling of the $d_{5/2}$ proton to the 2_1^+ state of ^{24}O are expected to be bound. Thus, from shell model analyzis of the energies of core excited states in ^{25}F conclusion can be drawn on the size of the N=16 subshell gap.

To get information on the structure of the neutron rich ^{23,25}F their excited states were populated via the fragmentation of a ^{36}S beam at GANIL, France. The emerging fragments were detected by the SPEG spectrometer. Ionization and drift chambers, as well as a plastic scintillator were placed at its focal plane providing information on the energy loss, total energy, and time-of-flight of the fragments for their identification. Nuclei produced in the reaction were created in excited states which deexcited by emission of γ rays in flight. These γ rays were observed by 74 BaF_2 and 4 hyper pure Ge detectors surrounding the Be target. Using the energies, intensities and coincidence relations of the γ transitions level schemes of ^{23,25}F could be constructed for the first time.

The experimental energies obtained for ^{25}F are compared with the results of large-scale shell-model calculations in Figure 1. It can be seen that several states between 3 and 4 MeV excitation energy can be assigned to the $\pi d_{5/2} \oplus 2^+$ configuration. They are well described by the shell model, giving credit also to its prediction on the energy of the 2_1^+ state in ^{24}O, which is expected to be at about 4.2 MeV.

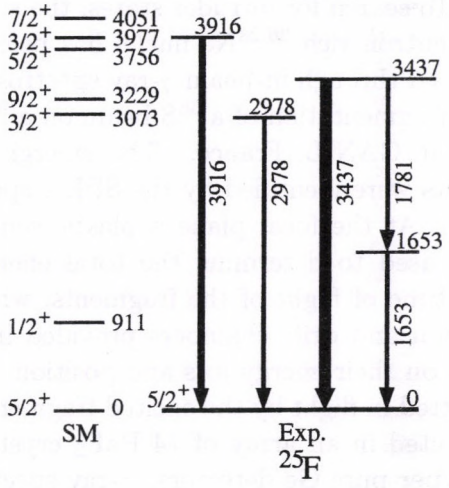

Figure 1. Proposed experimental level scheme of ^{25}F. The results of the large scale shell model calculations are included in the left part of the figure.

a) NSCL, MSU, East Lansing, USA

b) IPN, IN2P3-CNRS, Orsay, France

c) GANIL, Caen, France

d) Lab. de Phys. Corpusculaire, Caen, France

e) IFIN-HH, Bucarest, Romania

f) Nucl. Phys. Inst., Rez, Czech Republic

g) FLNR, JINR, Dubna, Russia

h) CSNSM, IN2P3-CNRS, Orsay, France

2.8 Neutron excitations across the N=20 shell gap in ^{26,28}Ne

Zs. Dombrádi, D. Sohler, T. Otsuka[a], F. Azaiez[b], M. Belleguic[b], M.J. Lopez-Jimenez[c], M.G. Saint-Laurent[c], O. Sorlin[b], N.L. Achouri[d], J.C. Angelique[d], C. Borcea[e], C. Bourgeois[b], J.M. Daugas[c], F. De Oliveira-Santos[c], Z. Dlouhy[f], C. Donzaud[b], J. Duprat[b], S. Grevy[d], D. Guillemaud-Mueller[b], S. Leenhardt[b], M. Lewitowicz[c], S.M. Lukyanov[g], W. Mittig[c], Y. Utsuno[h], Yu.-E. Penionzhkevich[g], M.G. Porquet[i], F. Pougheon[b], P. Roussel-Chomaz[c], H. Savajols[c], Y. Sobolev[g], C. Stodel[c], M. Stanoiu[b,c], J. Timár,

A sudden lowering of the energy of the intruder states based on neutron cross shell excitations is expected to play a crucial role in fading out of the N=20 shell effects around ^{32}Mg. Ground states of the nuclei in this region are expected to arise from an intruder neutron configuration resulting in formation of an island of inversion. Although, this expectation is quite old, no traces of shape coexistence have been found yet in any of the nuclei of the island of inversion nor in lighter nuclei around it.

To search for intruder states, the structure of neutron rich ^{26,28}Ne nuclei has been investigated through in-beam γ-ray spectroscopy of the fragmentation of a ^{36}S beam on a ^{9}Be target at GANIL, France. The emerging fragments were identified by the SPEG spectrometer. At the focal plane a plastic scintillator was used to determine the total energy and the time of flight of the fragments, while ionization and drift chambers provided information on their energy loss and position. γ rays, emitted in flight by the excited fragments were detected in an array of 74 BaF_2 crystals and 4 hyper pure Ge detectors. γ-ray spectrum of ^{28}Ne together with a normalized random background spectrum is shown in Figure 1.

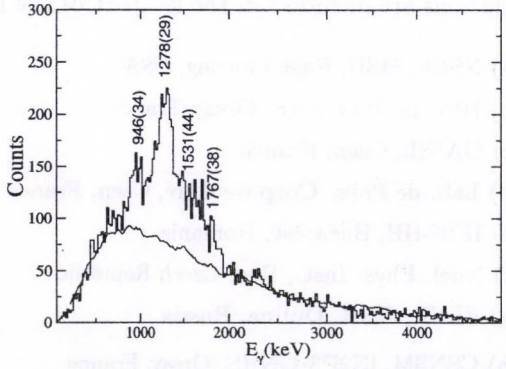

Figure 1. BaF_2 γ-ray spectrum of ^{28}Ne together with a normalized random background spectrum.

The high efficiency of the BaF_2 array made possible to observe $\gamma\gamma$-coincidences in coincidence with the emerging fragments. $\gamma\gamma$-coincidence spectra of ^{28}Ne gated by the 916 and 1767 keV γ-rays are presented in Figure 2. Using this information in construction of the level schemes 3-3 new states could be established both in ^{26}Ne and ^{28}Ne. According to shell-model calculations, in ^{28}Ne the 2183 keV state connected by the 916 keV transition to the 2_1^+ state at 1281 keV is the intruder 0_2^+ state providing the first candidate for cross shell excited states at the border of the island of inversion.

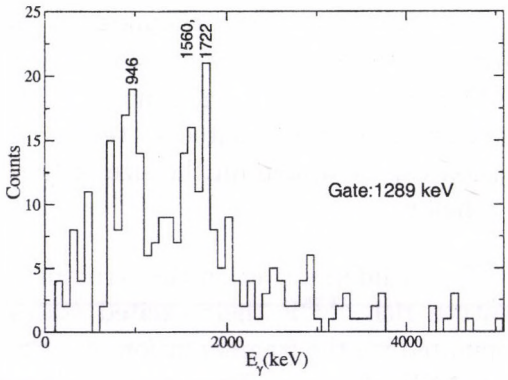

Figure 1. BaF_2 coincidence spectra of ^{28}Ne gated by the 916 and 1767 keV γ-rays.

a) Univ. of Tokyo, Hongo, Tokyo, Japan
b) IPN, IN2P3-CNRS, Orsay, France
c) GANIL, Caen, France
d) Lab. de Phys. Corpusculaire, Caen, France
e) IFIN-HH, Bucarest, Romania
f) Nucl. Phys. Inst., Rez, Czech Republic
g) FLNR, JINR, Dubna, Russia
h) JAERI, Tokai, Japan
i) CSNSM, IN2P3-CNRS, Orsay, France

2.9 Structure of the neutron-rich ^{37}P and ^{39}P nuclei

Zs. Dombrádi, O. Sorlin[a], D. Sohler, F. Azaiez[a], J. Timár, Yu.-E. Penionzhkevich[b], F. Amorini[a], D. Baiborodin[b], A. Bauchet[c], F. Becker[d], M. Belleguic[a], C. Borcea[e], C. Bourgeois[a], Z. Dlouhy[g], C. Donzaud[a], J. Duprat[a], D. Guillemaud-Mueller[a], F. Ibrahim[a], M.J. Lopez[f], R. Lucas[h], S.M. Lukyanov[b], V. Maslov[b], J. Mrazek[g], C. Moore[i], L. Petizon[a], M.G. Saint-Laurent[f], F. Sarazin[c], J.A. Scarpaci[a], M. Stanoiu[f], G. Sletten[j], C. Stodel[a], M. Taylor[i], C. Theisen[d], G. Voltolini[f],

In the last few years, large efforts were devoted to the study of the evolution of the N=28 shell gap between the neutron $f_{7/2}$ and $p_{3/2}$ orbitals, as the neutron to proton ratio is increased. Development of collectivity around N=28 has already been emphasized by several authors. Increase of the collectivity could partially be traced back to a gradual decrease of the proton single particle energy difference $\pi s_{1/2}$–$\pi d_{3/2}$ from N=20 to N=28. Study of the neutron-rich odd Phosphorus isotopes ^{37,39}P$_{22,24}$ was aimed at clarifying to what extent and how this effect takes place in the Z=15 isotope chain.

Structure of the ^{37,39}P nuclei was investigated by in-beam γ-ray spectroscopy using the fragmentation of a ^{48}Ca beam. The SPEG spectrometer was used to identify the emerging fragments detected at the focal plane. The thin Be target was surrounded by an array of 74 BaF_2 and 3 segmented Ge clover detectors to measure the energies, intensities and anisotropy, as well as the coincidence relationships of the γ-rays emitted in flight by the excited fragments. Based on the information obtained level schemes with spin assignments were proposed for the studied nuclei. In the γ-ray spectra of ^{37}P only one γ-line was present at 868 keV indicating the existence of a level at this energy connected directly to the ground state. In ^{39}P we found four γ-lines at 355, 619, 963 and 1201 keV. Placing them in the level scheme excited states were established at 355, 963 and tentatively at 2164 keV.

The experimental level schemes compared with the results of shell model calculations are presented in Figure 1. In both ^{37}P and ^{39}P calculations underestimate the energy of the excited states by 300 to 400 keV. This discrepancy can be traced back to the $f_{7/2}^2$ matrix elements since the calculated 2_1^+ states in the N=22 isotones from $^{36}_{14}$Si to $^{38}_{16}$S exhibit too high energy as compared to experiment. One reason could be that the fp part of the effective interaction was adjusted from a ^{40}Ca core while the effective neutron-neutron interaction in our study is applied to an ^{28}O core. The results are published in Ref. [3].

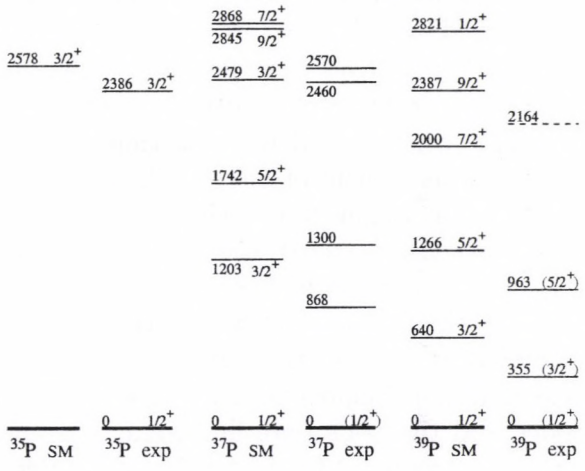

Figure 1. Comparison of the experimental (exp) and calculated level schemes (SM) for the P isotopes. The experimental data for ^{35}P are taken from Ref. 1 and for the states at 1300, 2460 and 2570 keV in ^{37}P from Ref. 2.

a) IPN, IN2P3-CNRS, Orsay, France
b) FLNR, JINR, Dubna, Russia
c) CSNSM, IN2P3-CNRS, Orsay, France
d) CEA-Saclay, Gif sur Yvette, France
e) IAP, Bucharest-Magurele, Romania
f) GANIL, Caen, France
g) NPI, Rez, Czech Republic
h) IPN, Lyon, France
i) OLL, Univ. of Liverpool, Liverpool, UK
j) NBI, Copenhagen, Denmark

[1] J.P. Dufour et al., Z. Phys. A 324, 487 (1986).
[2] N.A. Orr, PhD Thesis, Austr. Nat. Univ., 1989.
[3] O. Sorlin et al., submitted to Eur. Phys. J. A.

2.10 High efficiency ionization chamber for fission experiments

L. Csige, M. Csatlós, J. Gulyás, Z. Gácsi, M. Hunyadi, A. Krasznahorkay

The width of fission fragment mass distribution indicates the number of different fragments which are produced during the fission process from a given excited state. Smaller width means more limited variety of fission fragments which can indicate clusterization effect in hyperdeformed states before fission and also means less amount of nuclear waste.

A new gridded ionization chamber was constructed at Atomki to examine the mass distribution of the fission fragments from neutron induced fission of some U and Th isotopes. The design is based on a twin ionization chamber developed by C. Budtz-Jorgensen et al.[1]. Our aim was to increase the efficiency of the measurements by applying multiple detector units.

This compound detector permits simultaneous measurement of the total kinetic energy and fission fragment emission angle with respect to the detector symmetry axis. The chamber consists of five twin parallel plate ionization chambers with Frisch grids. Assuming that at low counting rates only one target emits fission fragments in one event, the anodes and the grids were interconnected forming two groups (A1-G1, A2-G2). In order to identify which target emitted the fission fragments the signals from each cathodes are also processed.

The energy of the fission fragments is determined from the anode pulse heights, while the sum of the grid and anode signals is used to deduce the fragment emission angle θ with respect to the symmetry axis of the chamber:

$$Q_{sum} = -n_0 e[1 - (X/D)cos\theta]$$

The angle dependent energy losses in the target can be determined using this angular information.

In order to minimize the distance between the targets and the neutron source, smaller distance between the plates and a smaller diameter had to be chosen as in Ref.[1]. This arrangement required higher gas pressure, which is necessary to stop the fission fragments before reaching the electrodes. A gas mixture of 90% Ar + 10% CH_4 at 2 atm pressure was used. With a test measurement at this pressure using ^{252}Cf source the optimal cathode and anode voltages were found to be at 4 kV and 3 kV, respectively.

Five large area (12.6 cm^2) and thin (100 $\mu g/cm^2$) targets were placed into the center of each cathode plane of the chamber. Preliminary measurement with thorium targets was performed recently in Karlsruhe.

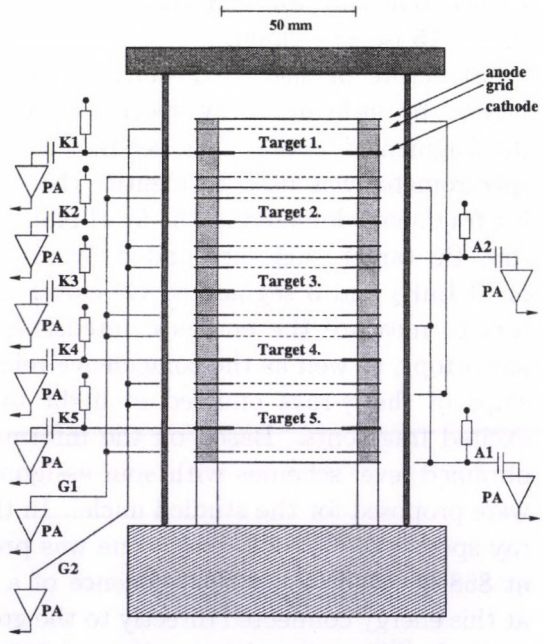

Figure 1. Schematic view of the chamber
PA: charge sensitive preamplifier

[1] C. Budtz-Jorgensen et al., Nucl. Inst. and Meth. in Phys. Res. **A258** (1987) 209-220

2.11 Influence of triaxiality on the signature inversion in odd-odd nuclei

R.R. Zheng[a)], S.Q. Zhu[a,b)], X.D. Luo[a)], J. Timár, A. Gizon[c)], J. Gizon[c)], D. Sohler, B.M. Nyakó, L. Zolnai, E.S. Paul[d)]

Signature inversion in the $A \approx 100$ region has been reported earlier only in the case of the odd-odd ^{98}Rh nucleus [1]. Our studies on the $^{100-103}$Rh isotopes and a close inspection of the known $\pi g_{9/2}\nu h_{11/2}$ bands of the Rh (Z=45) and Ag (Z=47) isotopes revealed that the signature splitting effects, earlier considered as quenchings of signature splitting, are not only quenchings but signature inversions. Indeed, the energetically favored signature at low spins in these $\pi g_{9/2}\nu h_{11/2}$ bands is the $\alpha = 1$ branch (odd spins) instead of the expected $\alpha = 0$ branch (even spins). The systematic occurrence of signature inversion in this mass region is discussed in Refs. [2,3] together with attempts to understand its behavior qualitatively.

Among many attempts for interpreting the mechanism of signature inversion in odd-odd nuclei, a model using an axially symmetric rotor plus two quasi-particles has already been successfully applied to describe the observed signature inversions in the $A \approx 80$ and $A \approx 160$ mass regions [4,5]. According to this model the signature inversion is caused by the competition between the Coriolis and the proton-neutron residual interactions in low K space. Such calculations have been also successfully applied to the $\pi g_{9/2}\nu h_{11/2}$ bands in the odd-odd ^{98}Rh and ^{102}Rh nuclei [6].

Recent observations of chiral band structures in the nearby Rh nuclei suggest a possibility of triaxiality in these nuclei, too. In the present work we examined the possible influence of triaxiality on the signature inversion using a triaxial rotor plus two-quasiparticle model and compared the results with the experimental data of ^{98}Rh and ^{102}Rh. The calculations provided a better agreement with the experiment than the axially symmetric calculations. Compared to the axially symmetric case, the triaxiality applied in the Hamiltonian enlarges the amplitudes of high-spin signature zigzags at small triaxial deformation and might push the signature inversion point to higher spin at large triaxial deformation. The results are published in Ref. [7].

a) Department of Physics, Shanghai Normal University, Shanghai 200234

b) Shanghai Commercial Polytechnic, Shanghai 201400

c) LPSC, IN2P3-CNRS/UJF, F-38026 Grenoble-Cedex, France

d) Oliver Lodge Laboratory, Department of Physics, University of Liverpool,Liverpool L69 7ZE, UK

[1] S. Chattopadhyay, et al., Phys. Rev. C57 (1998) R471.

[2] J. Timár, et al., Nucl. Phys. A696 (2001) 241.

[3] J. Timár, et al., Acta Physica Polonica B33 (2002) 493.

[4] R.R. Zheng, S.Q. Zhu, and Y.W. Pu, Phys. Rev. C56 (1997) 175.

[5] R.R. Zheng, S.Q. Zhu, N.P. Cheng, and J.Y. Wen, Phys. Rev. C64 (2001) 014313.

[6] R.R. Zheng, X.D. Luo, and S.Q. Zhu, Intern. J. of Modern Phys. Vol.12,No.1(2003)59.

[7] R. Zheng, et al., Chin. Phys. Lett. 21 (2004) 1475.

2.12 Study of low energy α-scattering on ^{89}Y

G.G. Kiss, Zs. Fülöp, Gy. Gyürky, Z. Máté, E. Somorjai, D. Galaviz[a)], A. Zilges[a)]

The heavy, proton-rich nuclei (p-nuclei) are produced by the so-called astrophysical p-process. This process involves γ-induced reactions on abundant, neutron-rich s-isotopes. In order to derive the abundance distribution of the proton-rich nuclei, it is necessary to know the reaction rates for the photon-induced reactions at the astrophysical energy of interest, in the Gamow-window. The (γ,α) and (γ,p) reaction rates can be obtained from the measured cross section of the inverse (α,γ)and (p,γ) reactions. Nevertheless, few of these reaction rates have been determined experimentally. Therefore the astrophysical calculations are based on the statistical model theory. Alpha-nucleus potentials are important ingredients for the calculation of (γ,α) photodisintegration rates. It has been shown that there are large uncertainties for the predictions of the (γ,α) reaction rates because of the limited knowledge of the α-nucleus potentials at the astrophysically relevant energies [1]. Systematic experimental study can help in understanding better the α-nucleus potential in mass region relevant to the p-process. The α-nucleus potential can be determined from elastic scattering experiments. Recently α-nucleus potentials of ^{144}Sm, ^{92}Mo, ^{112,114}Sn isotopes have been determined [2 – 4] at the ATOMKI.

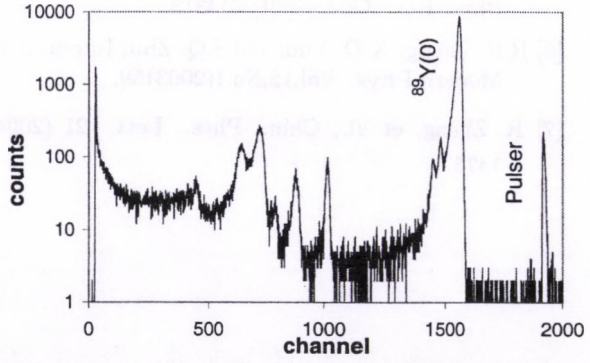

Figure 1. Typical spectra of ^{89}Y(α,α)^{89}Y at ϑ=30° at E_α=16.165MeV beam energy.

The present elastic scattering experiment aiming to determine the optical potential of the ^{89}Y neutron magic nucleus was performed at the Cyclotron Laboratory of ATOMKI [5]. The angular distributions were measured at laboratory energies of 16.165 and 19.519 MeV, slightly above the Coulomb barrier. The target was produced by evaporating metallic Y onto thin carbon foil, the target thickness was about 200 μg/cm^2. The target was placed in the center of a 78 cm scattering chamber, and spectra were taken at angles between 20° $\leq \vartheta_{LAB} \leq$ 170° in 1°-1.5° steps. Two monitor detectors were fixed at ±15° respect to the direction of the beam. The experimental data normalised to the Rutherford cross section is shown in Fig.2. Typical uncertainties remain below 3-4% for all measured data points. The final analysis and the determination of the optical potential is in progress.

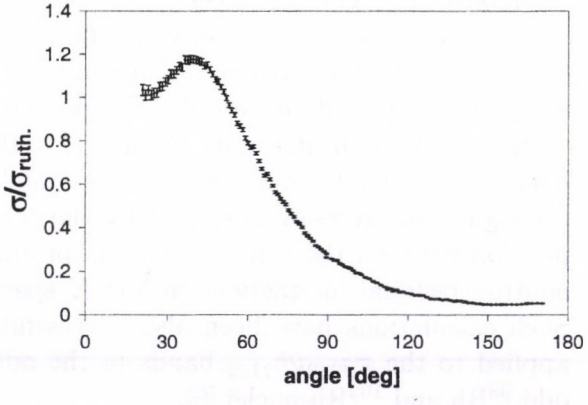

Figure 2. Elastic scattering cross section of ^{89}Y(α,α)^{89}Y at E_α=16.165MeV, normalised to Rutherford cross section.

a) Technische Univ. of Darmstadt, Inst. für Kernphysik, Darmstadt, Germany

[1] G.R. Satchler, Phys. Rep. 199 (1991)

[2] P. Mohr et al., Phys. Rev. C55 (1997).

[3] Zs. Fülöp et al., Phys. Rev. C64 (2001).

[4] D. Galaviz et al., Phys. Rev. C submitted.

[5] G.G. Kiss, Diploma thesis, Univ. of Debrecen, 2004.

2.13 Study of negative-parity high-spin bands in ^{102}Ru

D. Sohler, J. Timár, J. Molnár, A. Algora, Zs. Dombrádi, A. Krasznahorkay, L. Zolnai, G. Rainovski[a)1], *P. Joshi*[b)], *K. Starosta*[c,a)], *D.B. Fossan*[a)2], *R. Wadsworth*[b)], *P. Bednarczyk*[d)], *D. Curien*[e)], *G. Duchene*[e)], *A. Gizon*[f)], *J. Gizon*[f)], *D.G. Jenkins*[b)], *T. Koike*[g)], *E.S. Paul*[h)], *P.M. Raddon*[b)], *J.N. Scheurer*[i)], *A.J. Simons*[b)], *C. Vaman*[a)], *A.R. Wilkinson*[b)]

Several nuclear structure phenomena related to triaxiality have been pointed out in the region of transitional nuclei near A$\sim$100 below the tin isotope chain. The occurrence of signature inversion has been reported in $^{98,100-103}$Rh isotopes and recently, chiral twin bands have been found in ^{104,105,106}Rh nuclei. More recently, the rigid or γ-soft type of triaxiality in ^{102}Ru has been examined through an analysis of the excitation energies in the low-spin quasi-γ band. In the present work we report on extension of the band structure of ^{102}Ru.

High-spin states in the nucleus ^{102}Ru were investigated via the ^{96}Zr(^{13}C,α3n) reaction at beam energies of 51 and 58 MeV with the EUROBALL IV γ-ray spectrometer and the DIAMANT charged particle array. The already known negative parity bands (bands 2 and 3 in Fig. 1) were extended up to E_x $\sim$11 and $\sim$9 MeV with I^π=(23$^-$) and (20$^-$), respectively. In addition, two new negative-parity bands were observed shown as bands 4 and 5 in Fig. 1. The deduced high-spin structure has been compared with Woods-Saxon TRS calculations. On the basis of the comparison of measured and calculated Routhians, aligned angular momenta and M1/E2 branching ratios $\nu h_{11/2}(g_{7/2}, d_{5/2})$ configurations are suggested for all the negative-parity bands. The obtained results have been presented in Ref. [1].

a) Department of Physics and Astronomy, SUNY, Stony Brook, New York, 11794-3800, USA
b) Department of Physics, University of York, York, YO10 5DD, UK
c) NSCL, Cyclotron Laboratory, Michigan State University, East Lansing, MI 48824-1321, USA
d) GSI, Darmstadt, Germany
e) IReS, 23 rue du Loess, Strasbourg, 67037, France
f) LPSC, IN2P3-CNRS/UJF, F-38026 Grenoble-Cedex, France
g) Department of Physics, Tohoku University, Sendai, Japan
h) Oliver Lodge Laboratory, Department of Physics, University of Liverpool,Liverpool L69 7ZE, UK
i) Université Bordeaux 1, IN2P3- CENBG - Le Haut-Vigneau BP120 33175, Gradignan Cedex, France

[1] D. Sohler *et al.*, submitted to Phys. Rev. C.

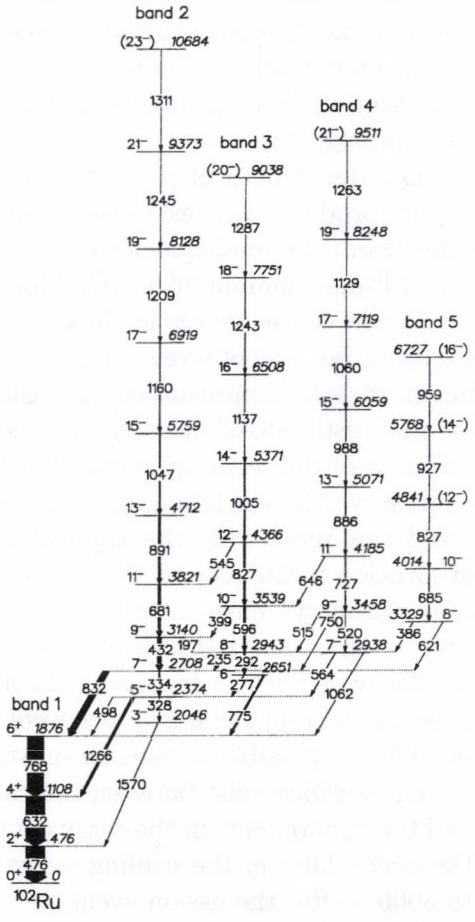

Figure 1. The partial level scheme of ^{102}Ru obtained in the present work.

[1] On leave of absent from Faculty of Physics, St. Kliment Ohridski University of Sofia, BG-1164 Sofia, Bulgaria
[2] Deceased

2.14 β-decay data for reactor heat calculations: measurement of the decay of ^{104,105}Tc isotopes using a total absorption spectrometer

A. Algora, J.L. Tain[a], B. Rubio[a], A.B. Perez[a], L. Caballero[a], J. Agramunt[a], E. Nácher[a], A. Krasznahorkay, M. Hunyadi, J. Gulyás, A. Vitéz, L. Batist[b], K. Burkard[c], W. Hüller[c], H. Penttilä[d], A. Nieminen[d], I. Moore[d], S. Rinta-Antila[d], P. Karvonen[d], A. Jokinen[d], A. Kankainen[d], T. Eronen[d], U. Hager[d], T. Sonoda[d], J. Äystö[d], J. Hakala[d], W. Gelletly[e], A. Garcia[f], I. Izosimov[g]

Safe operational procedures are a major pre-requisite of the design and development of nuclear power plants. The primary aim of this work was to study the decay characteristics of specific nuclei that are important contributors to the decay heat emitted by the reactor core immediately following shutdown.

Requirements for decay-heat calculations are: databases that contain all the necessary information (nuclide, lifetime, mean γ-, β-, and α- energy released in the decay, n-capture cross sections, etc...), and estimates of the uncertainties in these data.

The decay data of some of the important fission products are extremely complex and suffer from the inadequacies caused by the so called Pandemonium effect [1]. This effect has significant consequences in the decay-heat calculations because of levels missed in the experiment at high excitation energy; the result is an underestimate of the γ energy and an overestimate of the β energy released in the decay.

It is worth mentioning that the only way to avoid this problem is the application of total absorption techniques to β decay studies. For that reason we have installed a total absorption setup at the IGISOL facility to measure the decay of ^{104,105}Tc isotopes. The incomplete β decay data on these isotopes were identified in [2] as the possible source of a substantial discrepancy which exist between the calculations and the experiments in the γ-ray component of the decay heat in the cooling range from 300 to 3000 s after the fission event.

In our experiment separated parent activity produced by the IGISOL facility was carried to the centre of the Total Absorption Spectrometer (TAGS) by the tape transport system. The TAGS used was designed at the Nuclear Institute of St. Petersburg. It consist of two NaI(Tl) cylindrical crystals. The larger crystal has dimensions of $\varnothing = 200mm \times l = 200mm$ and has a longitudinal hole of $\varnothing = 43mm$. The smaller crystal has dimensions: $\varnothing = 200mm \times l = 100mm$ (see more details in [3]). The sources were produced using a uranium fission target with proton beams of 30 MeV. Special care was taken to have clean sources by appropriate selection of collection and measuring time for the isotopes of interest. Analysis of the data is underway.

Acknowledgements

A. Algora recognises support from the EC contract MERG-CT-2004-506849, and from the János Bolyai research fellowship.

a) IFIC, CSIC-Univ. Valencia, Valencia, Spain

b) NPI, St. Petersburg, Russia

c) GSI, Darmstadt, Germany

d) Univ. of Jyäskylä, Jyäskylä, Finland

e) Univ. of Surrey, Guildford, UK

f) Univ. of Washington, Seattle, USA

g) V.G. Khlopin Radium Institute, St. Petersburg, Russia

[1] J.C. Hardy, *et al.*, Phys. Letts 71B (1977) 307.

[2] T. Yoshida, *et al.*, Journal of Nucl. Science and Technology 36 (1999) 135

[3] A. Algora, Atomki Annual Report 2004, p. 17.

2.15 Monte Carlo simulations of the NPI total absorption spectrometer geometry

A. Algora

Optimising the geometry of an experimental setup can be of interest in particular experimental situations. In the case of the use of a total absorption spectrometer in beta decay studies, one of the priorities is to have the highest possible total efficiency for gamma rays, since it has been shown that the higher the efficiency of the setup, less is the dependence of the results of the analysis on the knowledge of the level scheme of the daughter nucleus [1]. The most cost-effective way for optimising a setup is by means of Monte Carlo techniques.

The total absorption technique is based on the principle of summing the gamma cascades that follow the β decay instead of detecting the individual gamma rays. In this way, we can have a device which is sensitive to the β population of the levels. A total absorption gamma spectrometer (TAGS) can be constructed using a large scintillator crystal which covers 4π relative to the source.

We have recently performed an experiment at the IGISOL facility in Jyväskylä in order to study the β decay of some isotopes relevant to the decay heat problem [2]. In the experiment we use a TAGS, which was designed at the Nuclear Institute of St. Petersburg. It consists of two NaI(Tl) cylindrical crystals. The larger crystal has dimensions of $\varnothing = 200mm \times l = 200mm$ and has a longitudinal hole of $\varnothing = 43mm$. The smaller crystal has dimensions: $\varnothing = 200mm \times l = 100mm$ (see Fig. 1 for an schematic view) [3]. As part of the preparation for the experiment we have simulated what is the optimal geometry of the setup depending on the position of the sources inside the larger crystal. The position of the sources is measured from one side of the larger crystal (x coordinate in Fig. 1). The simulations were performed using the Monte Carlo code GEANT4 [4]. Our results showed that the total efficiency for gamma rays of different energies has two maxima, the first is the trivial one, when we place the sources in the centre of the larger crystal ($x = -10cm$). The other maximum, the one with largest total efficiency, can be obtained when the sources are placed at a position of $x \sim -5cm$. More complex simulations, which are necessary for the analysis of our experiment and require the implementation of the geometry in great detail, are underway.

Figure 1. Schematic view of the TAGS geometry. In the experiments the sources are positioned along the longitudinal hole of the larger crystal. In the real experiment the sources were positioned in the place where the largest total efficiency was obtained from the simulations.

Acknowledgements A. Algora recognises support from the EC contract MERG-CT-2004-506849, and from the János Bolyai research fellowship.

[1] D. Cano-Ott, PhD Thesis (Univ. Valencia 2000), J.L. Tain and D. Cano-Ott unpublished

[2] Proposal I77, Univ. of Jyväskylä (Spokespersons: A. Algora, J.L. Tain)

[3] L. Batist, J.L. Tain, A. Gadea, private communication

[4] S. Agostinelli *et al.*, Nucl. Inst. and Meth. A506 (2003) 250, URL http://wwwasd.web.cern.ch/wwwasd/geant4/geant4.html

2.16 Evidence for chirality in ^{105}Rh

J. Timár, P. Joshi[a], K. Starosta[b,c], V.I. Dimitrov[d], D.B. Fossan[c]3, J. Molnár, D. Sohler, R. Wadsworth[a], A. Algora, P. Bednarczyk[e,f], D. Curien[e], Zs. Dombrádi, G. Duchene[e], A. Gizon[g], J. Gizon[g], D.G. Jenkins[a], T. Koike[c,h], A. Krasznahorkay, E.S. Paul[i], P.M. Raddon[i], G. Rainovski[c,i]4, J.N. Scheurer[j], A.J. Simons[a], C. Vaman[c], A.R. Wilkinson[a], L. Zolnai, S. Frauendorf[k]

High-spin states in ^{105}Rh were populated by the ^{96}Zr(^{13}C,p3n) reaction at beam energies of 51 and 58 MeV, and studied using the EUROBALL IV γ-ray spectrometer and the DIAMANT charged particle array. A pair of nearly degenerate ΔI=1 three-quasiparticle bands (bands 4 and 5 in Fig. 1) with the same spins and parity have been observed. Comparison of the experimental results with tilted axis cranking calculations (see Fig. 2) confirms the chiral character of the two bands, while arguments based on the excitation of particles within the $\pi g_{9/2}\nu(h_{11/2})^2$ configuration of the yrast band and comparison with the previously observed γ band (band 2) exclude the other possible interpretations. This is the first experimental evidence for three-quasiparticle chiral structure in the A$\sim$100 region, and the first simultaneous observation of a γ band and chiral partner bands in one nucleus. The results are published in Ref. [1].

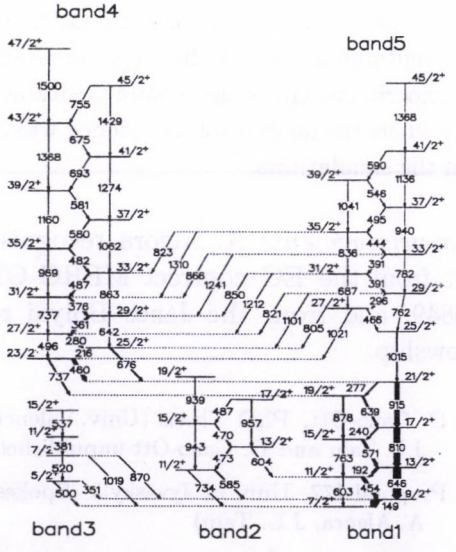

Figure 1. Partial level scheme of ^{105}Rh obtained in the present work.

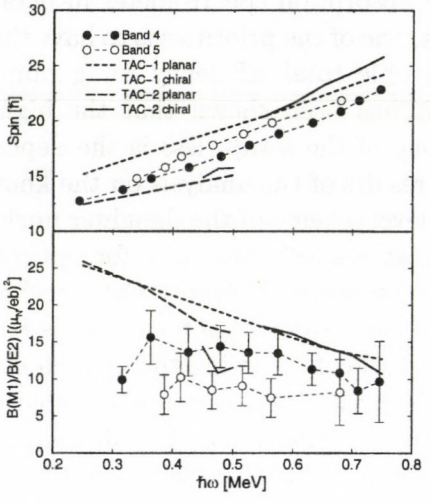

Figure 2. Comparison of the experimental values and TAC predictions for the chiral bands. TAC-1 and TAC-2 correspond to calculations without and with neutron pairing, respectively.

a) Department of Physics, University of York, York, YO10 5DD, UK

b) NSCL, Cyclotron Laboratory, Michigan State University, East Lansing, MI 48824-1321, USA

c) Department of Physics and Astronomy, SUNY, Stony Brook, New York, 11794-3800, USA

d) Department of Physics, University of Notre Dame, Notre Dame, Indiana 46556, USA

e) IReS, 23 rue du Loess, Strasbourg, 67037, France

f) GSI, Darmstadt, Germany

g) LPSC, IN2P3-CNRS/UJF, F-38026 Grenoble-Cedex, France

h) Department of Physics, Tohoku University, Sendai, Japan

i) Oliver Lodge Laboratory, Department of Physics, University of Liverpool,Liverpool L69 7ZE, UK

j) Université Bordeaux 1, IN2P3- CENBG - Le Haut-Vigneau BP120 33175, Gradignan Cedex, France

k) IHK Forschungszentrum Rossendorf, PF 510119, 01314 Dresden, Germany

[1] J. Timár, et al., Phys. Lett. B 598 (2004) 178.

[3]Deceased

[4]On leave of absent from Faculty of Physics, St. Kliment Ohridski University of Sofia, BG-1164 Sofia, Bulgaria

2.17 Alpha capture cross section of ^{106}Cd for the astrophysical p-process

Gy. Gyürky, Z. Elekes, Zs. Fülöp, G.G. Kiss, E. Somorjai, A. Palumbo[a], M. Wiescher[a], J. Görres[a], W. Rapp[a], N. Özkan[a], R.T. Gürray[a], T. Rauscher[b]

The modeling of the astrophysical p-process - the production mechanism synthesizing the heavy, proton rich isotopes - requires the knowledge of the reaction rates of thousands of reactions playing a role in the p-process reaction network. The reaction rates of the (γ, α) and $(\gamma$,p) reactions important for the p-process are calculated from the cross section estimates of statistical model calculations since experimental data are very scarce in the mass and energy region of the p-process. In order to check the calculated cross sections and to put the p-process models on a more reliable base, the experimental determination of (α, γ) and (p,γ) cross sections is very important since from the measured cross sections the astrophysically important, inverse (γ, α) and (γ,p) cross sections can be determined.

Owing to a big experimental effort of recent years, there is an increasing number of (p,γ) reactions measured for the p-process. For (α, γ) reaction, however, there are still very few investigated cases (see e.g. [1,2]). Therefore the aim of the present work is to extend the existing database for (α, γ) reactions by measuring the cross section of the ^{106}Cd$(\alpha, \gamma)^{110}$Sn reaction. As a side result, the cross section of the ^{106}Cd$(\alpha, n)^{109}$Sn and ^{106}Cd$(\alpha, p)^{109}$In reactions has also been measured.

The cross section of the above reactions has been determined using the activation technique [3]. Highly enriched ^{106}Cd targets have been irradiated with an α-beam in the energy range between 8 and 12.5 MeV (the relevant energy region of the astrophysical p-process). The irradiations have been carried out both at the cyclotron of the ATOMKI and at the tandem accelerator of the Notre Dame University, Indiana, USA. The γ-radiation following the β decay of the ^{110}Sn, ^{109}Sn and ^{109}In reaction products has been measured using calibrated HPGe detectors.

The obtained cross sections are compared with the predictions of Hauser-Feshbach statistical model calculations using the NON-SMOKER code [4]. The influence of the model parameters on the goodness of the predictions are also examined. The final analysis is still in progress, however the first results show that the model is able to reproduce the energy dependence of the cross sections and the absolute values are reproduced within a factor of 2. As an example, Fig. 1 shows the ATOMKI experimental results for the ^{106}Cd$(\alpha, \gamma)^{110}$Sn reaction and the NON-SMOKER predictions using the standard input parameters [4].

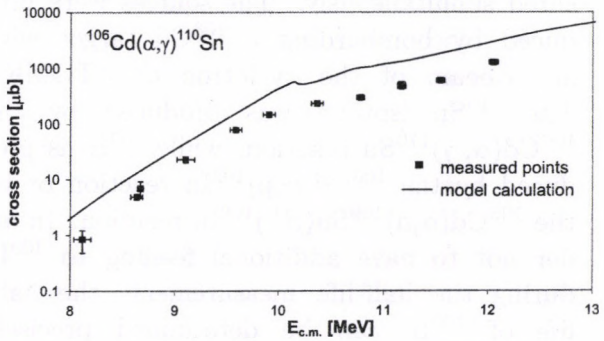

Figure 1. Measured cross section of the ^{106}Cd$(\alpha, \gamma)^{110}$Sn reaction and the NON-SMOKER model prediction.

a) University of Notre Dame, Notre Dame, Indiana 46556, USA

b) Universität Basel, CH-4056 Basel, Switzerland

[1] Zs. Fülöp et al., Z.Phys. A 355 (1996) 203.

[2] E. Somorjai et al., Astron. Astrophys. 333 (1998) 1112.

[3] Gy. Gyürky et al., Nucl. Phys. A in press (preliminary results)

[4] T. Rauscher and F. K. Thielemann, At. Data Nucl. Data Tables 79 (2001) 47.

2.18 Precise half-life measurement of ^{110}Sn and ^{109}In isotopes

Gy. Gyürky, Z. Elekes, Zs. Fülöp, G.G. Kiss, E. Somorjai, A. Palumbo[a], *M. Wiescher*[a]

Recently, the ^{106}Cd$(\alpha,\gamma)^{110}$Sn and ^{106}Cd$(\alpha$,p$)^{109}$In cross sections have been measured in the energy range relevant to the astrophysical p-process [1]. The cross sections are obtained by the activation method where the γ-radiation that results from the β-decay of the reaction products ^{110}Sn ($T_{1/2,adopted} = 4.11 \pm 0.10$ h) and ^{109}In ($T_{1/2,adopted} = 4.2 \pm 0.10$ h) is measured. The precise knowledge of the half-lives of the reaction products is crucial for a reliable cross section determination with the activation technique. Since the Sn and In half-lives have relatively large errors, a new determination of these half-lives is highly needed.

In the present experiment the half-lives of ^{110}Sn and ^{109}In isotopes have been measured simultaneously. The sources were produced by bombarding a ^{106}Cd target with an α-beam of the cyclotron of ATOMKI. The ^{110}Sn isotope was produced by the ^{106}Cd$(\alpha,\gamma)^{110}$Sn reaction, while ^{109}In is produced by the ^{106}Cd$(\alpha$,p$)^{109}$In reaction or by the ^{106}Cd$(\alpha$,n$)^{109}$Sn$(\beta^+)^{109}$In reaction. In order not to have additional feeding to ^{109}In during the half-life measurement, the half-life of ^{109}In can be determined precisely only after ^{109}Sn has decayed completely ($T_{1/2} = 18.0 \pm 0.2$ m); therefore, the gamma-counting has been started 6 hours after the end of the irradiation.

The irradiated sample has been placed in front of a HPGe detector in a holder fixed rigidly onto the end cap of the detector. Directly at the back of the sample a ^{7}Be source has been put in the holder in order to be able to control any possible change in the detection geometry or the efficiency of the detector during the counting. The decay of the ^{110}Sn and ^{109}In isotopes has been followed for 24 hours (roughly 6 half-lives) recording the γ-spectra in every 15 minutes.

The half-lives of the two isotopes were determined also by normalizing the γ-intensities from ^{110}Sn and ^{109}In with the number of counts from ^{7}Be reference source. The slight change of the ^{7}Be activity ($T_{1/2} = 53.22 \pm 0.06$ days) during the one day γ-counting has been taken into account. The half-lives have been determined from the parameters of the exponential fit to the measured data. As an example, Fig. 1. shows the decay curve of the ^{110}Sn isotope without normalization.

Table 1. Obtained half-lives for the two measured isotopes

	Half-life [hours]		
	without normalization	normalized to ^{7}Be	weighted average
^{110}Sn	4.179 ± 0.023	4.165 ± 0.035	4.173 ± 0.023
^{109}In	4.168 ± 0.018	4.166 ± 0.022	4.167 ± 0.018

Table 1. shows the results for both isotopes obtained without and with normalization to ^{7}Be. The two methods give the same result within the error bar for both isotopes. The weighted averages are listed in the last column of the Table. Our final result for the half-life of ^{110}Sn is $\mathbf{T_{1/2} = 4.173 \pm 0.023\ h}$ which is in good agreement with the adopted value but its error is reduced from 2.4 to 0.5 %. The same holds for ^{109}In where the obtained half-life, $\mathbf{T_{1/2} = 4.167 \pm 0.006\ h}$ is again in agreement with the adopted value.

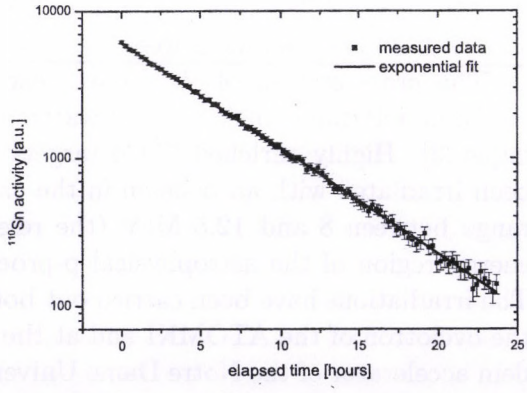

Figure 1. Decay of ^{110}Sn measured for 24 hours. The solid line is the exponential fit to the measurement.

a) University of Notre Dame, Notre Dame, Indiana 46556, USA

[1] Gy. Gyürky et al., Nucl. Phys. A in press.

2.19 Quadrupole deformation and clusterization in nuclei

J. Cseh, A. Algora, J. Darai[a)], P.O. Hess[b)],

The investigation of exotic nuclear shapes, e.g. superdeformed and hyperdeformed states (in which the atomic nucleus has a spheroidal shape with ratios of main axes of 2:1 and 3:1, respectively) is one of the most interesting topics in recent nuclear structure studies. The appearance of exotic cluster configurations (or exotic cluster decay) is another issue of utmost interest. The combination of these two problems brings us to an exciting question: what is the interrelation of these two phenomena, i.e. what are the possible clusterizations of nuclear states with exotic shape. Recently we have addressed this question from the angle of both the binary [1] and the ternary [2] clusterizations. We apply methods which can be generalised for more complicated multicluster-configurations in a straightforward way.

The basic concept of this work is that when we describe the composition of an atomic nucleus from smaller nuclei (clusters) then we take into account both of the two complementary natural laws, which govern this kind of phenomenon: the energy-minimum principle and the Pauli-exclusion principle. The crucial role of these two rules are obvious: energetically unfavoured systems are not likely to appear, and when the building blocks are fermions, like the nucleons of the atomic nuclei, then they follow the exclusion principle. However, the exact role, or relative importance of these two aspects of clusterization among different circumstances are not completely understood yet; the present work is meant to be a contribution to this task.

Much attention has been paid to the energetic preference of various cluster-configurations of a nucleus. The methods applied along this line are partly or completely empirical ones, using information of the experimental data. Furthermore, most of these works concentrate on the simplest, i.e. binary clusterizations, especially, when the energetic calculation involves (in addition to the experimental binding energies) intercluster potentials, like in the dinuclear system model [3], or in the local potential approach [4]. On the other hand the treatment of the exclusion-principle has to be done microscopically, therefore, apart from the light, or simplest heavy nuclei, it gives rise to very big computational difficulties. Due to this fact no systematic studies has been done, and many of the experimentally interesting systems are untouched from this viewpoint.

The main point of our work is that we present a method for the approximative treatment of the exclusion principle, which can be applied both to binary [1] and ternary [2] (and even to multi) cluster-configurations, and we combine this microscopic approach with an empirical method of the calculation of the energetic preference. This latter quantity is obtained in a similar way as in the work [5] with a straightforward generalisation for ternary clusterization. In this way both aspects of the clusterization (i.e. energy-minimum and exclusion principles) can be handled, therefore, their interrelation can be studied in specific problems. The exclusion-principle is taken into account by a selection rule, based on the real [6] or effective [7] $U(3)$ symmetry for light and heavy nuclei, respectively. This symmetry-based consideration can also be very involved for heavy nuclei, nevertheless, it seems to be widely applicable.

As specific examples we consider binary and ternary cluster-configurations in the ground, superdeformed and hyperdeformed states of the light ^{36}Ar and heavy ^{252}Cf nuclei. In case of ^{36}Ar the superdeformed state has been found experimentally [8], and a theoretical prediction is available for its hyperdeformed state [9]. In case of ^{252}Cf the main motivation is provided by the spontaneous fission experiments from its ground state, which indicated several very exotic clusterizations [10]. As for superdeformed and hyperdeformed states of this nucleus, we consider hypothetical states with appropriate deformations ($\epsilon = 0.6$

and $\epsilon = 0.86$ respectively).

The main conclusions of our studies are as follows. Our results clearly indicate that the two considerations, based on the microscopic structure on the one hand side, and on the energetic stability on the other hand side, do not necessarily result in the same preference of cluster configurations. The most likely clusterizations are probably those ones, which are in the overlapping regions of the preferences of the two complementary selecting procedures.

For the binary clusterization the structural selection rule has similar tendency for the deformation-dependence both in the case of the light ^{36}Ar nucleus, and in the heavy ^{252}Cf nucleus. In the ground-state the strongly asymmetric binary cluster-configurations are preferred, in the hyperdeformed state the symmetric fragmentations are more likely, while in the superdeformed state the situation is in between, i.e. islands of allowed binary configurations appear. Considering the energetic stability as well, for the ^{252}Cf the $Z_{light} = 2$, 20, and 48 regions are preferred in the ground, superdeformed, and hyperdeformed states, respectively.

Another interesting finding is that the same clusterization appears both in the ground-state and in the superdeformed and hyperdeformed states of ^{36}Ar. In this case the ^{24}Mg+^{12}C binary and the ^{24}Mg+^{8}Be+^{4}He, ^{20}Ne+^{4}He+^{12}C, and ^{16}O+^{8}Be+^{12}C, ternary clusterizations are allowed in each of the three states. Furthermore, they are energetically favoured as well. (Please, note the similarity of the binary and ternary configurations adding in the first ternary case the last two clusters and in the last two cases the first two clusters, compared to the binary case!) The reason for the appearance of the same cluster-configuration in different states is that if the deformation of the clusters is taken into account, and their different orientations are allowed in the description, then different spatial configurations of the same clusters may result in states of the parent nucleus with very different quadrupole deformation. This is the same observation, which was made for the molecular states of light nuclei both in the two-center shell model [11] and in the cluster models [12,13], when unconstrained calculations were carried out (without requiring e.g. cylindrical symmetry in the calculation).

a) Univ. of Debrecen, Inst. of Exerimental Physics

b) Inst. de Ciencias Nucleares, UNAM, Mexico

[1] J. Cseh, A. Algora, J. Darai, P. O. Hess, Phys. Rev. **C70** (2004) 034311.

[2] A. Algora, J. Cseh, J. Darai, P. O. Hess, in preparation.

[3] T. M. Schneidman, G. G. Adamian, N. V. Antonenko, R. V. Jolos, W. Scheid, Phys. Rev. **C67** (2003) 0143113, and references therein.

[4] B. Buck, A. C. Merchant, S. M. Perez, Phys. Rev. Lett. **76** (1996) 380, and references therein.

[5] B. Buck, A. C. Merchant, and S. M. Perez, Few-Body Systems **29** (2000) 53;
B. Buck, A. C. Merchant, M. J. Horner, and S. M. Perez, Phys. Rev. C**61** (2000) 024314.

[6] J. P. Elliot, Proc. R. Soc. A **245** (1958) 128, 562.

[7] P. Rochford, D.J. Rowe, Phys. Lett B **210** (1988) 5;
D. J. Rowe, P. Rochford, J. Repka, J. Math. Phys. **29** (1988) 572;
P. O. Hess, A. Algora, M. Hunyadi, and J. Cseh, Eur. Phys. J. A**15** (2002) 449.

[8] C. E. Svensson, et. al., Phys. Rev. Lett. **85** (2000) 2693;
C. E. Svensson, et. al., Phys. Rev. C**63** (2001) 061301(R).

[9] W. D. M. Rae and A. C. Merchant, Phys. Lett. B**279** (1992) 207.

[10] J. H. Hamilton et al, J. Phys. G**20** (1994) L85;
A. V. Ramaya et al, Phys. Rev. Lett. **81** (1998) 947.

[11] H. Chandra, U. Mosel, Nucl. Phys. **A298** (1978) 151.

[12] W. D. M. Rae, Int. J. Mod. Phys. **3** (1988) 1343.

[13] J. Cseh, W. Scheid, J. Phys. **G18** (1992) 1419.

2.20 Quasiparticle Resonances in the BCS Approach

R. Id Betan[a,b], *N. Sandulescu*[a,c] *and T. Vertse*

We use a simple method to evaluate the energies and the widths of quasiparticle resonant states in the BCS approach. This method is based on BCS equations formulated in Berggren representation. The formalism is derived from the HFB approach in coordinate space by neglecting the off-diagonal matrix elements of the pairing gap matrix. The Berggren repesentation is a complete single particle basis composed of bound states, complex energy resonant sates (Gamow states) and a complex continuum of scattering states along a contour [1]. The shape of the contour fixes the complex energy Gamow states icluded (from which the complex quasi particle energies are calculated). Truncated Berggren representations in which the effect of the non-resonant continum has been neglected were used before in BCS calculations [2]. However this truncation spoiled the independence of the results on the choice of the complex contour. In the present approach we use the full representation where the results should be independent of the contour. If the contour is along the real energy axis then we use the standard complet set of the bound states and real energy scattering states. Drawing the contour in the third quadrant of the complex k plane we can include certain Gamow resonances into the basis.

In our calculation the pairing gap of a quasiparticle resonance is obtained by integrating the pairing field with the Gamow wave function corresponding to the resonant state. But the continuum contribution to the pairing field is calculated by solving the BCS equations in a single-particle basis formed by bound states and real energy scattering states.

We apply the model to study the structure of even-even nuclei with closed proton and open neutron shells: ^{18}O, ^{20}O and ^{22}O. The effects of the ^{16}O core is simulated by phenomenological Woods-Saxon potentials. The single particle states obtained in the $s-d$ shell agree rather well with available experimental data for ^{17}O. We get the last bound $2s_{1/2}$ orbit at -3.262 MeV, a narrow $1d_{3/2}$ resonance at $(0.91-i0.05)$ MeV and a wide $1f_{7/2}$ resonance at $(7.45-i1.53)$ MeV. We use a density dependent local pairing interaction as in ref.[3] and a high energy cutoff at 10 MeV. Our calculation with the full real continuum corresponds to the continuum shell model type BCS calculation (CBCS). The p parameter of the interaction has been adjusted to reproduce the average pairing gap value 1.83 MeV for ^{20}O. The average gaps and the root-mean-square radii calculated in CBCS agree with those calculated using scattering states only from the vicintity of the resonances. This is a good approximation. But if we approximate the effect of the resonances by a single real energy scattering state (with real wave function renormalized inside a box with size 20 fm) we get considerable different values for both the average gap and the root-mean-square radii. Therefore the later seems to be a very poor approximation to the CBCS.

This work is partially supported by the Hungarian OTKA fund Nos. T37991 and T46791.

a) Royal Institute of Technology, Physics Department Frescati, Frescativagen 24, S-10405, Stockholm, Sweden.

b) Dept. de Fisica, FCEIA, UNR, Av. Pellegrini 250, 2000, Rosario, Argentina.

c) Royal Inst. of Phys. and Nucl. Eng., P.O. Box MG-6, Bucharest-Magurele, Romania.

[1] T. Berggren, Nucl. Phys. A **109**, 265 (1968).

[2] O. Civitarese, R.J. Liotta and T. Vertse, Phys. Rev. C **64**, 057305 (2001); A.T. Kruppa, P.-H. Heenen, R.J. Liotta, Phys. Rev. C **63**, 044324 (2001).

[3] G.F. Bertsch and H. Esbensen, Ann. of Phys. **209**, 327 (1991).

3.1 High Precision Laser Spectroscopy of Antiprotonic Helium Atoms

D. Horváth, B. Juhász, and the ASACUSA collaboration

The ASACUSA collaboration has continued the laser spectroscopy studies of antiprotonic helium atoms ($\bar{p}-e^- - He^{2+} \equiv \bar{p}He^+$) at the Antiproton Decelerator (AD) of CERN. In previous years, we could measure the wavelengths of several transitions between different energy levels of antiprotonic helium with a precision of ~100-ppb (10^{-7}) each [1]. Using our data and the antiprotonic charge/mass ratio measured previously to a very high precision by the TRAP collaboration, we could extract the best baryonic CPT (Charge-Parity-Time invariance) limit of $\delta = (q_p + q_{\bar{p}})/q_p = (m_p - m_{\bar{p}})/m_p = 10$ ppb [2], where $q_{p(\bar{p})}$ and $m_{p(\bar{p})}$ are the proton (antiproton) charge and mass, respectively.

In 2004, we could further increase the accuracy of our measurements, thanks to the following improvements:

- Instead of a pulsed dye laser, we used a continuous-wave (CW) titanium-sapphire or dye laser with a frequency bandwith of $< 10^{-10}$. The CW light was then amplified to a high-energy pulse using a pulsed Nd:YAG laser.

- The frequency of the CW laser was measured with a femtosecond optical comb generator with a relative accuracy of $\sim 10^{-12}$. The CW laser was locked to the comb generator, and their frequencies were swept across the $\bar{p}He^+$ resonance lines.

- Even though the frequency of the CW laser is accurately measured using the comb generator, the frequency of the pulse-amplified light is in general different from the input frequency. This frequency shift is called 'chirp'. To compensate for this, we used an electro-optic modulator. In addition, we recorded for each laser shot the beat note between the pulse-amplified laser light and the 400-MHz-shifted CW laser. The Fourier analysis of this beat note reveals the chirp, which was usually ±20 MHz in our case. After correction with this shift, the remaining uncertainty due to the chirp is reduced to ~1 MHz, which corresponds to a relative precision of $\sim 10^{-9}$.

- The pulse length τ_w of the amplifying Nd:YAG laser was increased with an optical delay line by a factor 10, so as to improve the Fourier limit $1/(2\pi\tau_w)$.

- One of the twelve transitions we measured was a metastable-to-metastable transition. Such transitions, unlike the metastable-to-short-lived transitions measured so far, have a much smaller linewidth. Besides, the accuracies of the three-body QED calculations are higher for transitions with smaller widths.

So far, experimental errors [1] and the scatter of the theoretical values [3,4] have been all about 100 ppb. With our 2004 results, the differences between the two sets of calculations have become the dominant error source when we deduce the proton-antiproton mass and charge CPT limits. When we finish analyzing our data and theorists finish updating their calculations, we hope to be able to determine the antiproton mass and charge to ~1 ppb.

Acknowledgements

Our work is supported by the Grant-in-Aid for Specially Promoted Research (15002005) of MEXT of Japan, and the Hungarian Scientific Research Fund (OTKA T046095 and TeT-Jap-4/00).

[1] M. Hori *et al.*, Phys. Rev. Lett. 91 (2003) 123401.

[2] S. Eidelman *et al.*, Phys. Lett. B 9592 (2004) 1.

[3] V.I. Korobov, Phys. Rev. A 67 (2003) 062501.

[4] Y. Kino, M. Kamimura, H. Kudo, Nucl. Instrum. Methods B 214 (2004) 84.

3.2 KLL resonant Auger transitions in metallic Cu and Ni

L. Kövér, W. Drube[a)], Z. Berényi, I. Cserny, V.R.R. Medicherla[a)]

KLL Auger spectra of *3d* transition metals contain important information on the effects of the solid environment on deep core Auger transitions. Following the changes in the spectra when fine tuning the exciting photon energy across the K-shell ionization threshold with high energy resolution is informative concerning the possible resonant processes, expected to indicate the single-step nature of threshold Auger emission. The satellite structures in these spectra are strongly related to the unoccupied local electronic states above the Fermi level, as well as to the excitation, relaxation and screening processes associated with core hole ionization. In spite of the fundamental significance of the phenomena mentioned above, even non resonant high energy resolution studies of KLL Auger spectra of *3d* transition metals (using laboratory X-ray sources) are very scarce due to the demanding experimental conditions requested [1-3].

A very efficient tool for studying these phenomena is the Tunable High Energy XPS developed at HASYLAB which provides unique conditions, photon flux and energy resolution for deep core Auger spectroscopy [4-6].

Using the THE-XPS instrument at the BW2 beamline the high energy resolution ($\Delta E = 0.2$ eV) $KL_{2,3}L_{2,3}$ Auger spectra of polycrystalline Cu and Ni foils were measured with the Scienta SES-200 hemispherical analyzer. In the high energy range Cu 2p photoelectron peaks appearing in the Cu KLL Auger spectra due to the excitation by internal Cu K X-rays and trusted value for the Cu 2p3/2 binding energy [7] were used for energy calibration. The exciting photon energy range was tuned up to about 50 eV above the K absorption edge and for the resonant energy region to 5 eV (Cu KLL) and 4 eV (Ni KLL) below threshold ensuring a photon beam with an energy width of about 1.1 eV.

The evolution of the satellite structure as a function of excitation energy above threshold indicates different behaviour for particular satellites, making possible to separate initial state and final state effects. For illustration of the results, Fig. 1 shows the Cu KLL Auger spectra measured in the resonant exciting photon energy region. In the spectra the linear dispersion of the peak energy positions with lowering the photon energy below the ionization threshold, as a signature of the Auger resonant Raman process can be clearly seen. Similar tendency is observed in the respective Ni KLL Auger spectra.

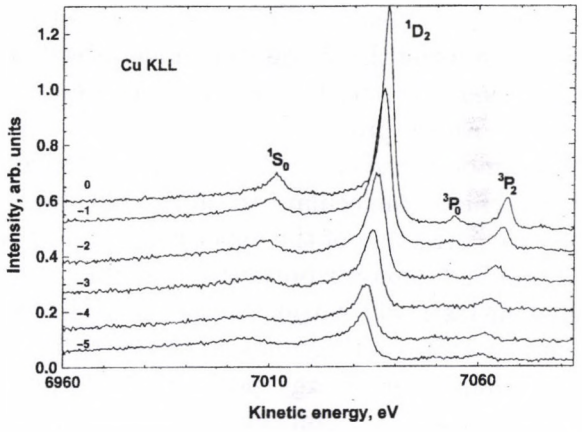

Figure 1. The evolution of the Cu KLL spectra photoexcited from polycrystalline metal using photon energies at and below the ionization threshold (relative energy values - in eV - are indicated).

This work was supported by the IHP-Contract HPRI-CT-1999-00040/2001-00140 of the European Commission and by the Hungarian project OTKA T038016.

a) HASYLAB/DESY, Notkestraße 85, 22603 Hamburg, Germany

[1] L. Kövér et al, J. Electron Spectrosc. Relat. Phenom. 114-116 (2001) 55.

[2] L. Kövér et al, Surf. Sci. 433-435 (1999) 833.

[3] A. Némethy et al, J. Electron Spectrosc. Relat. Phenom. 82 (1996) 31.

[4] W. Drube, R. Treusch, Physica B208 (1995) 33.

[5] W. Drube et al, Phys. Rev. Lett. 74 (1995) 42.

[6] W. Drube et al, Phys. Rev. B60 (1999) 15507.

[7] M.P. Seah, J. Electron Spectrosc. Relat. Phenom. 97 (1998) 235.

3.3 Resonant KLL Auger spectra of ferromagnetic metals Fe and Co

L. Kövér, W. Drube[a)], Z. Berényi, I. Cserny, V.R.R. Medicherla[a)]

Resonant KLL Auger spectra of 3d transition metals contain important information on the nature of the Auger process including solid state effects due to changes in the electronic structure local to the initial state core hole [1].

Tuning the energy of the monochromatic exciting photons across the K-absorption edge, features characteristic to resonant phenomena can be reflected in the spectra [2]. In the case of the resonantly photoexcited KLL Auger spectra induced from Cu and Ni metals, the spectral shapes have been successfully described using the single step model based on the resonant scattering theory [3] for describing the Auger process. The *4p* partial density of unoccupied electronic states was derived from a cluster molecular orbital model, while a realistic correction of the experimental spectra was applied for contributions of electrons scattered inelastically within the samples [4]. As a function of exciting photon energy, a linear dispersion of the energy position of the peak maximum and a significant distortion of the peak shape was found, indicating the presence of the Auger Resonant Raman effect [4].

For observing resonantly photoexcited KLL Auger transitions in *3d* metals and studying threshold dynamics of Auger satellites the Tunable High Energy XPS (THE XPS) facility at the BW2 beamline of HASYLAB provides optimum conditions [4-6].

KL_2L_3 Auger spectra of polycrystalline Fe and Co were measured using the THE-XPS instrument with the SES-200 analyser with an energy resolution of 0.2 eV. For electron energies exceeding 5 keV, a proper positive bias voltage was applied on the sample. Energy calibration of the energy scale was performed by using reference data [7] for Cu L_3VV and Au $M_5N_{67}N_{67}$ Auger lines as well as for Cu *2p* photolines excited by K_α X-rays photoinduced internally in the calibrating Cu sample. Using Si (220) (Fe) and Si (111) (Co) monochromators ensuring a photon beam energy width of 1.1 eV, KLL spectra were obtained down to 3 eV (Fe) and 2 eV (Co) photon energies below K-threshold.

Fig. 1 shows the Fe KLL spectra recorded at threshold and sub-threshold excitations, indicating the signature of the Auger Resonant Raman process. Similar results were obtained for the resonant Co KLL spectra.

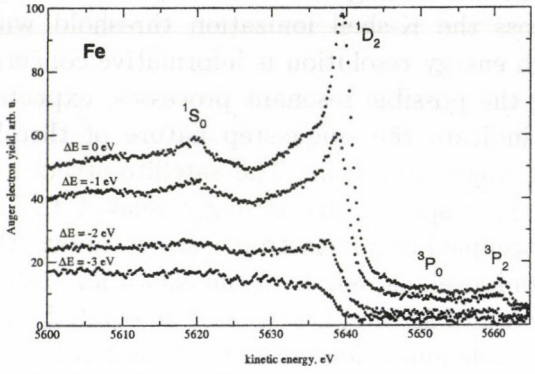

Figure 1. The evolution of the Fe KLL Auger spectra photoexcited from a polycrystalline metal sample using photon energies at and below the K-shell photoionization threshold.

This work was supported by the IHP-Contract HPRI-CT-199-0040/2001-00140 of the European Commission and by the Hungarian Project OTKA T038016.

a) HASYLAB/DESY, Notkestraße 85, 22603 Hamburg, Germany

[1] L. Kövér, I. Cserny, J. Tóth, D. Varga, T. Mukoyama, J. Electron Spectrosc. Relat. Phenom. 114-116, 55 (2001).

[2] L. Kövér, W. Drube, Z. Berényi, I. Cserny, V.R.R. Medicherla, HASYLAB Annual Report 2002, Pt. 1, 671 (2003).

[3] W. Drube, R. Treusch , G. Materlik, Phys. Rev. Lett. 74, 42 (1995).

[4] L. Kövér, W. Drube, Z. Berényi, I. Cserny, V.R.R. Medicherla, T. Ishii, H. Ikeno, H. Adachi, submitted for publication.

[5] W. Drube, T.M. Grehk, R. Treusch, G. Materlik, J. Electron Spectrosc. Relat. Phenom., 88-91, 683 (1998).

[6] W. Drube, T.M. Grehk, R. Treusch, G. Materlik, J.E. Hansen, T. Lberg, Phys. Rev. B60, 15507 (1999).

[7] M.P. Seah, J. Electron Spectrosc. Relat. Phenom. 97, 235 (1998).

3.4 Mn KLL Auger transitions in MnO nanolayers – a high energy resolution study

L. Kövér, W. Drube[a)], I. Cserny, Z. Berényi and S. Egri

Highly resolved KLL Auger spectra provide a unique tool for obtaining chemical state information from deeply buried interfaces even in the case of very thin, several nm thickness interface layers. The case of the Mn KLL spectra in MnO is interesting because in our earlier study on polycrystalline MnO showed the presence of an intense extra peak in the spectra at the low kinetic energy side of the main $^1D_2$ Auger line which cannot be seen in the respective spectra of the polycrystalline metal [1]. For obtaining more details, necessary to determine the origin of this extra peak needs a significantly higher energy resolution and intensity, as well as a very thin layer sample in order to eliminate most of the contribution to the spectra from electrons scattered inelastically.

MnO nanolayers of 2 nm thickness were prepared in situ by evaporating high purity Mn metal onto a thoroughly degassed glassy carbon wafer and heating in oxygen atmosphere. The partial oxygen pressure was 2×10^{-5} mbar and the wafer was kept at a temperature of 1000 K during oxidation.

The measurements of the Mn $KL_{23}L_{23}$ Auger spectra of the MnO nanolayers were performed with the Tunable High Energy XPS instrument [2] of the BW2 synchrotron beamline (HASYLAB) equipped with a Scienta SES-200 hemispherical analyser using high electron energy resolution (0.2 eV). Mn $2p$, $3s$ and VB spectra of the sample confirmed that the single phase nanolayer on the surface of the supporting carbon wafer was pure MnO.

Fig. 1a shows the Mn $KL_{23}L_{23}$ spectrum excited by photons (14 eV above the K-shell ionization threshold) from a MnO nanolayer in comparison with the spectrum (excited by bremssstrahlung) of a polycrystalline MnO sample (Fig. 1b) [1]. The striking difference between the two spectra in energy resolution, intensity and regarding the inelastic background is obvious.

On the basis of the similarity between its energy separation from the main $^1D_2$ Auger peak and the multiplet splitting in the $3s$ photoelectron peak, the "extra peak" can be attributed to multiplet splitting. This seems to be confirmed by its continuing presence in the resonant Auger spectra excited using subthreshold photon energies, as shown by the preliminary results.

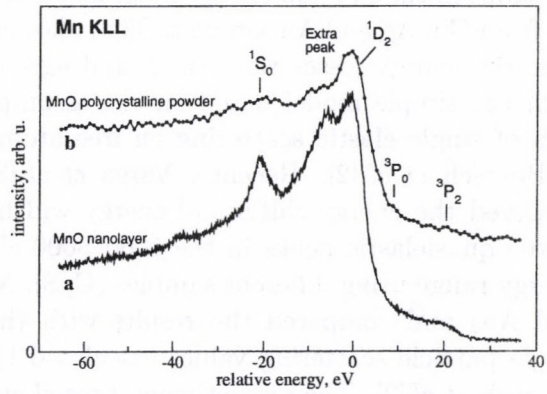

Figure 1. Mn $KL_{23}L_{23}$ Auger spectra excited by monochromatic photons 14 eV above the K-shell ionization threshold from a MnO nanolayer (a) and by bremsstrahlung from polycrystalline powder [1] (b) The kinetic energy is measured relative to the $^1D_2$ line at 5203.3 eV [1].

Acknowledgements

This work was supported by the European Community Research Infrastructure Action under the FP6 "Structuring the European Research Area" Programme (through the Integrated Infrastructure Initiative "Integrating Activity on Synchrotron and Free Laser Science") and by the Hungarian Project OTKA T038016.

a) HASYLAB/DESY, Notkestraße 85, 22603 Hamburg, Germany

[1] A. Némethy, L. Kövér, I. Cserny, D. Varga and P. B. Barna, J. Electron Spectrosc. Relat. Phenom. 70, 183 (1995).

[2] W. Drube, T. M. Grehk, R. Treusch and G. Materlik, J. Electron Spectrosc. Relat. Phenom. 88-91, 683 (1998).

3.5 Angle and atomic number dependent energy shift in elastic scattering for free atoms and molecules

T. Ricsóka, S. Ricz, Á. Kövér, D. Varga and Z. Berényi

During the past decade the elastic scattering of low-, medium- and high energy electrons from solids and liquids has been investigated experimentally and theoretically. This phenomenon is the physical basis of the surface sensitive electron spectroscopy. Laser and Seah [1] studied the quasielastic scattering of electrons in the electron energy range 250–3000 eV from Cu, Ag and Au samples. They showed that the energy losses were small and agreed with the simple model based on the assumption of single elastic scattering on free atoms of Boersch *et al* [2]. Recently Varga *et al* [3] analyzed the energy shifts and energy widths of the quasielastic peaks in the 1000–5000 eV energy range using different samples (C, Si, Ni and Au) and compared the results with the single particle scattering values calculated by Boersch *et al* [2]. Their experimental recoil energy shifts and broadenings were in good agreement with the formula of Boersch for Ni and Au samples, but in the case of Si and C they found larger energy broadening than the calculated one.

In order to test the validity of the simple model of Boersch [2] for free atoms and molecules, we measured the energy shift of the elastic peak using different targets (Ar, He and CH_4) in the 1000–2500 eV primary electron energy range. Since the energy losses are small, the scattered electrons were analyzed with the high energy resolution electron-spectrometer (ESA-21). The scattered electrons are detected simultaneously by 13 channeltrons between 0° and 120° relative to the direction of the incident electron beam.

In the present impact energy range the electrons scatter from the nuclei of the molecule. Due to the big mass difference of the carbon and hydrogen nuclei in the methane we could separate the elastic peaks from the carbon and hydrogen. Figure 1 shows the position of the hydrogen elastic peak relative to the carbon one as a function of the scattering angle at 1000 eV impact energy. The experimental data agree well with the results of the simple model calculated by Boersch *et al* [2].

This is the one of the first experimental data for the energy shift of the elastically scattered electron from free atoms and molecules.

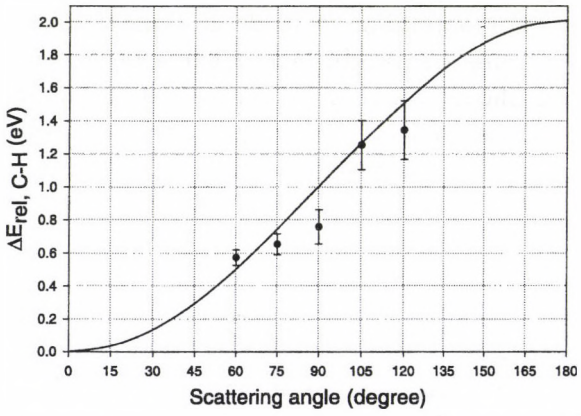

Figure 1. Comparison between the theoretical and experimental energy shift of the elastic peak of hydrogen relative to the carbon one for methane target at 1000 eV impact energy. Black full circles show the experimental data, whereas black solid line represents the results of the model of Boersch [2].

Acknowledgements

This work was supported by the Hungarian Scientific Research Foundation (OTKA Grant No: T037203).

[1] D. Laser, M. P. Seah, Phys. Rev. B **47** (1993) 9836.

[2] H. Boersch, R. Wolter, H. Z. Schoenebeck, Z. Physik **199** (1967) 124.

[3] D. Varga, K. Tőkési, Z. Berényi, J. Tóth, L. Kövér, G. Gergely and A. Sulyok, Surf. Interface Anal. **31** (2001) 1019.

3.6 Accelerating multiple scattering of the emitted electrons in collisions of ions with atoms and molecules

T. Ricsóka, Gy. Víkor[a)], Sz. Nagy[a)], K. Tőkési, Z. Berényi, B. Paripás[b)], N. Stolterfoht[c)] and B. Sulik

Ionization is one of the fundamental phenomena studied in atomic collision physics. Double differential spectra of electrons ejected in ion-atom and ion-solid collisions provide detailed information about the ionization dynamics. During the past decade special emphasis have been laid on the emission of the fast electrons in collisions of heavy partners [1]. Significantly enhanced emission of fast electrons above the binary encounter energy was observed in both ion-atom [2] and ion-solid collisions [3]. In some cases, the fast electrons have been identified as originated from double [4] or multiple [2] scattering by the projectile and target cores. Since the moving projectile ion is much heavier than the electron, such kind of multiple scattering of the electron also accelerates it. The process is often denoted as Fermi-shuttle acceleration [1].

In the present work, we measured the double differential cross-sections for electron emission in collisions of 700–1500 keV N^+ ions with N_2, Ne and Ar targets. We studied the target atomic number (Z_T) dependence of the yield of the Fermi-shuttle type triple and quadruple scattering in these collisions.

We performed classical trajectory Monte-Carlo calculations for the target ionization. Figure 1 compares the present experimental double differential cross sections with the results of the CTMC calculation for electron emission at 30°, 90° and 150° in 0.75 MeV N^+ + Ar collisions as a function of the ejected electron energy. The experimental double differential cross-sections are in good agreement with the theoretical values, and all the expected target ionization structures (P, P-T, P-T-P and P-T-P-T) clearly appear in the spectra.

We consider the present work as a starting point of a systematic study, a combined experimental and CTMC analysis of a wide range of collision systems.

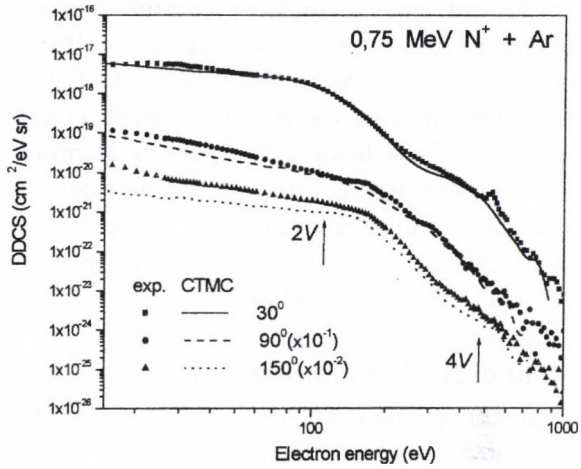

Figure 1. Experimental double differential cross section in comparison with theoretical CTMC results for electron emission at 30°, 90° and 150° in 0.75 MeV N^+ + Ar collisions as a function of the ejected electron energy.

Acknowledgements

This work was supported by Hungarian OTKA Grants (T046905, M27839) and by the Hungarian-Swedish KVA-collaboration.

a) Department of Atomic Physics, Stockholm University, 10405 Sweden

b) Department of Physics, University of Miskolc, 3515 Miskolc-Egyetemváros, Hungary

c) Hahn-Meitner Institute Berlin, D-14109 Berlin, Germany

[1] B. Sulik, N. Stolterfoht, R. Hellhammer, Z. Pesic, Cs. Koncz, K. Tokési, D. Berényi, Nucl. Inst. and Meth. B **212** (2003) 32.

[2] B. Sulik, Cs. Koncz, K. Tokési, A. Orbán, D. Berényi, Phys. Rev. Lett. **88** (2002) 073201.

[3] R. A. Baragiola, E. V. Alonso, A. Oliva, A. Bonnano, F. Xu, Phys. Rev. A **45** (1992) 5286.

[4] S. Suárez, R. O. Barrachina, and W. Meckbach, Phys. Rev. Lett. **77** (1996) 474.

3.7 Higher-order effects in the photoionization of 3p shell of argon

T. Ricsóka, S. Ricz, Á. Kövér, R. Sankari[a)], J. Nikkinen[a)], D. Varga and S. Aksela[a)]

The angular distribution of electrons ejected in atomic photoionization process gives detailed information on the structure of atoms, the dynamics of the process and the multielectron correlation effects. The $2p^{-1}ns(nd)$ photoexcited states in argon were studied by Gorczyca and Robicheaux [1] with the R-matrix method considering interference between the direct photoionization and the resonant excitation participator autoionization. They found that the interference plays important role in the accurate description of the angular distribution of Ar $3p$ photoelectrons.

In the present work, the angular distribution of $3p$ photoelectrons of argon was measured with linearly polarized synchrotron radiation in the 90–330 eV photon energy range in order to determine the dipole and nondipole parameters. The experiment was carried out at the beamline I411 on the third generation MAX-II storage ring in Max-Lab, Lund, Sweden. The emitted electrons were analyzed with ESA-22 electronspectrometer [2]. The photoelectrons were simultaneously detected at 20 different angles in the 15°–345° angular region relative to the polarization vector in the polarization plane.

Strong interference was observed between the direct and indirect channels in the $3p$ shell photoionization of argon. Figure 1 compares the present experimental β parameters with the results of the R-matrix calculation of Gorczyca and Robicheaux [1] in the 246–253 eV photon energy range. The present experimental dipole angular distribution parameters agree with theoretical values. The difference between the dipole parameters β of Ar $3p_{1/2}$ and $3p_{3/2}$ subshells indicating the importance of the spin-orbit interaction in the photoionization.

This is the first experimental data for dipole and nondipole parameters to verify the interference between the direct and indirect photoionization.

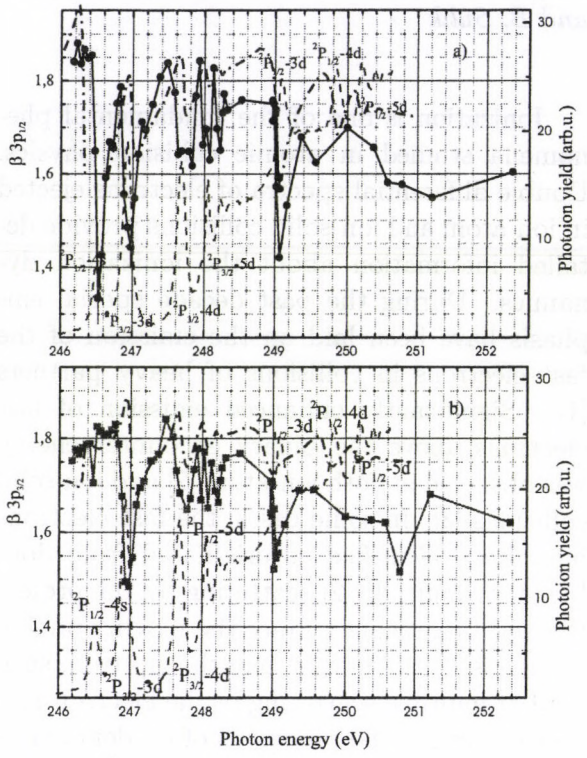

Figure 1. Experimental dipole β parameter of Ar $3p_{1/2}$ (a) and $3p_{3/2}$ (b) photoelectron lines in comparison with the theoretical values. Black full circles with black solid line show the experimental data, whereas black dashed dotted line represents the R-matrix calculation and black dashed line corresponds to the photoion yield [3] in both figures.

Acknowledgements

This work was supported by the Research Council for Natural Sciences and Technology of the Academy of Finland and by the Hungarian Scientific Research Foundation (OTKA Grant No: T037203) and by the European Community's ARI-Program.

a) Univ. of Oulu, Dept. of Physical Sciences, P.O. Box 3000, 90014, Oulu, Finland

[1] T.W. Gorczyca and F. Robicheaux, Phys. Rev. A **60** (1999) 1216.

[2] S. Ricz, Á. Kövér, M. Jurvansuu, D. Varga, J. Molnár, and S. Aksela, Phys. Rev. A **65** (2002) 042707 .

[3] O.-P. Sairanen, A. Kivimäki, E. Nõmmiste, H. Aksela, and S. Aksela, Phys. Rev. A **54** (1996) 2834.

3.8 Ionization of helium in positron impact

K. Tőkési, I.F. Barna[a)], *and J. Burgdörfer*[a)]

We present total (Fig.1) and partial (Fig.2) single-ionization cross sections of helium for positron impact within the framework of classical trajectory Monte Carlo (CTMC) method and compare with Coulomb distorted-wave models and experimental data. The incident positron energy was varied between the ionization threshold and 500 eV.

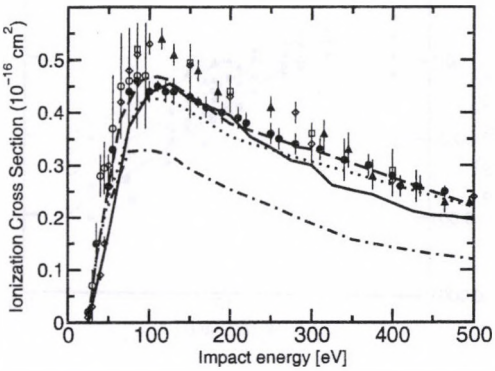

Figure 1. Ionization cross sections of helium by positron impact. Experimental data; diamond: [1], triangle: [2], solid circle: [3], circle: [4], square: [5]. Theory; solid line: present 3B-CTMC data, dash-dotted line: present 4B-CTMC data, dashed line: present distorted-wave results, dotted line: [6].

Figure 2 shows the partial single-ionization cross sections. As we expected the dominant contribution to the ionization cross section arise from the channel when the bound target electron remains in the ground state after the collision. For the case of the ionization with simultaneous excitation the cross sections are about two order of magnitude smaller. Due to the favorable dipole transition, ionization with excitation into the 2p state is larger than that into the 2s state. We hope that our calculations together with the work of Moores stimulate experimentalists to measure the partial ionization cross sections for positron impact.

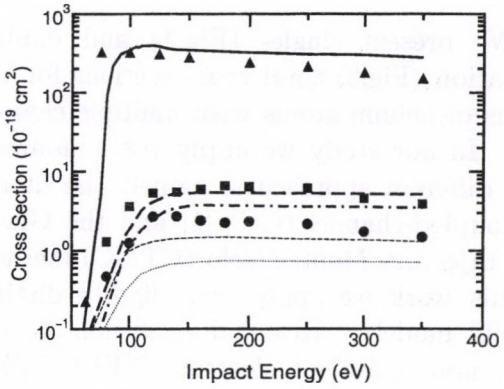

Figure 2. Partial single-ionization cross sections of helium for positron impact. The full symbols represents the results of our 4B-CTMC calculations, triangle:for $He^+(1s)$, square for $He^+(2p)$ and circle for $He^+(2s)$. The thick lines represent our distorted-wave results. The solid line is for $He^+(1s)$, dashed line for $He^+(2p)$ and the dash-dot-dashed line is for $He^+(2s)$. The thin line shows the results of Moores [7], dotted line for $He^+(2s)$, dashed line for $He^+(2p)$.

Acknowledgements

The work was supported by the Hungarian Scientific Research Found: OTKA Nos. T046095, T046454, the grant "Bolyai" from the Hungarian Academy of Sciences, TéT Grant No. A-15/04, and EU under contract no. HPRI-CT-2001-50036.

a) Institute for Theoretical Physics, Vienna University of Technology, A-1040, Vienna, Austria

[1] H. Knudsen *et al.*, *J. Phys. B: At. Mol. Opt. Phys.* **23** 3955 (1990).

[2] J. Moxom *et al.*, *Can. J. Phys.* **74** 367 (1996)

[3] D. Frommeet *al.*, *Phys. Rev. Lett.* **57** 3031 (1986)

[4] S. Mori and O. Sueoka, *J. Phys B: At. Mol. Opt. Phys.* **27** 4349 (1994)

[5] M.F. Jacobsen *et al.*, *J. Phys. B: At. Mol. Opt. Phys.* **28** 4691 (1995)

[6] C.P. Campbell *et al.*, *Nucl. Instrum. Methods. B* **143** 41 (1998)

[7] L.D. Moores, *Nucl. Instrum. Methods. B* **179** 316 (2001)

3.9 Single- and double-ionization of helium in heavy ion impact

I.F. Barna[a)], *K. Tőkési, and J. Burgdörfer*[a)]

We present single- (Fig.1) and double-ionization (Fig.2) total cross sections for collisions of helium atoms with multiple charged ions. In our study we apply two fundamentally different approaches, namely the *ab initio* coupled-channel (CC) [1] and the Classical Trajectory Monte Carlo (CTMC) method. In this work we apply two slightly distinct CTMC models. To avoid confusion we call them non-equivalent electron (NEE) CTMC [2] and equivalent electron (EE) CTMC model [3], respectively. While for the case of the non-equivalent electron model the bare Coulomb interactions among the particles are used, for the case of the equivalent electron approximation model potentials are considered.

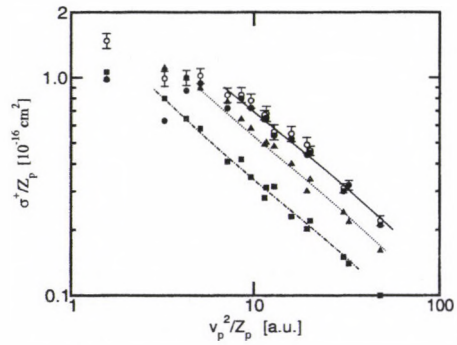

Figure 1. Scaled single-ionization cross sections. Open circles: experimental results [4],full circles: CC, full triangles: EE-CTMC, full squares: NEE-CTMC. The curve through the data is drawn to guide the eyes.

The comparison between the quantum and classical approaches is motivated through the investigation of the quantum effects in atomic collisions. The difference between the *ab initio* and the purely classical results shows us all the non-classical or quantum mechanical information which are hidden in the classical theories. We consider bare projectiles with charge states between 2 and 8 with energies between 0.19 and 2.31 MeV/amu. We find that our coupled-channel calculations are very close to the experimental data even for the cases when the external fields are strong. At the same time both CTMC models show somewhat larger discrepancies compared to the experimental cross sections.

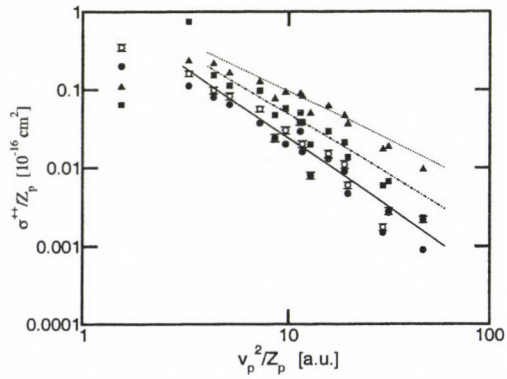

Figure 2. Scaled double-ionization cross sections. Notations are the same as in Fig. 1.

Acknowledgements

The work was supported by the Hungarian Scientific Research Found: OTKA Nos. T046095, T046454, the grant "Bolyai" from the Hungarian Academy of Sciences, TéT Grant No. A-15/04, and EU under contract no. HPRI-CT-2001-50036.

a) Institute for Theoretical Physics, Vienna University of Technology, A-1040, Vienna, Austria

[1] Barna I F, Grün N and Scheid W 2003 *Eur. Phys. J. D* **25** 239.

[2] Tőkési K and Hock G 1996 *J. Phys. B: At. Mol. Opt. Phys* **29** L119.

[3] Tőkési K and Kövér Á 2000 *J. Phys. B: At. Mol. Opt. Phys.* **33** 3067

[4] H. Knudsen *et al.*, *J. Phys. B: At. Mol. Opt. Phys.* **17** (1984) 3545

3.10 Double electron excitation of helium by charged particle impact

K. Tőkési

A four-body classical trajectory Monte Carlo method is applied in the study of double electron excitation of helium by charged particle impact. The calculations are based on the independent particle model. As projectiles we consider protons and antiprotons with energies between 0.25 and 5 MeV. The state selective total cross sections as a function of the impact energy are calculated and compared with experimental and theoretical data.

Fig. 1. shows the double excitation cross sections of helium to the $(2s^2)^1S$ (Fig. 1a), $(2s2p)^1P$ (Fig. 1b) and $(2p^2)^1D$ (Fig. 1c) states as a function of the impact energy. The errors of our calculated data are smaller or comparable with the size of the symbols. Our recent cross sections are compared with the experimental data of Giese *et al.* [3] and Moretto-Capelle *et al.* [2] and with the previous calculations of Bodea *et al.* [1]. Instead of the antiproton impact, the experiments in ref. [3] were carried out with electron impact. These cross sections are shown at the energy where the electron velocity is equal that of the antiproton velocity. In all cases the cross sections for antiprotons exceeds the cross section for protons. The largest difference is obtained for the excitation of the $(2s^2)^1S$ state (Fig. 1a). According to our expectation, with increasing projectile energies the cross sections for proton and antiproton impact approaching each other. This tendency is valid for the previous calculations of Bodea *et al.* [1] except for the $(2p^2)^1D$ (Fig. 1c). The calculated cross sections generally agree with the experimental values.

Acknowledgements

The work was supported by the Hungarian Scientific Research Found: OTKA Nos. T046095, T046454, and the grant "Bolyai" from the Hungarian Academy of Sciences.

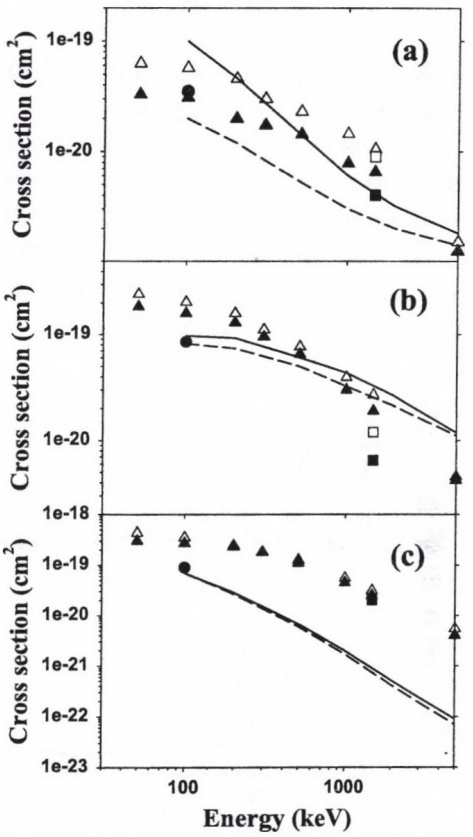

Figure 1. Cross sections for the double excitation of the helium to the $(2s^2)^1S$ (a), $(2s2p)^1P$ (b), and $(2p^2)^1D$ (c) states as a function of the projectile energy. open triangle: present CTMC results for antiproton impact, triangle: present CTMC results for proton impact, solid line: theoretical results of Bodea *et al.* [1] for antiproton impact, dashed line: theoretical results of Bodea *et al.* [1] for proton impact, circle: experimental data of Moretto-Capelle *et al.* [2] for proton impact, open square: experimental data of Giese *et al.* [3] for equivelocity electron impact, square: experimental data of Giese *et al.* [3] for proton impact.

[1] D. Bodea *et al.* J. Phys. B **31** (1998) L745.

[2] P. Moretto-Capelle *et al.* *Phys. Rev. Lett.* **79** (1997) 5230.

[3] J.P. Giese *et al.* *Phys. Rev. A* **42** (1990) 1231.

3.11 Double 1s shell ionization of Si induced in collisions with protons and heavy ions

M. Kavčič[a], M. Kobal[a], J.-Cl. Dousse[b], and K. Tőkési

The K X-ray spectra of Si induced in collisions with heavy ions and protons were measured by means of high-resolution X-ray spectroscopy, using curved crystal spectrometers [1]. The main objective of the study was to determine the double to single 1s ionization cross section ratios of Si in collision with 2 MeV protons, 34 MeV C^{2+} and 50 MeV Ne^{3+}.

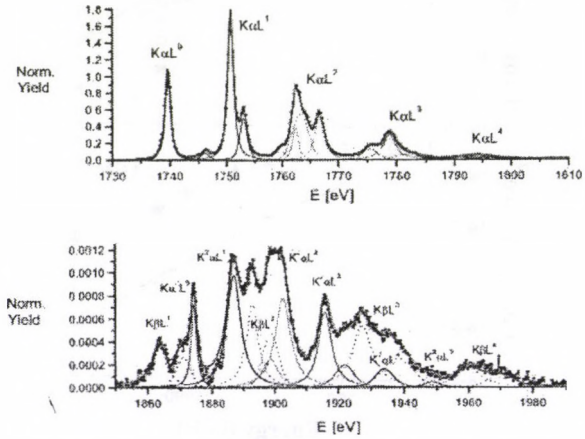

Figure 1. Measured Kα (a) and Kβ (b) X-ray spectra of Si produced by 34 MeV C ions impact. The spectra were fitted with pseudo Voigt curves. K$\alpha(1s \rightarrow 2p)$ contributions are shown by solid lines, and K$\beta(1s \rightarrow 3p)$ contributions by dotted lines.

Thanks to the sub eV energy resolution of the employed spectrometers, we were able to extract properly the yields of the Kα hypersatellite which overlaps the KβL satellite line. From the experimentally determined initial hypersatellite production yields the double (σ_{KK}) to single (σ_K) K shell ionization cross section ratios (σ_{KK}/σ_K) were determined for the three collision systems. Relatively high cross section ratios were obtained for the collisions with C and Ne ions. The cross section ratio was approximately 100 times smaller for the 2 MeV proton collision . Fig. 1 shows the measured Kα and Kβ X-ray spectra of Si produced by 34 MeV C ions impact.

The experimentally determined values were compared to theoretical predictions based on the independent electron approximation using single electron probabilities calculated within the framework of three-body classical trajectory Monte Carlo (CTMC) method and within the framework of the first order semiclassical approximation (SCA). Whereas for asymmetric collisions with protons the 1s ionization is governed by the direct Coulomb ionization, the electron capture becomes significant for more symmetric collisions involving heavy ions. It was shown that for the asymmetric proton-silicon collision the measured ratio of the double to single 1s ionization cross sections is somewhat overestimated by the SCA model whereas for heavy ion collisions CTMC calculations incorporating both ionization mechanisms give values that are in relatively good agreement with the experimental results.

Acknowledgements

This work was supported by the Slovenian Ministry of Education, Science and Sport of Slovenia through the research program *Low Energy Physics* (PO-0521-0106-02), by the Swiss National Science Foundation and through a bilateral Scientific and Technological Cooperation between Slovenia and Hungary, TéT Grant No. SLO-15/03.

a) J. Stefan Institute, P.O. Box 3000, SI-1001 Ljubljana, Slovenia

b) Physics Department, University of Fribourg, CH-1700 Fribourg, Switzerland

[1] M. Kavčič, M. Kobal, J.-Cl. Dousse,and K. Tőkési, Nucl. Inst. and Meth. B, accepted.

3.12 Fermi-shuttle type multiple electron scattering in atomic collisions

K. Tőkési, B. Sulik, and N. Stolterfoht[a)]

In ion-atom collisions, higher orders of multiple electron scattering can be treated practically only in non-perturbative models. Especially classical trajectory Monte Carlo (CTMC) calculations seem to work successfully in many Fermi-shuttle acceleration cases [1,3]. A main advantage of the CTMC method is that many details of the classical collision scenario can be conveniently analyzed in its framework. The analysis of the CTMC trajectories, e.g., makes it possible to classify and identify multiple electron scattering events. In spite of the limitations due to its classical character, CTMC cross sections agree well with experiments for most of the studied collision sytems [1,3]

In our present works [4,5], we perform CTMC calculations to follow the ionisation process in ion-atom collisions for a set of projectile-target combination. The incident projectile energy is varied from small to intermediate energies (1-50 keV/u). In our present approach, we solve Newton's classical nonrelativistic equations of motions for a complete three-body system. The three particles are the projectile, one atomic active electron (e), and the remaining target ion. The interaction between either pairs of the partners is represented by a central model potential, which accounts for the screening of the inactive electrons of the ionic cores. The parameters of the model potentials has been derived from Hartree-Fock calculations.

Fig.1 shows a sample CTMC event for a projectile-target-projectile-target (P-T-P-T) scattering at intermediate velocity (150 keV/u) C^+ + Xe collisions. The projectile and electron trajectories clearly show two consecutive close P-collisions between the active target electron and the incoming projectile ion. In slower collisions, one may expect higher order collision sequences. Indeed, the analysis of many CTMC events at small projectile energies (1 keV/u) indicates the dominance of long (6-14-fold) Fermi-shuttle type scattering sequences in electron emission above 10 eV kinetic energy. The energy gain of the ejected electrons can be considered as a result of ping-pong games, played by the two colliding ionic cores with the electron as a ball.

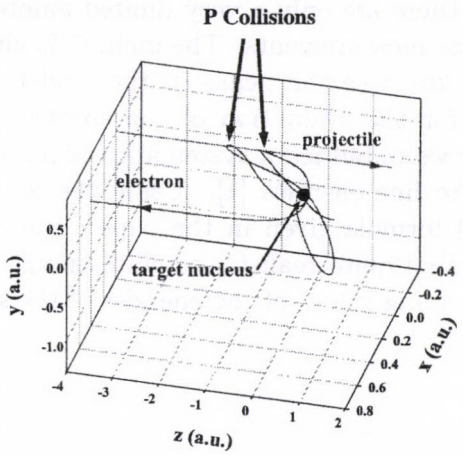

Figure 1. A sample CTMC event for a P-T-P-T scattering in intermediate velocity (150 keV/u) C^+ + Xe collisions. The projectile and electron trajectories clearly show two consecutive close P-collisions between the active target electron and the incoming projectile ion.

Acknowledgements

This work was supported by Hungarian OTKA Grants (T046905, M27839), the grant "Bolyai" from the Hungarian Academy of Sciences, and the TéT Grant No. GR-11/03.

a) Hahn-Meitner-Institut Berlin, Bereich Strukturforschung Glienickerstr. 100, D-14109 Berlin, Germany

[1] B. Sulik *et al.*, Phys. Rev. Lett. **88** (2002) 073201.

[2] B. Sulik *et al.*, Phys. Scr. T92 (2001) 463.

[3] B. Sulik *et al.*, Nucl. Inst. and Meth. B 212 (2003) 32.

[4] T. Ricsóka *et al.*, Nucl. Inst. and Meth. B, accepted.

[5] K. Tőkési *et al.*, Nucl. Inst. and Meth. B, accepted.

3.13 A procedure to derive more reliable KαL^i satellite energy and intensity values

I. Török, T. Papp

In a certain Z range, where already the KL^i satellite groups of the Kα lines are distinctly seen for the Kα_1 and Kα_2 lines, many times the satellites of the Kα_2 line are superimposed on the Kα_1 line and its satellites. In such cases it is difficult to evaluate the mixed lines. Probably therefore in this Z range in the open literature there are only a very limited number of satellite measurements. The main difficulty is: where to place the peaks in the model spectrum for the evaluation of the spectra. Recently we published a systematics of the KαL^i satellite line energies [1]. Using the semiempirical formula given in the paper, one could determine quite realistic satellite energies for the starting values of the energies of the satellite peaks.

Another help can be for getting better peak parameters is to make a systematics of the relative intensities of the satellite lines, and to correct the values got from the evaluating program. So by using the combined systematics of the satellite energies and that of the intensities one can determine more realistic peak parameters for these satellites, after several iteration.

A similar procedure is possible for the KβL^i satellite lines, but here one has to take into account the much more effective band structure of these lines.

[1] I. Török, T. Papp, S. Raman, Nucl. Instrum. Meth. B150 (1999) 8.

3.14 Assessment of M X-ray line energies of ^{237}Np emitted by ^{241}Am

G. Kalinka, M. Novák

In the course of a systematic investigation [1] to accurately characterize the photon spectrum of ^{241}Am in the 2-130 keV energy range in order to use it for simultaneous energy, resolution and efficiency calibration of X-ray detectors, we have observed significant deviation of the energy values of certain Np L and practically all M X-ray lines relative to literature data [2,3] on elemental ^{237}Np.

Our experimental data was taken with two liquid nitrogen cooled Si(Li) detectors and one Peltier cooled Si SDD detector having energy resolutions between 145-160 eV, energy linearity within ± 2 eV and each having been carefully characterized for their response in the energy range of interest beforehand. The ^{241}Am source used was a commercial thin α-type source, supposedly in the form of $^{241}AmO_2$, deposited on a stainless steel backing. This had the advantage of simultaneously acquiring accompanying fluorescent X-ray lines from Cr, Fe and Ni which could serve as built in energy references, but unfortunately Cr K lines masked the highest energy Np M-O transitions.

While Np L X-ray lines from ^{241}Am are somewhat better studied, data on M X-rays are rather scarce [4]. Therefore spectra were first fitted using transitions identified during a high resolution crystal spectrometer measurement of EPMA excited M-lines from $^{237}NpO_2$ [2]. Such fits using Lorentzian widths from [5,6] resulted in energies and Gaussian widths well in excess to [2,3], and our prior calibration values, respectively. In the next approach, therefore, experimental Gaussian width values were used, and for the three most intense transitions allowance was made for the presence of high energy satellite lines with parameters - for the sake of simplicity - identical to those of diagram lines. Results similar to the one in the figure, taken with a Si(Li) detector, were consistently obtained with other detectors too.

Satellites (distinguished by shading in the figure) have intensities ~1/3 of corresponding diagram lines and are shifted ~70 eV upwards, whereas diagram line energies are still ~9 eV up relative to [2], compared with ~24 eV before, without satellites. Note that contrary to intershell transitions, the L_1L_3 intrashell transition of Np showed neither energy shift, nor extra Gaussian widening larger then ~ ±2 eV each, therefore no need was for the inclusion of satellites, similar to neighbour Cr, Fe, and Ni K lines mentioned above.

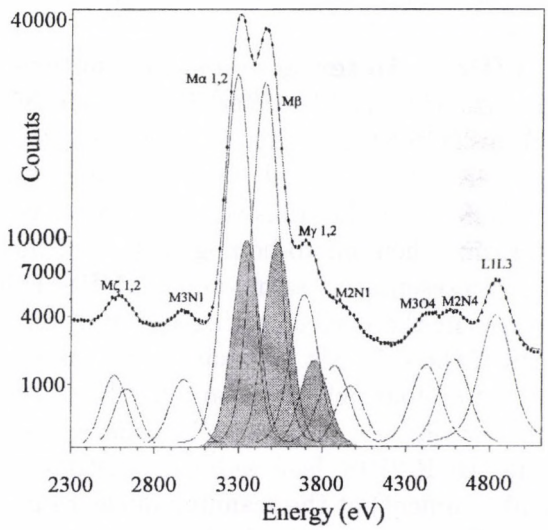

Although the resolving power of the detectors used, combined with the statistics acquired has made it possible to unambiguously identify the presence of high energy satellites of the main Np M lines during the α-decay of ^{241}Am, more favourable experimental condition and theoretical explanation are necessary to get details of the physics behind.

[1] M. Novák, Diploma Thesis, Debrecen University, 2004

[2] H. Kleykamp, Z. Naturforsch. 36A (1981) 1388

[3] R. Delattes, *et al.*, Rev. Mod. Phys. 75 (2003) 35

[4] D.D. Cohen, Nucl. Instrum. and Methods A 267 (1988) 492

[5] M.O. Krause, *et al.*, Phys.Rev. A 15 (1977) 2335

[6] J.L. Campbell, T. Papp, At. Data Nucl. Data Tables 77 (2001) 1

4.1 Contribution of the IBA group to the EU5 MICRO-XRF project

Á.Z. Kiss[h)], I. Uzonyi[h)], A. Simon[h)], Z. Szikszai[h)], G.Á. Szíki[h)], Gy. Szabó[h)], I. Gomez-Morilla[g)], B. Vekemans[a)], L. Vincze[a)], G.W. Grime[g)], R. Simon[c)], J.-N. Audinot[e)], U. Wätjen[d)], A. Somogyi[b)] and F. Adams[a)]

The overall objective of the EU5 project was the development of synchrotron radiation induced micro X-ray fluorescence analysis (MICRO-XRF) as an accurate and traceable elemental analysis on the microscopic level. The Ion Beam Analytical group of ATOMKI took part in this project for two years and contributed to four work packages from the seven. The most important results are summarised below.

WP3: Heterogeneity characterisation of existing Certified Reference Materials (CRMs). This part of the project dealt with experimental testing of four candidate Reference Materials with the objective to determine their micro-homogeneity and minimum representative sample mass (MRSM) for the use in the corresponding certification reports of these CRMs. Measurements were carried out on four pelletized samples (BCR-176R incineration ash; BCR-277R estuarine sediment; BCR-280R lake sediment; BCR-320R canal sediment) at the scanning nuclear microprobe laboratory of ATOMKI. Besides determining MRSM-s, our measurements enlightened the conceptual differences of the existing definitions for the minimum representative sample mass and urged the development of new models.

WP4: Feasibility study of reference materials. The goal of this work package was to select, produce and characterize standards in order to determine the sensitivity and the lateral resolution of the micro-XRF technique. Within the framework of this work package, depth profile and implanted dose of fluorine in implanted silicon samples were measured using the Proton Induced Gamma-ray Emission (PIGE) method. Our results show that PIGE can compete with Secondary Ion Mass Spectrometry (SIMS) in fluorine depth profiling. Furthermore, it is a non-destructive technique.

WP5: Intercomparison study of selected materials. In WP5 the acceptability of MICRO-XRF as a potential primary tool for microscopic trace elemental analysis was investigated. The ATOMKI IBA group applied Particle Induced X-ray Emission (PIXE) and Rutherford Back-scattering Spectrometry (RBS) techniques as independent methods in this interlaboratory study. Activities focused on determining the concentrations of ZnO deposited in the form of thin (1-10 nm) films on various substrates.

WP6: Development of micro-PIXE as a quantitative method. The ATOMKI-IBA Group and the University of Surrey took part in this work package, where an intercomparison study of quantitative PIXE analysis with high lateral resolution was implemented. Our aim was to investigate the traceability, accuracy and reproducibility of protocols and reference materials for quantitative elemental microanalysis using probe beam techniques with a micrometer spatial resolution. The results of the intercomparison measurement with BCR glass demonstrated that, at least under controlled conditions, the reproducibility and accuracy of standardless PIXE analysis could be within 5%. We can conclude that this technique is a valuable tool for MICRO-XRF calibration.

Co-operating institutions:

a) University of Antwerp, Department of Chemistry, MiTAC, Antwerp-Wilrijk, Belgium;
a) European Synchrotron Radiation Facililty (ESRF), Grenoble, France;
c) Forschungszentrum Karlsruhe (FZK), Group ISS, Karlsruhe, Germany;
d) EC-JRC, Institute for Reference Materials and Measurements (IRMM), Geel, Belgium;
e) Laboratoire d'Analyse des Matériaux (LAM) CRP-GL, Luxemburg;
f) University of Southern Denmark, Odense M., Denmark;
g) University of Surrey, Dept. of Physics, Surrey, U.K.;
h) ATOMKI, Debrecen, Hungary;
i) KFKI Atomic Energy Research Institute, Health and Environ. Physics, Budapest, Hungary.

4.2 Characterisation of rough surfaces of gold nanoparticle films with RBS microbeam

A. Simon, Z. Kántor[a)], *P. Heszler*[b,c)], *A. Csik, J. Ederth*[b)], *A. Hoel*[b)], *J. Kopniczky*[b)], *C.-G. Granqvist*[b)]

Au nanoparticles exhibit excellent compatibility with biomolecules and some distinct optical properties. Their two popular features, the colour change upon aggregation and surface plasmon resonance (SPR) enhancement, have been exploited in analytical chemistry and catalysis, biosensing platforms, and immunoassays. The preparation of monodisperse Au nanoparticles with improved electronic, optical, and chemical properties is still an ongoing and formidable task as there are disadvantages of the thin film deposition techniques, such as: particulate deposition together with the thin film and uneven surface roughness even at the particulate-free areas of the thin film.

Our aim was to deduce the microstructural details of a thin Au nanoparticle films by microbeam assisted Rutherford Backscattering Spectrometry. For this purpose, a new numerical method has been developed for the deterministic calculation of the RBS spectra of solid surfaces with arbitrary 3D-structure, elemental and isotopic distribution. An arbitrary cross section of a sample can be introduced into the RBS simulation software, which comprises an ideal tool for the calculation of how the geometrical facts like surface roughness and granular nanostructure affect the RBS spectra. As a complementary technique, Atomic Force Microscopy (AFM) and Scanning Electron Microscopy (SEM) were also taken for studying the morphology of the nanocrystalline films. However, none of these two methods are sensitive for the elemental composition.

Films of ultra-fine gold particles were prepared onto Si substrate by advanced gas evaporation and deposition technique. This method is designed for creating isolated nanocrystals and nanocrystal films with well-defined particle size distribution. These nanoparticles are of high purity, exhibiting very good crystallinity and a well-controlled and reproducible mean size. Different preparation conditions such as evaporation temperature and deposition time were applied resulting different film thickness and mean size of the Au nanoparticles.

Model structures of a dense gold thin film with surface roughness and homogeneously distributed contaminant and a nanoparticle thin film, with and without contaminants in the intergranular volume have been used for the simulation of the RBS spectra, by varying the roughness, lateral scale and particle size parameters, as well as the elemental compositions and contaminant densities. For the simulation of the measured samples the gold layer was considered to be 50 nm thick in average, the nanoparticle size was 10 nm with 100 nm surface undulations and 4nm RMS of the height profile of the film.

We found that our simulation code could approximate the measured RBS spectra better than the traditional RBS evaluation codes. Our result also showed that the RBS spectra of the studied gold nanolayers could be reliably interpreted with the presence of a certain amount of water (or may be another material consisting of light elements) in the intergranular pores, in line with other experimental observations.

a) Department of Physics, University of Veszprém, P.O. Box 158, H-8201 Veszprém, Hungary

b) Department of Engineering Sciences, The Ångström Laboratory, Uppsala University, P.O. Box 534, SE-75121 Uppsala, Sweden

c) Research Group of Laser Physics of the Hungarian Academy of Sciences, Box 406, H-6701 Szeged, Hungary

4.3 Diatoms and the nanotechnology

K. Tőkési, R.J. Bereczky, Gy. Lakatos[a] *and C. Cserháti*[b]

During the last decade studies of interactions between highly charged ions (HCI) and solid surfaces are at the center of interest which is partly stimulated by potential future technical application such as nanofabrication. The investigation of the interactions of highly charged ions with internal surfaces recently become available due to the advances in the fabrication of micro- and nanocapillaries. These target materials offer the opportunity to observe "hollow atom" formation in free space. Hollow atoms are an exotic form of matter where the atomic charge cloud resides in shells with large diameters while the core is virtually empty. In the past there has been an increasing amount of indirect evidence for the existence of this atomic state. Microcapillary transmission promises to provide direct evidence for the hollow atom formation for the first time. Our earlier theoretical descriptions rely on metallic microcapillaries which have proven to be quite successful in comparison with experimental data [1]. However, since very detailed measurements have recently become available for insulator nanocapillaries, critical and precise tests of theory are only now being possible [2]. We note, that the theoretical description of the interaction between the HCI and insulator nanocapillaries is far from being well understood. One of the key point of the experimental investigations is the preparation of the nanocapillaries. In this work we propose an alternative way to prepare insulator nanocapillaries. We take an advantage of the nature that during the evolution the cylindrical shape nanostructure was developed as a truss of diatoms [3]. The truss of the diatoms contains roughly 99 % SiO_2 and in some cases of diatoms it form almost ideal cylindrical shape. As an example Fig. 1 shows the scanning electron micrograph of the diatom. The size of the holes in the truss are in the nanometer range (see Fig. 1a). On the basis of these properties the diatoms can be ideal candidate for insulator nanocapillaries in our forthcoming experiments.

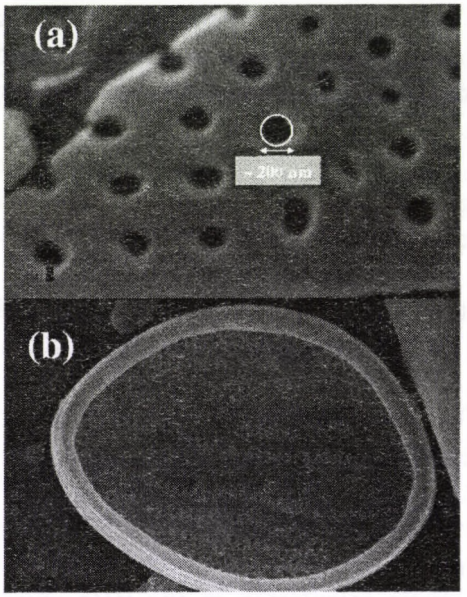

Figure 1. Scanning electron micrograph of the diatom.

Acknowledgements

The work was supported by the grant "Bolyai" from the Hungarian Academy of Science, and TéT Grant No. A-15/04.

a) Ecological Institute, Univ. of Debrecen

b) Dept. of Solid State Physics, Univ. of Debrecen

[1] K. Tőkési, L. Wirtz, C. Lemell, and J. Burgdörfer, Phys. Rev. A **64** (2001) 042902.

[2] N. Stolterfoht, *et al.*, Phys. Rev. Lett. **88** (2002) 133201.

[3] Gy. Lakatos, *et al.*, Proceedings of the 10th International Svedala Symposium on Ecological Design, Sept. 11-13 (1992), p155.

4.4 Direct observation of the hydrogen peak in the energy distribution of electrons backscattered elastically from polyethylene

D. Varga, K. Tőkési, Z. Berényi J. Tóth, and L. Kövér

Observation of the hydrogen peak is either challenging or impossible task for the conventional electron spectrosopy. Hydrogen was observed earlier in electron scattering experiments using transmission geometry and formvar film [1]. In this work we show an alternative way for the detection of hydrogen peak analyzing the spectra of elastically backscattered electrons from polyethylene ($(CH_2)_n$). We take advantage of the fact that the elastic peak from polyethylene split into carbon and hydrogen components. The energy of the elastically scattered electrons is shifted from the nominal values due to the energy transfer between the primary electron and the target atoms (recoil effect). Due to the motion of the scattering atoms, a broadering of the energy width of the spectra takes place.

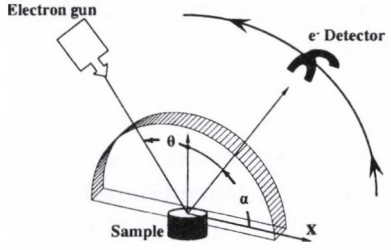

Figure 1. Schematic view of the geometric configuration of the calculation.

We performed Monte Carlo simulation for 2 keV electrons penetrated and elastically backscattered from polyethylene sample. In our calculations both the elastic and inelastic scattering events were taken into account. We further assume that the thermal motion of the target atoms follows the Maxwell-Boltzmann energy distribution. After each elastic scattering the recoil energy was calculated according to ref [2]. Fig. 1 shows the geometric configuration used in the calculation. The initial angle of incident beam (θ) was 50^o.

Fig. 2 shows the gray scale plot of the intensity of electrons backscattered elastically from polyethylene. The separation between the carbon and hydrogen peaks is clearly seen. Our results show that the multiple electron scattering causes only minor changes in the energy shifts and broadenings of elastic peaks. Moreover, our simulations are in good agreement with our experimental observations [3].

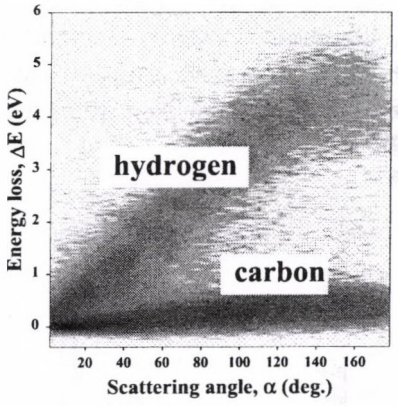

Figure 2. Gray scale plot (white: minimum intensity, black: maximum intensity) of the electron intensity backscattered elastically from polyethylene.

Acknowledgements

The work was supported by the Hungarian Scientific Research Found: OTKA No. T0038016, and the grant "Bolyai" from the Hungarian Academy of Sciences.

[1] M. Vos, Phys. Rev. A **65** 012703 (2001)

[2] D. Varga, *et al.*, Surf. Interface Anal. **31** 1019 (2001).

[3] D. Varga, *et al.*, Book of abstracts, ESS'04, IUVSTA workshop July 4-8, 2004 Debrecen, Hungary, p17.

4.5 Effective energy loss function of silver derived from reflected electron energy loss spectra

Z. Zhang[a)], Z. Ding[a)], H. Li[a)], K. Tőkési, D. Varga, and J. Tóth

The inelastic excitations of silver are studied both experimentally and theoretically. The effective energy loss function of silver was derived from reflected electron energy loss spectra (REELS). The full width at half maximum of the elastic peak was in the 0.4-0.6 eV region using the ESA-31 home built spectrometer based on a 180° hemispherical analyser [1] with 0.5 % energy resolution but with different retardation. The electron beam was produced by LEG 62 VG Microtech electron gun with tungsten filament. Prior to electron spectroscopic analysis, in-situ cleaning of the sample surface was performed using 2 keV energy Ar^+ ion sputtering.

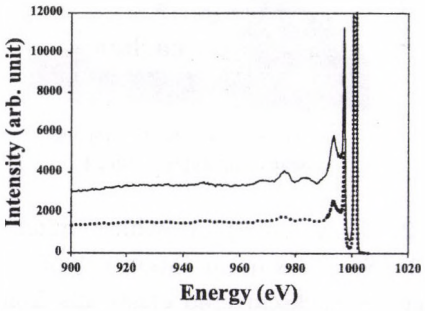

Figure 1. Reflected electron energy loss spectra of 1 keV energy primary electrons. solid line: incidence angle of the primary electron beam is 0° and the observation angle is 50°, dotted line: incidence angle of the primary electron beam is 50° and the observation angle is 0°.

The incidence angle of the primary electron beam were 0° and 50° while the angle of analysed beam were measured at 50° and 0° with respect to the surface normal of the sample, respectively. During measurements the vacuum was better than $2x10^{-9}$ mbar. Fig 1. shows the typical measured electron spectra.

The effective energy loss functions (EELF) have been derived from these experiments in Hefei, China. Inelastic scattering cross sections obtained by the Tougaard's deconvolution method [2] is similar to the extended Landau approach, but the latter is more sophisticated. Therefore in our numerical simulation the extended Landau approach was used. The effective energy loss functions (EELF) have been derived from differential inverse inelastic mean free path as described in ref [3].

It has been revealed that the EELF is very close to the theoretical surface energy loss function in the lower energy loss region but gradually approaches the theoretical bulk energy loss function in the higher energy loss region for Ag. The simulated REELS spectra by Monte Carlo method based on the EELFs reproduced the experimental REELS spectra with considerable success.

Acknowledgements

This work was partially supported by the National Natural Science Foundation of China (Grant No.10025420 and 90206009). The work was also supported by the Hungarian Scientific Research Found: OTKA No. T038016, the grant "Bolyai" from the Hungarian Academy of Sciences, and TéT Grant No. CHN-28/2003.

a) Structure Research Laboratory and Department of Physics, University of Science and Technology of China, 96 Jinzhai Road, Hefei, Anhui 230026, P.R. China

[1] L. Kövér, D. Varga, I. Cserny, J. Tóth, and K. Tőkési, Surf. Interface Anal. **19**, (1992) 9.

[2] S. Tougaard, J. Kraaer, Phys. Rev. B**43**, 1651 (1991).

[3] Z. Zhang, T. Koshikawa, T. Iyasu, R. Shimizu, and K. Goto Surf. Interface Anal. **35**, 403 (2003).

4.6 Angular distribution of electrons backscattered elastically from silver

K. Tőkési and D. Varga

The effect of the multiple electron scattering to the spectra of elastically backscattered electrons are studied theoretically for polycrystalline silver sample. The simulation is based on the Monte Carlo technique where both the elastic and inelastic scattering events were taken into account. In this work the partial expansion method was used to describe differential and total cross sections for elastic scattering. Details of the elastic cross section calculations can be found in ref. [1].

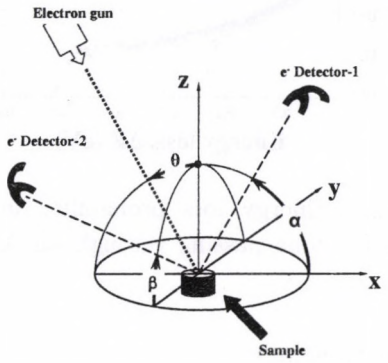

Figure 1. Schematic view of the geometric configuration of the calculation.

Fig. 1 shows the geometric configuration used in the calculation. The initial angle of incident beam (θ) was 68^o. The angular distributions of the elastically scattered electrons were calculated at the xz (α-distribution) and the yz (β-distribution) planes. The bin size in both angular direction was 4^o. The Monte Carlo simulation was performed for 1 keV electrons. Fig. 2 shows the angular distributions of electrons backscattered elastically from silver sample. Fig. 2b shows that, depending on the geometrical condition, the partial yield ($I_1(\alpha)$) of the elastically backscatted electrons to the total yield ($I_\Sigma(\alpha)$) can be very small.

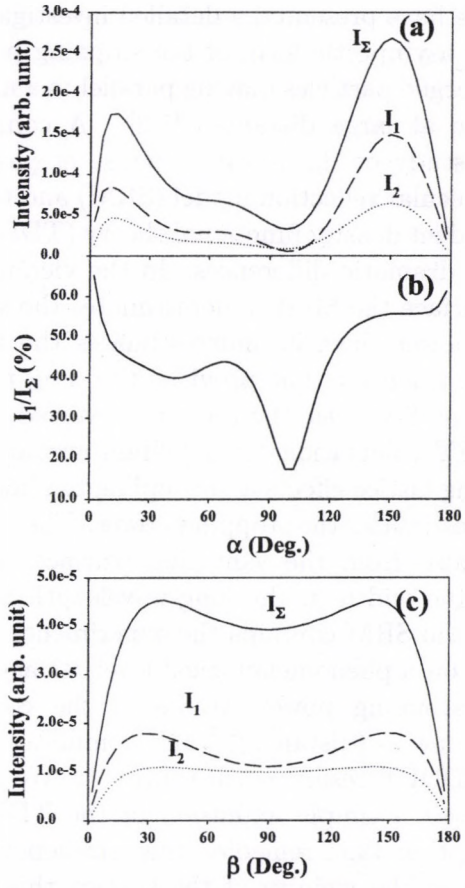

Figure 2. Angular distributions of electrons backscattered elastically from silver sample. Dashed line: the electron suffers only one elastic scattering and escape from the sample (I_1), dotted line: the electron suffers two elastic scatterings and escape from the sample (I_2), solid line: the elecron escape from the sample via elastic scatterings (I_Σ).

Acknowledgements

The work was supported by the Hungarian Scientific Research Found: OTKA No. T038016, TéT Grant No. A-15/04, and the grant "Bolyai" from the Hungarian Academy of Sciences.

[1] F. Salvat, and R. Mayol, Comput. Phys. Commun. **74** 358 (1993).

4.7 Energy loss of charged particles at large distances from metal surfaces

K. Tőkési, X-M. Tong[a)], C. Lemell[b)] and J. Burgdörfer[b)]

We have presented a detailed investigation of the asymptotic form of the stopping power for charged particles moving parallel to a metal surface at large distances [1,2]. A comparative study of the linear response employing the specular reflection model (SRM) and time-dependent density functional theory (TDDFT) shows dramatic differences. In the vicinity of the surface the SRM underestimates the stopping power since it underestimates the local electron density that provides the drag force. At large distances, the roles are reversed. The TDDFT calculation for a jellium surface neglecting lattice effects and coupling to phonons underestimates the stopping power. The latter originates from the vanishing (surface) plasmon line width in the long-wavelength limit. Since the SRM contains the experimental line width on a phenomenological level, its asymptotic stopping power results in the correct power law $\sim$ (distance)$^{-3}$ and dominates over the TDDFT result $\sim$ (distance)$^{-4}$. We have proposed a simple extension of the TDDFT description that remedies this deficiency [1]. While in the vicinity of the surface this new stopping power calculation gives values significantly larger than obtained by SRM, it converges to the SRM in the asymptotic region above the surface.

As an application of our stopping power calculations we present the energy loss for a protons passing through an Al microcapillary. The reason for this choice is that for small z differences between TDDFT and SRM are more pronounced. Note however, that integrated energy loss is much larger and more easily measurable for highly charged ions. For the study of the problem of energy loss we have performed a classical trajectory Monte Carlo simulation with an ensemble of 5×10^6 primary trajectories. In our simulations a capillary with a radius of 2360 a.u. and length L=30000 a.u. was used. Fig.1 shows the energy loss probability for a 2.1 keV/amu H^+ ions passing through an Al microcapillary. The energy loss exceeding about 0.3 eV corresponding to $\Delta E/E$=0.014 % should be experimentally observable. We note that with increasing projectile charge the maximum reachable energy loss for TDDFT approach to the value obtain with SRM.

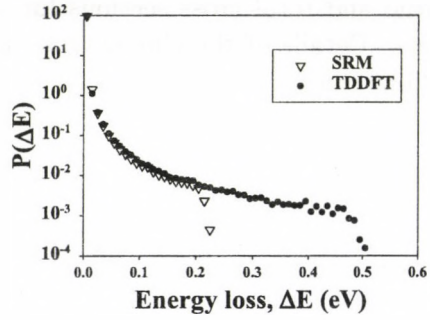

Figure 1. Energy loss probability for a 2.1 keV/amu H^+ ions passing through an Al microcapillary.

Acknowledgements

The work was supported by the Hungarian Scientific Research Found: OTKA Nos. T038016, T046095, the grant "Bolyai" from the Hungarian Academy of Sciences, TéT Grant No. A-15/04, the Austrian Fonds zur Förderung der wissenschaftlichen Forschung, FWF (Austria), and EU under contract no. HPRI-CT-2001-50036. We gratefully acknowledge invaluable inspiration and guidance over many years by our friend and pioneer of this field, Rufus Ritchie.

a) Physics Department, Kansas State University, Manhattan, Kansas 66506-2601, USA

b) Institute for Theoretical Physics, Vienna University of Technology, A-1040, Vienna, Austria

[1] K. Tőkési, X-M. Tong, C. Lemell, J. Burgdörfer, Advances in Quantum Chemistry **46** 29 (2004).

[2] K. Tőkési, X-M. Tong, C. Lemell, J. Burgdörfer, in press PRA.

4.8 Electron density profile in multilayer systems

K. Tőkési, A. Sulyok[a)], and M. Menyhárd[a)]

Electron energy loss spectroscopy (EELS) has been used extensively to study the multilayer systems, where the thickness of layers are in the nanometer range. These studies has received considerable attention because of its technological interest, for example in the nanotechnology. On the most fundamental level, its importance is derived from the basic physics that is involved.

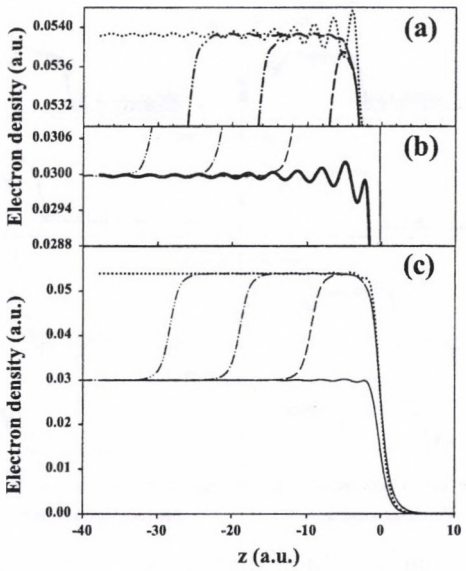

Figure 1. Electron density profile in LDA approximation. The vacuum-solid interface is at $z = 0$. Half-infinite samples; solid line: profile for r_s=1.997, dotted line: profile for r_s=1.642, dashed line: profile for 5 Å coverage of r_s=1.642 on the substrate described by r_s=1.997, dash-dotted line: profile for 10 Å coverage of r_s=1.642 on the substrate described by r_s=1.997, dash-double-dotted line: profile for 15 Å coverage of r_s=1.642 on the substrate described by r_s=1.997.

One key quantities of interest is the response of a many-body system to an external perturbation: How act and how modify the interface between the solid-solid or solid-vacuum the excitations in the solid and in the vicinity of the interfaces. In this work, as a starting point of such investigations we calculated the electron density profile for multilayer systems. Our approach employs the time-dependent density functional theory (TDDFT), that is, the solution of a time-dependent Schrödinger equation in which the potential and forces are determined selfconsistently from the dynamics governed by the Schrödinger equation. We treat the problem in TDDFT at the level of the local-density approximation (LDA). Later, the comparison of experimentally obtained loss functions and the theory, based on our TDDFT calculations can provide deeper understanding of surface physics. We performed the calculations for half-infinite samples characterized by r_s=1.642 and r_s=1.997. We also performed the calculations for double layer systems. The substrate was characterized by r_s=1.997 and the coverage by r_s=1.642. Fig. 1. shows the obtained electron density profile in LDA approximation. Because of the sharp cutoff of electronic wave vectors at the Fermi surface, the densities in the interior exhibit slowly decaying Friedel oscillations. To highlight the Friedel-oscillation we enlarged the electron density profile in Fig. 1a. and Fig. 1b.

Acknowledgements

The work was supported by the Hungarian Scientific Research Found: OTKA No. T038016, the grant "Bolyai" from the Hungarian Academy of Sciences, and TéT Grant Nos. CHN-3/2004,and A-15/04.

a) Research Institute for Technical Physics and Materials Sciences Budapest, P.O. Box 49, H-1525

[1] K. Tőkési, X-M. Tong, C. Lemell, J. Burgdörfer, Advances in Quantum Chemistry **46** 29 (2004).

[2] K. Tőkési, X-M. Tong, C. Lemell and J. Burgdörfer, in press PRA.

4.9 Investigation of charge collection in a Silicon PIN photodiode

A. Simon, G. Kalinka

Ion Beam Induced Charge (IBIC) imaging with a 2 MeV He^+ microbeam has been used to investigate spectroscopic features and charge transport properties of a Hamamatsu S1223 silicon PIN photodiode. Pulse height spectra were collected with high lateral resolution at different reverse bias values between 0 V and -100 V. Pulse height maps and median energy maps were generated to observe the spatial variations of charge collection properties. Absolute charge collection efficiency (CCE) was calculated along a line including the edge structure of the photodiode.

The central sensitive area of the pin diode was found to be very homogeneous without any incomplete charge collection regions, which is of great importance for the applications of pin diodes for radiation spectroscopy. The absolute charge collection efficiency profile calculated through a line shows a broad plateau close to 94 % CCE and an exponential decrease where the electric field is absent. However, low energy satellite peaks and other structures in the spectra were found. For the identification of their origin a narrow, 50 μm wide boundary region was selected which comprised a narrow 7.5 μm wide strip of the central region, a 18 μm wide edge protection region next to it and a 24 μm wide strip from the outermost protection ring. Spectra at different biases taken here are shown in the figure.

At zero bias there is only one peak at about 2000 keV. These counts originate from the central region, where CCE is close to 100 %. To the left of this peak two "truncated shelf" regions are seen, separated by a valley with a tiny peak sitting in it. With increasing bias these structures shift to the right (higher amplitudes), their "widths" shrink and beginning from the right (highest energy) side they steadily transform into peaks (above 10 V and 60 V for the right and left shelf regions, respectively). This behaviour can be understood by the particular edge protection structure of the device. By increasing the bias the depletion region extends not only in-depth, but laterally, too. First, it reaches a narrower and thinner protection layer region, then a wider and thicker one. A thinner coverage and the existence of a depleted region results in higher amplitude, while a thicker coverage and/or an undepleted region below it with incomplete charge collection gives lower amplitude. For further details see [1].

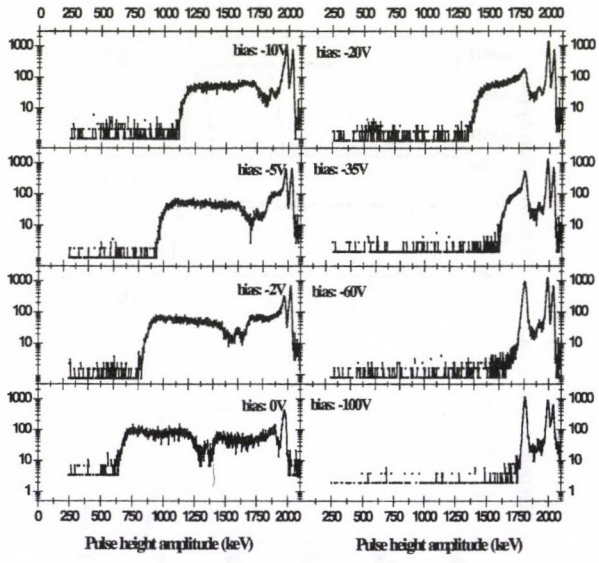

We can conclude that satellite peaks originate from volumes beneath the different layers of the photodiode at the edge and gold bonding pad due to energy loss in edge protecting surface coverages, contact metallisation and incomplete charge collection in the near surface and undepleted regions. The energy shift depends on the thickness and chemical composition of the layer structure.

In overall we have found that the CCE is good over the bulk of the device, but for spectroscopic purpose we recommend to use a collimator, which uncovers only the region where the p-doping is uniform. This way the edge effects can be effectively filtered out, thus the spectroscopic performance of the photodiode will significantly improve.

[1] A. Simon and G. Kalinka, accepted for publication in Nuclear Instruments and Methods in Physics Research B

4.10 High spatial resolution measurement of depth-of-interaction of a PET LSO crystal

A. Simon, L. Balkay[a)], G. Kalinka, A. Kerek[b)], D. Novák, A. Sipos, J. Végh, L. Trón[a)], J. Molnár

A new type of experimental technique to investigate the depth-of-interaction (DOI) dependence in small scintillator elements designed for high-resolution animal PET [1] has been introduced at our institute, recently. A lutetium oxyorthosilicate (LSO) crystal ($2\times2\times10$ mm^3) was irradiated with a highly focused 2 MeV He^+ beam at the ATOMKI nuclear microprobe laboratory. Pulse height spectra from a photomultiplier (PMT) attached to one end of the LSO crystal were collected in list mode. Sequential scans of 1000×1000 μm^2 areas along the 10 mm long crystal were made to get high lateral resolution images of pulse height spectra at different distances from the window of the PMT. A mean pulse height algorithm was applied to each pixel to generate two dimensional intensity images and the corresponding spectra of 100 μm$\times$1 mm areas.

Representative pulse height spectra are shown in Fig. 1 for different distances between the position of irradiation and the PMT. The mean value of the pulse height spectrum describing the position of the full energy peak is a way to measure DOI effects. It is seen that the closer the DOI to the PMT-end of the crystal the higher the energy of the peak. The centre of the detected peak varies about 30 % *along* the lateral side of the crystal. This effect is due to the increasing number of reflections with associated loss of light when the distance between the DOI position and the light collecting PMT grows. Further these results, no difference in the light intensity was found depending on which position *across* (perpendicular to the length of) the crystal was irradiated with the microbeam.

The obtained results of the overall DOI dependence confirm previous measurements on LSO crystals with similar geometry and wrapping but based on collimated gamma-ray irradiation. Since the present experimental setup allows obtaining data with several orders of magnitude better spatial resolution (from μm up to mm) than with collimated gamma-beam, the method can be applied for variety of problems where high spatial resolution is required. By varying the beam energy the penetration depth of the ions can be changed giving the opportunity for the real 3D light collection mapping. A further advantage of using an ion beam is the absence of Compton-scattering contribution to the spectrum.

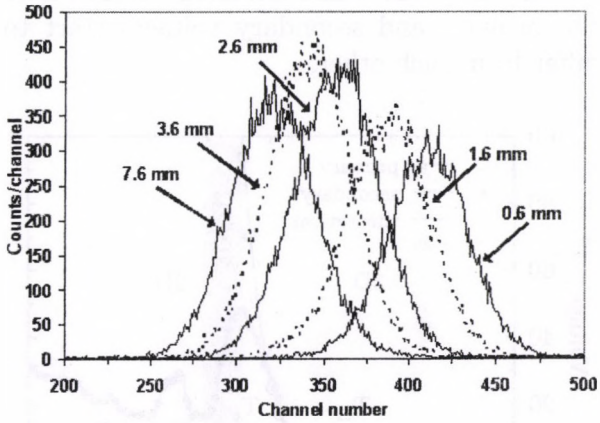

Figure 1. Pulse height spectra as a function of distance from the PMT. This distance corresponds to the depth-of-interaction.

This work was presented at the IWORID 04 conference and accepted for publication in Nuclear Instruments and Methods in Physics Research A.

a) Positron Emission Tomograph Center, University of Debrecen, Hungary

b) Royal Institute of Technology, Stockholm, Sweden

[1] J. Imrek et al., Nuclear Science Symposium and Medical Imaging Conference, Rome, October 16-22, 2004, to be published in IEEE Trans. Nucl. Sci.

4.11 Phase structure of layered superconductors

I. Nándori, K. Sailer[a)], K. Vad, S. Mészáros, J. Hakl

Performing current transport measurements on high transition temperature superconductor (HTSC) materials it is possible to study experimentally vortex properties and critical behaviour of layered systems. Recent measurements of the primary and secondary voltages in $Bi_2Sr_2CaCu_2O_8$ (BSCCO) single crystals in zero magnetic field using a multicontact 'DC flux transformer' configuration show a new qualitative picture of vortex phase diagram [1]. The onset of the secondary voltage is associated with the critical temperature T_{c1} where vortex loops start to be unbound. The first peak of the secondary voltage defines the 3D/2D phase transition temperature where the primary and secondary voltages start to differ from each other.

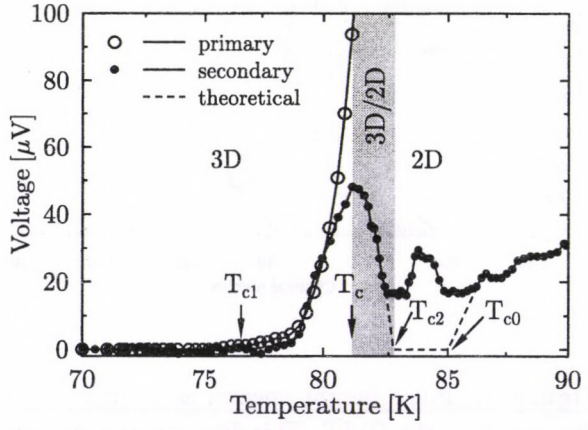

Figure 1. Primary and secondary voltages measured on the opposite surfaces of a BSCCO single crystal. The dashed line is the result of the RG analysis of Ref. [2].

Above T_c the experimental data disagree with the theory as it is shown in Fig. 1. A possible reason for the disagreement is the dilute gas approximation used in the theoretical RG analysis. By the modification of the RG analysis [2] using other RG approaches [3] one may go beyond the results of dilute gas approximation. One of the commonly accepted models to describe the phase structure of HTSC materials is the layered XY model. This can be mapped onto the layered sine-Gordon model (LSG), which has the following Lagrangian in case of two layers where ϕ_1, ϕ_2 are one-component scalar fields belonging to them

$$\begin{aligned} L &= \frac{1}{2}[(\partial\phi_1)^2 + (\partial\phi_2)^2] + \frac{1}{2}J(\phi_1 - \phi_2)^2 \\ &+ \sum_{n,m}\Big[u_{nm}\cos(n\beta\phi_1)\cos(m\beta\phi_2) \\ &+ v_{nm}\sin(n\beta\phi_1)\sin(m\beta\phi_2)\Big]. \end{aligned} \quad (1)$$

Here the second term describes the interaction of the layers. We propose a theoretical study of the critical behaviour of the layered LSG model using the Wegner-Houghton renormalization group (WH-RG) method [3] in order to treat the length-scale dependence of vortex interactions. The WH-RG equation has been derived in the local potential approximation. For 2D the well-known evolution equations for the coupling constants of the LSG model obtained in the dilute gas approximation [2] are recovered by means of the linearised WH-RG equations. Our approach offers a general scheme to go beyond the dilute gas approximation by solving the WH-RG for the LSG model numerically which is in progress.

Acknowledgements

This work has been supported by the project OTKA T037976 and the Supercomputing Laboratory of the Faculty of Natural Sciences, University of Debrecen.

a) Department of Theoretical Physics, University of Debrecen, H-4032, Debrecen, Hungary

[1] K. Vad, S. Mészáros, I. Nándori and B. Sas: submitted to Philosophical Magazine; I. Nándori, K. Vad, S. Mészáros, J. Hakl, Czech. Journal of Physics (2004) D481.

[2] S.W. Pierson, O.T. Valls, H. Bahlouli, Phys. Rev. **B45** (1992) 13035, S.W. Pierson, Phys. Rev. Lett. **74** (1995) 2359.

[3] I. Nándori and K. Sailer: submitted to Philosophical Magazine.

4.12 Study of magnetoresistance of $Eu_{0.8}Sr_{0.2}CoO_3$

J. Hakl, S. Mészáros, K. Vad, P.F. de Châtel, Z. Németh[a)], Z. Homonnay[a)], A. Vértes[a)], Z. Klencsár[b)], E. Kuzmann[b)], K. Kellner[c)], G. Gritzner[c)]

Following the discovery of the effect of colossal negative magnetoresistance (CMR) in doped manganite perovskites, a search for materials showing similar anomalous effects was started. Various transition metal compounds with different composition and crystal structure were also found to show large magnetoresistance effect.

Among these, the perovskite cobalt oxides $Ln_{1-x}B_xCoO_3$ (Ln: lanthanides B: alkaline-earth metal) show a couple of unic properties as the spin-state transitions or the 'glassy ferromagnetism' in $La_{1-x}Sr_xCoO_3$ [1]. In essence, the system evolves with Sr doping from a spin-glass or cluster-glass like phase to a ferromagnetic like state. In parallel the compounds become metallic. The phase boundary lies in the vicinity of $x_{crit} \approx 0.2$.

Room temperature MR effect was observed in few cobalt perovskite compound samples close to the critical composition range. However, neither the experimental nor the theoretical background of the latter phenomenon is known in all details.

In order to gain further insight into the magnetic and electronic nature of cobaltites at the phase boundary, $Eu_{0.8}Sr_{0.2}CoO_3$ was prepared and investigated by ac magnetic susceptibility, high field dc magnetization and magnetotransport measurements.

The results of magnetic measurements revealed ferromagnetic-paramagnetic transition at 133 K, and clear traces of glassy magnetic freezing at lower temperatures. These phenomena are explained by the formation and subsequent freezing of ferromagnetic clusters, which effect can be attributed to the spontaneous electronic phase segregation. The results of magnetotransport measurements are consistent with the magnetic data. The temperature dependence of the zero field resistivity is on the borderline of the metal-insulator transition with inflection points at 200 K and 100 K. At 200 K the relative reduction of the resistivity can be attributed to the reduction of spin-disorder scattering, which in turn is ascribed to the presence of short-range ferromagnetic fluctuations within the clusters up to 200 K. The MR ratio correspondingly starts to increase at 200 K.

In conclusion, we have strong evidence for magnetic cluster formation and cluster freezing in $Eu_{0.8}Sr_{0.2}CoO_3$. In contrast to $La_{0.8}Sr_{0.2}CoO_3$ the two effects are well separable, but the underlying magnetic behaviour shows analogous character.

This work was supported by the Hungarian Science Foundation (OTKA) under contracts T043565, F034837, T034839 and T037976 and the Wissenschaftlich-Technische Zusammenarbeit Österreich Ungarn project A-22/01.

a) Department of Nuclear Chemistry, Eötvös Loránd University, Pázmány P. s. 1/a, Budapest 1117, Hungary

b) Research Group for Nuclear Methods in Structural Chemistry of the Hungarian Academy of Sciences and Eötvös Loránd University, Pázmány P. s. 1/a, Budapest 1117, Hungary

c) Institute for Chemical Technology of Inorganic Materials, Johannes Kepler University, Altenbergerstrasse 69, A-4040 Linz, Austria

[1] J. Wu and C. Leighton: Phys. Rev. B 67 (2003) 174408

[2] J. Hakl, S. Mészáros, K. Vad, L. Kerekes, P.F. de Châtel, Z. Németh, Z. Homonnay, A. Vértes, Z. Klencsár, E. Kuzmann, K. Kellner, G. Gritzner, Czech. Journal of Physics 54 (2004), D307

[3] Z. Klencsár, Z. Németh, A. Vértes, I. Kotsis, M. Nagy, I. Cziráki, C. Ulhaq-Bouillet, V. Pieron-Bohnes, K. Vad, S. Mészaros, J. Hakl, Journal of Magnetism and Magnetic Materials 281 (2004) 115

4.13 Formation of nanocrystalline structure of $TaSi_2$ films on silicon

S.I.Sidorenko[a)], Yu.N.Makogon[a)], D.L.Beke[b)], A.Csik, S.N.Dub[a)], E.P.Pavlova[a)], O.V.Zelenin[a)]

An increasing interest in nanocrystalline materials has been revealed in the last decade, due to their potential, based on the possibility to control the structure at an atomic level, to replace traditional materials in many applications. Such a fine control allows tailoring the material with the optimum desired properties in magnetic, optical and catalytic applications. Regarding the mechanical parameters, fascinating properties can be reached, such as superplastic deformation behavior and super high hardness (over 50 GPa). One of the most interesting points in the super-hard materials is the possibility to simultaneously obtain very high fracture toughness values, by producing a structure of nanocrystalline grains embedded into an amorphous matrix [1]. The purpose of this work was to investigate the structure of the nanocrystalline $TaSi_2$ film sputtered onto the silicon substrate: results on the effect of the deposition rate, the annealing conditions and the contamination by O and C.

Thin films with thickness of 1000 nm were prepared by magnetron sputtering from a $TaSi_2$ target. Films were deposited on silicon substrate with two deposition rates: 0.2 nm/sec and 1 nm/sec. Samples were heat-treated in vacuum at $2{,}6 \cdot 10^{-3}$ Pa in the temperature range of 270 to 1270 K for one hour. For the identification of phases the X-ray diffraction method was used allowing also to receive information integrated over the film thickness. The atomic distributions of Ta, Si, O and C elements in depth after annealing were investigated using Auger electron spectroscopy (AES) and secondary ion mass spectroscopy (SIMS). Changes of the structure of the as-received and annealed $TaSi_2$ films were investigated by cross-sectional transmission electron microscopy (XTEM). As revealed, the decrease of the deposition rate leads to an increase of the amount of O and C impurities and this contamination cause the formation of an amorphous phase in deposited films. Upon annealing, the amorphous structure crystallizes into a mixture of disilicide and polysilicide (i.e., $TaSi_2$ and Ta_5Si_3, respectively). After annealing at 970 K, in film produced at the 0.2 nm/sec deposition rate, there is a formation of nanocrystalline structure with grain size of 10 nm. The formation of nanocrystalline structure drastically changed the mechanical properties of the film. The nanohardness and elastic modulus increased significantly and the film became brittle and overstressed.

In films deposited by 1 nm/sec rate both the basic Ta-disilicide and amorphous phase were observed. After annealing the amorphous phase near Si-substrate coexists with column-shape grains of Ta-disilicide of 150x500 nm size and the annealed thin film became nonuniform in thickness. At the same time the nanohardness and elastic modulus have been increased. With increasing the annealing temperature the resistivity of the film practically did not change. This is connected with the insignificant increase of the amount of the $TaSi_2$ phase.

a) National Technical University of Ukraine, prospect Peremogy 37, Kiev, Ukraine

b) Dept. of Solid State Physics, Univ. of Debrecen

[1] S. Veprek, A. Niederhofer, K. Moto, T. Bolom, H.D. Mannling, P. Nesladek, G. Dollinger, A. Bergmaier, Surface and Coating Technology 133-134 (2000) 152.

4.14 Stimulated structural transformations in amorphous semiconductor multilayers

A. Csik, D.L. Beke[a)], S. Kökényesi[b)], G.A. Langer[a)], I.A. Szabó[a)]

The nano-scale technologies provide new possibilities of creating materials and devices with peculiar characteristics for micro- and optoelectronics. Stability of nanostructured systems strongly depends on the interdiffusion processes, which in turn can be used for solid-state synthesis of multicomponent materials, optical recording [1]. Amorphous multilayers (AML) are attractive for these purposes because of the rather simple technology and modeling of physical processes, but the explanation of some physical effects, for example quantum confinement, blue shift of the absorption edge, diffusion on nano-scale are rather indefinite up today [2]. Stimulated intermixing depends on the temperature and the intensity of illumination, which also can heat up the layer. A model of surface relief formation due to the interdiffusion and the influence of illumination intensity on the amplitude recording process in three typical AMLs was discussed in this work.

Amorphous a-Se/As_2S_3, $As_6Se_{94}/Se_{80}Te_{20}$ multilayers with total thickness up to 0.8-2.0 μm and modulation period λ=5-8 nm were deposited by thermal evaporation in vacuum onto sapphire or quartz substrate. Si/Ge AML with a total thickness up to 0.1-0.3 μm and modulation periods λ=4-6 nm were prepared by DC magnetron deposition onto the same type of substrate. Small Angle X-Ray Diffraction (SAXRD) was used to investigate the periodicity and the quality of interfaces. SAXRD method was also used for the investigations of interdiffusion taking place during heat treatments and illumination. In situ monitoring of the change of the optical transmission with illumination time was performed.

Blue-shift of optical absorption edge ΔE_g=0.06-0.08 eV related to the absorption edge in homogeneous, 0.1-1.0 μm thick layers (the reference state was a layer, having the same composition as the "well" layers) was observed in all AMLs. Furthermore it is expected that with decreasing thickness of the "valley" layers, and/or with the appearance and growth of transition layers of mixed composition during interdiffusion, further ΔE_g shift (0.05÷0.1 eV) and further bleaching of the AML will be observed. Photo-induced changes of optical transmission τ were not observed in homogeneous a-Si, a-Ge, $Se_{80}Te_{20}$ layers at T≥290 K, but small photo-darkening ($\tau/\tau_o \leq 10\%$) was observed at 293 K in a-Se, As_6Se_{94} layers. The last fact is in accordance with the known photo-induced changes in As-Se system, which are due to the peculiar bonding configurations of chalcogen bridge atoms in all chalcogenide glasses. In a-Si/Ge system the bleaching disappears below 170 K even at the maximum value of P used (30 W/cm^3) but photo-darkening does not appears. It means that photo-induced structural transformations are not essential in Si/Ge AML, but the changes of optical parameters can be stimulated, as well as in all AMLs due to the activation of interdiffusion processes by heating. Our experiments support the model of two possible components of stimulated structural transformations due to the interdiffusion in investigated AMLs: the pure photo-stimulated and the thermally stimulated one.

a) Dept. of Solid State Physics, Univ. of Debrecen

b) Dept. of Experimental Physics, Univ. of Debrecen

[1] V. Palyok, A. Mishak, I. Szabo, A. Kikineshi, Appl.Phys. A 68 (1999) 489

[2] D. Nesheva, D. Arsova, Z. Levi, Phil.Mag. B 69 (1994) 205

4.15 Raman and X-ray diffraction studies of nanometric $Sn_2P_2S_6$

A.V. Gomonnai[a], *Yu. M. Azhniuk*[a], *Yu. M. Vysochanskii*[b], *A.A. Kikineshi*[b,c], *M. Kis-Varga, L. Daróczy*[c], *I.P. Prits*[b] *and I.M. Voynarovych*[b]

The last decade of the previous century gave rise to a keen interest in the studies of semiconductor microcrytals whose specific properties, resulting from the spatial confinement of charge carriers, have determined a wide variety of promising application possibilities. Semiconductors of the $Sn_2P_2S_6$ family have become an object of extensive theoretical and experimental interest in view of phase transitions and polycritical phenomena observed under variations of temperature, pressure and mixed crystal composition. $Sn_2P_2S_6$ crystals at ambient pressure undergo a second-order structural transition from ferroelectric (Pn) to paraelectric ($P2_1/n$) phase at 337 K which was studied by various methods for good quality bulk single crystals. In $Sn_2P_2S_6$ ceramics with grain size below 1 μm a decrease of the phase transition temperature by 12 K with respect to the bulk sample was observed by dielectric measurements.

We studied micro- and nanocrystalline $Sn_2P_2S_6$ samples by Raman spectroscopy. The crystals grown by chemical transport were milled in a stainless steel ball-mill under vacuum for increasing time periods (5, 25, 50 and 75 h) to obtain crystallite sizes down to the nanometer range. The grain size reduction was followed by measuring the XRD spectra of powders as seen on Fig. 1. The curves confirm that the $Sn_2P_2S_6$ lattice structure is preserved for the nanocrystalline samples. Our Raman scattering studies [1] of the nanocrystalline powders and powder-based ceramic samples have shown the general resemblance of the spectra to those of similar bulk crystals, but with some additional features, specific for the Raman spectra of the finest powder fractions. Namely, the observed slight downward shift and considerable broadening of the intense peak at 381 cm^{-1}, corresponding to the P-P bond vibration of the $(P_2S_6)^{4-}$ anions, with the average grain size decrease, is explained by the increasing role of the surface phonons due to the high suface-to-volume ratio in nanocrystals. The contribution of the confinement-related selection rules relaxation in the observed effect was also discussed. An additional band at 406 cm^{-1}, revealed only for the finest powder fractions, is related to the partial substitution of sulfur in $(P_2S_6)^{4-}$ anions by oxygen at the nanocrystal surface.

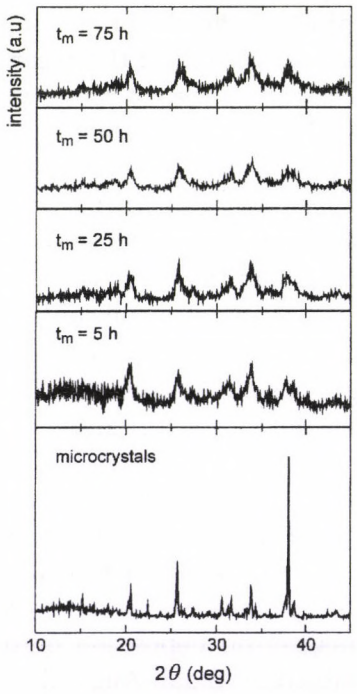

Figure 1. XRD patterns of ball-milled $Sn_2P_2S_6$ powders.

a) Institute of Electron Physics, Ukrainian National Academy of Sciences, Universytetska Street 21, Uzhhorod 88017, Ukraine

b) Uzhhorod National University, Pidhirna Street 46, Uzhhorod 88000, Ukraine

c) Department of Solid State Physics, University of Debrecen, P.O.B. 2, 4010 Debrecen, Hungary

[1] A.V. Gomonnai et al, J. Phys.: Condensed Matter 15 (2003) 6381

4.16 Surface excitation correction of the inelastic mean free path (IMFP) of electrons determined by EPES experiments

G. Gergely[a)], M. Menyhárd[a)], S. Gurbán[a)], J. Tóth and D. Varga

The IMFP of electrons [1] was determined by EPES [2] on Si, Ag, Ni, Cu and Au sample pairs using them also as reference materials. The experiements (elastic peak area measurements) were made by a home-built HSA (hemispherical analyser) based electron spectrometer with high energy resolution [3]. For the evaluation of experiments Monte Carlo simulation was applied which based on a new software package EPESWIN of Jablonski and the TPP-2M IMFP data of Tanuma. IMFPs deduced from EPES experiments without correction are different from calculated data of Tanuma [1]. The difference was attributed to surface excitation (SEP). Parameters of Chen [4] were applied for correcting the integrated elastic peak ratios of the sample pairs. Experiments covered the 0.2–2 keV energy range using the ESA 31 HSA (ATOMKI) [3] and DESA 100 (Staib) spectrometers [5]. The correction factors were determined by a trial and error procedure. For every sample pair the correction of IMFPs reduced the deviations from Tanuma's data, but perfect correction was not achieved. The same was found on the experimental elastic peak ratios and their MC simulation. Jabłoński's EPESWIN software [6] resulted in better agreement with experiments than previous approach [5].

Acknowledgements

This project was supported by the Hungarian Science Foundation of OTKA: T037709 and T038016.

Note: The paper was an oral presentation by G. Gergely at ESS-04 IUVSTA Workshop (Chairmen: C.J. Powell (NIST) and L. Kövér) 4-8 July 2004, Debrecen, Hungary.

a) Res. Inst. Techn. Phys. & Mat. Sci. 1525 Budapest. P.O.Box.49

[1] C.J. Powell and A. Jabłoński, J. Phys. Chem. Ref. Data 28 (1999) 19.

[2] G. Gergely, Progr. Surf. Sci. 71 (2002) 31.

[3] L. Kövér, D. Varga, I. Cserny, J. Tóth and K. Tőkési, Surf. Interf. Anal. 19 (1992) 9.

[4] Y.F. Chen, Surf. Sci. 519 (2002) 115.

[5] G. Gergely et al, SIA (accepted).

[6] A. Jabłoński et al, J. Phys. Chem. Ref. Data (in press).

4.17 Surface excitation correction of electron IMFP of selected polymers

G. Gergely[a)], G.T. Orosz[a)], B. Lesiak[b)], A. Jabłoński[b)], J. Tóth and D. Varga

The IMFP [1] of selected polymers: polythiophenes, polyanilines, polyethylene (PE) [2] was determined by EPES [3] experiments, using Si, Ge and Ag (for PE) reference samples. Experiments were evaluated by Monte Carlo (MC) simulations [1] applying the NIST 64 (1996 and 2002) databases and IMFP data of Tanuma and Gries [1]. The integrated experimental elastic peak ratios of sample and reference are different from those calculated by Monte Carlo (MC) simulation [1]. The difference was attributed to the difference of surface excitation parameters (SEP) [4] of the sample and reference. The SEP parameters of the reference samples were taken from Chen and Werner. A new procedure was developed for experimental determination of the SEP parameters of polymer samples. It is a trial and error method for optimising the SEP correction of the IMFP and the correction of experimental elastic peak ratio [4]. Experiments made with a HSA spectrometer [5] covered the E = 0.2−2 keV energy range. The improvements with SEP correction appears in reducing the difference between the corrected and MC calculated IMFPs, assuming Gries and Tanuma's et al IMFPs [1] for polymers and standard respectively. The experimental peak areas were corrected for the hydrogen peak. For the direct detection of hydrogen see Ref. [6] and [7]. Results obtained with the different NIST 64 databases and atomic potentials [8] are presented.

Acknowledgements

This work was supported by the Hungarian Science Foundation of OTKA: T037709 and T038016.

Note: The paper was a poster presentation by G. Gergely at ESS-04 IUVSTA Workshop (Chairmen: C.J. Powell (NIST) and L. Kövér) 4-8 July 2004, Debrecen, Hungary.

a) Res. Inst. Techn. Phys. & Mat. Sci. 1525 Budapest. P.O.Box.49

b) Inst. Phy. Chem. PAS. 44/52 Kasprzaka, Warsaw, Poland

[1] C.J. Powell and A. Jabłoński, J. Phys. Chem. Ref. Data 28 (1999) 19.

[2] B Lesiak et al, Langmuir 16 (2000) 1415, Surf. Sci. 70 (2001) 174; ibid.507 (2002) 900.

[3] G. Gergely, Progr. Surf. Sci. 71 (2002) 31.

[4] G. Gergely et al, Appl. Surf. Sci (in press).

[5] L. Kövér, D. Varga, I. Cserny, J. Tóth and K. Tőkési, Surface and Interface Anal. 19 (1992) 9.

[6] G.T. Orosz, G. Gergely, M. Menyhárd, J. Tóth, D. Varga, B. Lesiak, A. Jabłoński, Surface Science 566 (2004) 544.

[7] G. Gergely, M. Menyhárd, A. Sulyok, G.T. Orosz, B. Lesiak, A. Jabłoński, J. Tóth, D. Varga, Surface and Interface Analysis 36 (2004) 1056.

[8] A. Jabłoński et al, J. Phys. Chem. Ref. Data (in press).

4.18 Electron IMFPs determined by XPS using different energy X-ray excitations

J. Tóth, I. Cserny, L. Kövér, D. Varga

In this study a combination of a home built conventional XPS X-ray source with a specially designed "hard" X-ray source for the excitation of Auger lines of the few keV energy range is presented including the main characteristics of the two X-ray tubes.

The home built XPS-XAES-REELS instrument (ESA-31) [1] equipped with different X-ray sources [2] (Al, Mg, Cu, Mo) has been used for studying different polycrystalline materials: Au, Ag and Cu.

Assuming that the photo ionisation cross sections and the detecting efficiency correction factors are known, the energy dependence of the ratios of the respective inelastic mean free paths can be determined in the high energy range using various energy (e.g. Cu, Mo) X-rays for excitation. The energy dependences of the IMFP determined by EPES and XPS are compared.

Acknowledgements

The financial support was from the Hungarian National Science Foundation OTKA T038016. The authors are indebted for the fine micro-crystalline Cu standard specimen to the Surface Analysis Society of Japan, especially to Dr. Shigeo Tanuma and Professor Keisuke Goto (Nagoya Institute of Technology).

Note: The paper was a poster presentation by J. Tóth at ESS-04 IUVSTA Workshop (Chairmen: C.J. Powell (NIST) and L. Kövér) 4-8 July 2004, Debrecen, Hungary.

[1] L. Kövér, D. Varga, I. Cserny, J. Tóth and K. Tőkési, Surf. Interf. Anal. 19 (1992) 9.

[2] J. Tóth, Gy. Molnár, D. Varga, I. Cserny, L. Kövér et al, ECASIA-2001 Abstr.: p.293.

5.1 The Tisza-project - challenges and perspectives

Zs. Szántó, É. Svingor, S.A. Nagy[a)], I. Futó, L. Palcsu, Á. Elek[a)], D. Fürj[a)], M. Molnár, L. Rinyu

In the recent years, the Tisza river basin has come to the forefront of international attention due to a sequence of major flood events and environmental disasters with the Baia Mare cyanide spill leading the headlines. Although accidental pollution has usually higher publicity, the permanent pollution of the River Tisza is the main determining factor of the water quality in the long run. Permanent pollution originates on the one hand from industrial activities, where mainly inorganic micro-contaminants are released to the water. On the other hand, it derives from agricultural activities and municipal sewage discharges. The use of fertilizers and pesticides in agriculture may contribute to a significant nutrient and chemical load in the Tisza and its tributaries while sewage discharges from settlements and animal husbandry influence the organic matter content and the bacteriological characteristics of the water.

The goal of the running national project is to provide scientific foundation of the hydroecological state assessing, monitoring and databank organising program of River Tisza and Upper Tisza-Region. The main objective of the project is to help saving the water resources and ecological values with the help of integrated catchment management tools and to secure the sustainable use of the resources of the Tisza River Basin.

In the second phase of this project the task of our laboratory was the investigation of the origin and mixing of water in the catchment area of upper Tisza and its tributaries. Water samples were obtained to capture "snapshots" of present site-specific hydrological status. The sampling sites along the Tisza river show more or less the same characteristics with similar anion and cation concentrations. Differences in sulphate, chloride, calcium or sodium content were typical for the major tributaries which have bigger catchment area and originating farer from the sampling points.

The ICP measurements show minor heavy metal pollution (especially in Szamos tributary) but all the values were under the acceptable limits.

Secondly, tritium (^{3}H) and stable isotope ratios (δD, δ^{18}O, δ^{15}N, δ^{13}C) were measured in water samples taken from the catchment area. The δ^{18}O values of the water samples taken along the Tisza river plotted nicely on the GMWL and even on the LMWL. The differences that we observed were in all cases related to the Tisza tributaries: the Belfő channel, the Lónyai channel and Kraszna river. All the data value recorded in case of these tributaries plotted below the GMWL because of their small catchment area and their faster reaction to snowfall or winter rainfall that is characterized by a more negative delta value. In small drainage systems where surface runoff from recent precipitation is the main source of flow, δ^{18}O of the water is equal to that of the local precipitation. The Tisza river transporting water over large distances there is not sensitive to local precipitation or overland runoff influences. No difference between summer and winter tritium concentration values was found. The bigger tributaries with an extended catchment area show a slow transition between summer and winter tritium data and entering into the Tisza river slightly modify (function of their debit) the measured tritium concentration. The lower tritium concentration values of the two channels support the conclusion drawn from the stable isotope results: the water used for communal purposes originates from old, deep subsurface water body and fed the Lónyai and Belfő channels.

Acknowledgments

The project was/is supported by the National Research and Development Program (NKFP-3B/0019/2002) Hydroecology of River Tisza and Upper Tisza-Region.

a) University of Debrecen, Dept. of Hyrdobiology

5.2 Radiocarbon dating of the first Turkish bridge over the River Tisza

Zs. Szántó, M. Molnár, R. Kertész[a)], A. Morgós[b)], I. Futó, É. Svingor, L. Rinyu, L. Palcsu

Situated at the junction of the Tisza and Zagyva rivers, the territory of the present-day Szolnok town has been nearly continuously inhabited since the beginning of the Neolithic age. Gravures and other written documents attested the presence of bridge(s) over the River Tisza during the centuries. The first bridges were mentioned in 1526 as temporary pontoon bridges used for the needs of the Turkish army.

The remainings of an old bridge on the River Tisza were discovered last summer in excavations of the river bank at Szolnok. It was supposed that the remainings found were probably part of the bridge built in 1562, the first wooden bridge over the River Tisza mentioned in the letter of bishop of town Eger [1] but could also been parts of a bridge built much later.

Although the mineral water and sodium silicate have penetrated the wood logs resulting in though blackish-brown and hardened by petrifaction samples, the original character of the pylons was still evident. Six timbers (7 samples) have been radiocarbon dated. Samples were physically and chemically pretreated to remove contamination before they were converted to CO_2. In order to avoid the "old wood" effect, in which the inner tree rings may be tenths of years older than the outer ring of sapwood deposited just before the tree died the exterior was removed. Physical treatments consisted of cleaning, sorting, grinding and sieving. Chemical treatment included the standard A/A/A method. The pre-treated samples were combusted to CO_2 in a controlled oxygen stream. The purified CO_2 was trapped and measured by gas proportional counting [2]. Correction for fractionation was done by measuring the $\delta^{13}C_{PDB}$ value. Calibration of ^{14}C dates to calendar years was performed using the Calib 4.4.2 program [3].

The results showed the wood sample prepared by A/A/A contained contaminants of more recent carbon material which gave it a more recent date and spread the results over four centuries. In order to avoid humic acids, as well as lignin alpha-cellulose was extracted from the wood samples by bleaching with $NaClO_2$ solution under acidic condition. Alpha-cellulose was separated finally by washing the residue with NaOH and dried. Using alpha-cellulose for dating the estimation of the extent to which the formation of the wood predated the archaeological event of interest became more precise due to the fact that exchange with the reservoir ceases at cellulose formation.

Dating alpha-cellulose two different time periods were obtained: the first period (1505-1595 AD and 1612-1673 AD, respectively) coincides with the Turkish occupation period, while the second interval (1733-1813 AD) proved the existence of another bridge from the 18^{th} century. The dendrochronological data (1558-1565 AD) [3] confirmed the assumed calendar time span, the archaeological excavation revealing without doubt the proof of the first wooden bridge over the River Tisza.

a) Damjanich János Museum, Szolnok

b) Hungarian National Museum, Budapest

[1] Verancsics Antal összes munkái. 8. kötet. Vegyes levelek. Monumenta Hungariae Historica 19. Pest, MTA Történelmi Bizottsága, 1868.

[2] E. Hertelendi, É. Csongor, L. Záborsky, J. Molnár, J. Gál, M. Győrffi, S. Nagy: A counter system for highprecision ^{14}C dating. Radiocarbon 31(3) 399-406, 1989.

[3] M. Stuiver, P.J. Reimer: Extended ^{14}C database and revised CALIB radiocarbon calibration program. Radiocarbon 35(1):215-230, 1993.

[4] Kertész R, Morgós A, Nagy D, Szántó Zs. Az első híd a Tiszán, Szolnoki Tudományos Közlemények VIII: 1-13, 2004.

5.3 Application of Safety Assessment Methodologies to LILW Repository in Hungary

Zs. Szántó, K. Bérczi[a)], P. Ormai[b)], L. Juhász[c)]

Existing repositories for low and intermediate level radioactive waste in many countries do not fully comply with current regulations and internationally accepted standards, raising the questions whether action to upgrade safety of these facilities is required and, if so, which corrective measures are necessary to achieve long-term safety. Answering these questions requires a systematic safety assessment, for which the IAEA provides guidance within the research projects ISAM and its successor ASAM, directed at the practical application of the methodology developed within ISAM. A typical example of such a facility is the Püspökszilágy Radioactive Waste Treatment and Disposal Facility which, therefore, has been chosen as a test case for the ongoing ASAM project.

From the results of the safety analysis conducted for the Püspökszilágy facility it can be concluded that the present operation and the safety up to the end of the passive institutional control period is properly guaranteed. The facility as a whole is suitable for safe disposal of low and intermediate level short-lived wastes. Beyond the passive institutional control period, however, inadvertent human intrusion - or any other scenario resulting in surfacing of waste after deterioration of concrete barriers - could result in exceeding both, the dose constraint and the dose limit. This is mainly due to the significant amount of long lived radionuclides already disposed of (^{14}C, ^{226}Ra, ^{232}Th, ^{234}U, ^{235}U, ^{238}U, ^{239}Pu and ^{241}Am) and also caused by the high activity of disposed ^{137}Cs sealed sources.

According to the iterative nature of the ISAM methodology [1], it was assessed whether a change of the assessment context (e.g. longer institutional control period, extend the size of the area subject to institutional control, modification of WAC, review of dose criteria) or an improvement of the databases, models and scenarios was likely to change the conclusion with regard to the long-term assessment. Since this was, within the technical possibilities and the regulatory permissible boundaries, not expected to be the case, the process of evaluation and ranking options for corrective actions was started.

The following options were identified as in principle viable to upgrade safety of the repository:

1. Reconstruction of cap system (clay cap);
2. Backfilling of the vaults (reduction of cap settlements and water ingress to the wastes);
3. Groundwater cut-off wall;
4. Partial/full recovery of spent sources;
5. Compaction and repackaging of other waste; and
6. Improvement of record keeping and installation of markers.

These fundamental options have several sub-options. It will also be possible to combine some of the options, such as the improvement of the cap (Option A) with the backfilling of the vaults (Option B). The complexity of available options and attributes requires a methodical approach to the evaluation and ranking of the options in order to arrive at a transparent decision which also can be communicated to stakeholders. On this basis, currently a multi-attribute utility analysis is being conducted. The work required to define attributes and weighting factors and to evaluate the options using these attributes is ongoing.

a) ETV-ERŐTER., Budapest

b) RHK KHt Budaörs, Hungary

c) OSSKI, Budapest

[1] IAEA (2002) Improvement of Safety Assessment Methodologies for Near Surface Disposal Facilities. Results of a co-ordinated research project. Draft final report, IAEA.

5.4 Paleoclimate reconstruction based on tritium and radiocarbon measurements at Focul Viu Ice Cave, Bihor Mts., Romania

Zs. Szántó, L. Palcsu, M. Molnár, I. Fórizs[a)], Z. Kern[a)], B. Nagy[a)], É. Svingor, I. Futó, L. Rinyu

For predicting the climate change in the near future we have to understand the climate change happened in the past. Several methods and tools have been developed or are under development for palaeoclimate reconstruction (palynology, dendrochronology, isotope analysis, etc.) but none of them can reveal perfectly the past changes in the climate.

Little research has been devoted to the role of cave ice in palaeoclimatology despite the fact that a significant number of ice caves in temperate climatic region contain ice and wood remnants from same site and probably same time span. In Romania numerous studies dealt with the relation between ice formation, external climate and cave climate, respectively [1-2] but there is still limited information on the process of ice formation, age of ice and growth rate of ice.

Perennial ice block of about 14 meter vertical thickness and estimated volume of 12 000 m^3, including subfossil wood, can be found in the Focul Viu Ice Cave, Bihor Mountains, Romania at 1120 m elevation a.s.l. on a karstic highland under temperate climate. The annual mean temperature of the highland area is about 7 °C. The cave ice forms mainly from drip water in springtime, when the temperature of the ice and the rock wall is below freezing point in the cave and over freezing point on surface.

Near-surface samples were taken from the upper surface and the side wall of the ice block for tritium, $\delta^{18}O$ and δD measurements [3] and two wood samples were extracted from different depths (6.7 m and 11.1 m, respectively) for radiocarbon dating.

The tritium activity-concentration indicates 1.9 cm/yr short-term growth rate for the ice, while the long-term growth rate based on radiocarbon ages gave 0.85 cm/yr. This big difference between the long and short term growth rates confirms the theory that on long time span (few hundred years) there were periods when the balance of ice growth was negative, more ice melt than formed. This conclusion was supported by the dark impurity (horizontal) layers distributed unevenly along the vertical profile, which were probably formed during the ice-melting periods. Additionally, since the ice in the Gheţarul de Focul Viu ice cave usually forms during spring, the isotopic feature of ice characterizes the springtime water of the cave. The sources of water in the Gheţarul de Focul Viu ice at spring are infiltrating melt water and spring precipitation, which directly arrives into the cave.

a) Laboratory for Geochemical Research, Hungarian Academy of Sciences, Budapest, Hungary

[1] Gh. Racoviţa, M. Şerban, I. Viehmann, Tendences de long terme dans la dynamique des formations de glace de la Grotte de Scărişoara (Monts de Bihor), Theoretical and Applied Karstology, 1987, vol. 3 pp. 143-164.

[2] Gh. Racoviţa, M. Şerban, Interpretation en vue d'une reconstruction paleoclimatique des particularités structurales et dynamiques du dépot de glace pérenne de la Grotte de Scărişoara, Studia universitas Babes-Bolyai, Geologia, 1990, XXXV, 2, pp. 47-61.

[3] I. Fórizs, Z. Kern, B. Nagy, Zs. Szántó, L. Palcsu, Isotopic composition of perennial ice cave as a proxy for paleoclimate: the Focul Viu Ice Cave, Bihor Mts., Romania, International Conference on Isotopes in Environmental Studies - Aquatic Forum 2004, 25-29 October 2004 Monte Carlo, Monaco, IAEA-CN-118/27.

5.5 Monitoring of gas generation during the charge/discharge regime of miners' headlamps

Zs. Szántó, M. Molnár, L. Palcsu, I. Futó, L. Rinyu, É. Svingor

The miners' headlamp combines a battery pack for waistbelt mounting with a detachable headlamp/cable unit. The battery that incorporates the Ni/Cd "gel-cells" and the KOH electrolyte (which acts only as an ion conductor and does not contribute significantly to the cell's reaction) is the most important piece of the lamp.

The total reaction of the NiCd cell is:

$$2NiOOH + 2H_2O + Cd \Leftrightarrow 2Ni(OH)_2 + Cd(OH)_2$$

The preferred charging regime for caplamps is top-up charging with an occasional full discharge cycle. Nickel-cadmium cells are charged by applying direct current with the proper polarity to the cell. That means the charger will deliver a constant amount of current to the battery regardless of its voltage.

During the first 70% of the charge cycle, a NiCd battery absorbs almost all of the energy and the battery remains cool. After the 70% charge threshold is reached, less and less energy is absorbed. The cells start to generate excess gases the pressure rises and the temperature increases. The charge acceptance drops further and once full charge is reached, the battery goes into overcharge. The higher the overcharge rate the higher the rate of gas generation.

The battery made up of three NiCd cells has the potential for cell reversal problems when the discharge is deep enough to bring one or more of the cells in a battery to zero voltage. If discharge continues beyond this point, the voltage on the depleted cell will reverse polarity. The problem that occurs is the generation of hydrogen gas. As the electrodes change polarity they will generate hydrogen. Since the hydrogen will not recombine, the internal cell pressure will build up to a level that causes the cell to vent if the reverse charge current is maintained for a significant period of time.

Due to the potential hazard during underground working gas emission generated into the cells and the amount of vented gas is strictly regulated 1 .

The three characteristics of cell chemistry which indicate charge completion are temperature, voltage and internal cell pressure. As a cell nears full charge, the voltage of the cell, its temperature and pressure all will rise. Full charge detection followed by discharge was achieved under laboratory conditions by monitoring the battery voltage, current and pressure build up terminating the charge when a certain signature occurs (the initially set voltage was reached). Sampling (1 cm^3 of headspace gas) was made at regular intervals and the qualitative and quantitative analysis of gases of the battery was made using a QMS (OMNISTAR, Balzers Instruments). Monitoring of gas generation was made during 16 and 72 hours charge periods followed by 12-13 hours discharge periods.

The results showed a constant increase in pressure (up to 2 bars) into the checked cells during the charge period, the generated gases being the following: CH_4, H_2 and O_2. The voltage of the three cells increased to 4.40 V while the charge current dropped from 1 A to 0.5 A. During discharge a decrease of the cell voltage was observed a sharp drop being recorded (from 3.0 V to 2.85 V) after 12-13 hours. The excess oxygen generated during the charge period reaching the active sites on the negative plate was recombined from the gaseous state forming hydroxyl ions, so its concentration decreased in the headspace gas.

The study showed an increase of up to 19% of H2 into the cells during the 72 hours charge period and up to 15% of H2 into the space between the battery and its outside polycarbonate case, which is not acceptable for underground mining activities.

[1] International Electrotechnical Commission 2002. Caplights for use in mines susceptible to firedamp, IEC 62013-2, pp. 1-7.

5.6 Isotope analitical investigation of old and fresh water mixing in a karstic aquifer

M. Molnár, L. Palcsu, Z. Major, I. Futó, É. Svingor, L. Rinyu, Zs. Szántó

The studied area is the part of the Aggtelek karst system, Hungary. The Pasnyag spring and the Lótusz spring are located one after the other nearby the Alsó-hill. The water of the Pasnyag spring applied as drinking water. From the local hydrogeological conditions it is possible that fresh and old ground water components are mixed in the springs. This fact is also confirmed by the water quality data.

The objective of this work was to determine the mixing ratio of the water of different origin in the springs. Repeated water sampling has been carried out around the site from the springs and two monitoring wells (F1 and F4) for two years. The F1 monitoring well is near at hand the Pasnyag spring, and the F4 well is between the two springs. The water quality of the Pasnyag spring and the nearby F1 well is significantly different.

Helium content and isotope ratio, tritium concentration (by ^{3}He ingrowth method), radiocarbon content of dissolved inorganic carbon (DIC), and δD, δ^{13}C, δ^{18}O isotope ratios were measured from the water samples.

On the basis of isotope measurements the water of the springs and the observed monitoring wells are composed of fresh and old components in different ratios. The fresh component is dominant in the Pasnyag spring. The tritium and radiocarbon concentration of this water show that it is fresh, young water directly from the karstic system, with only small amount of DIC from the limestone. The helium concentration and isotope ratio in the water of this spring also shows that the subthermal water component is not significant. Higher ratio of the fresh karstic water also detectable in the far F4 monitoring well, but it has slightly lower tritium and ^{14}C content. In the Lótusz spring and the F1 well (nearby the Pasnyag spring) higher ratio of the subthermal water was observed. The low tritium and radiocarbon content show together that these waters contain high amount of old water. The higher helium content and the higher radiogenic ^{4}He ratio of the water also indicate subthermal origin in these cases.

5.7 The origin of the methane in deep aquifers of the Pannonian Basin

I. Futó, I. Vető,[a)], É. Svingor, I. Horváth,[a)], Zs. Szántó

Bacterial methanogenesis and thermally induced generation of gaseous and liquid hydrocarbons have long been considered as processes strictly separated in space and time [1]. As the compositional and isotopic analysis of the hydrocarbon gas (HC) became a routinely used technique in petroleum exploration, the beginning of thermal gas generation in relatively cold and immature strata was recognized [2]. The discovery of living bacteria at temperatures as high as 50-55 °C implied that bacterial methane may be formed at temperatures considerably higher than previously supposed.

The great number of water wells penetrating the deep aquifers of the hot Pannonian Basin, which is at the same time a mature petroleum province, offers a unique possibility for studying the spatial and temporal relationships between bacterial methanogenesis and thermal generation of HC gases.

H and O isotope ratios of water and H and C isotope ratios of methane as well as the abundances of some major and minor dissolved components were measured in 26 subsurface waters from SE Hungary, produced from late Neogene aquifers within the upper two kilometers in depth [3].

The HC gas content of the great majority of the waters is dominated by isotopically light bacterial methane. The depth of the onset of thermal gas generation varies from 0.7 to 1.2 km but the amount of thermogenic methane leaving the kerogen was not sufficient to overprint the light isotopic signature of the methane in the waters. About two thirds of the waters are characterised by low sulfate content (<5 mg/l), high chloride/sulfate ratio (>20) and methane δD values less negative than -260%. They also show a direct relationship between the H isotope ratio of the methane and that of the water. These waters experienced exhaustive bacterial sulfate reduction followed by a relatively shallow bacterial methanogenesis. The methanogens started to operate immediately after the sulfate content dropped below 0.1 mmol/l due to bacterial sulfate reduction.

In about one third of the waters the methane δD values are more negative than -278%. These samples contain a relatively high amount of sulfate (35-45 mg/l) and do not show a direct relationship between the H isotope ratio of the methane and that of the water. In this waters sulfate reduction was inhibited by some unknown mechanism and, with continuing burial, the corresponding aquifers became sites of intensive bacterial acetogenesis and subsequent fermentation of the acetate to methane in the depth interval of about 600-1000 m at temperatures of about 40-60 °C. The effectiveness of the acetate fermentation was highly variable. During the last glacial period meteoric waters invaded some of the corresponding aquifers, reducing drastically the concentrations of methane.

The minor amounts of ethane and other heavy hydrocarbon gases are mostly of early thermogenic origin. The contribution of early thermogenic methane is too slight to alter significantly the very negative, bacterial C isotopic signature of the methane present in the waters.

Our results show that deep, hot acetate fermentation and early thermal gas generation can occur closely in space and time and even partly overlap.

a) Geological Institute of Hungary, Budapest

[1] Tissot, B.P., Welte, D., 1984. Petroleum Formation and Occurrence, 2nd Edition. Springer, Berlin.

[2] Faber, E., Stahl, W.J., Whiticar, M.J., 1992. Distinction of bacterial and thermogenic hydrocarbon gases. In: Vially, R. (Ed.), Bacterial Gas. Technip, Paris, pp. 63-74.

[3] I. Vető, I. Futó, I. Horváth and Zs. Szántó, 2004. Late and deep fermentative methanogenesis as reflected in the H-C-O-S isotopy of the methane-water system in deep aquifers of the Pannonian Basin (SE Hungary) Organic Geochemistry 35(6) 713-723

5.8 Interpretation of temporal changes of isotopic composition in precipitation in Hungary by meteorological data and satellite images

L. Palcsu, É. Svingor, Zs. Szántó, I. Futó, M. Molnár, L. Rinyu, R. Rozinai, Z. Dezső[a)]

Rainfall events are continuously sampled in Debrecen, East-Hungary from December 2000. In this study we focused on the variation of tritium in the precipitation. The tritium concentration of water samples are measured by the ^{3}He ingrowth method. The accuracy of the measurements is 0.1-0.6 TU depending on the tritium content of the samples. Fig. 1 shows the tritium data of the precipitation events. The tritium curve is quite variable, there can be observed sharp peaks and changes which require explanations.

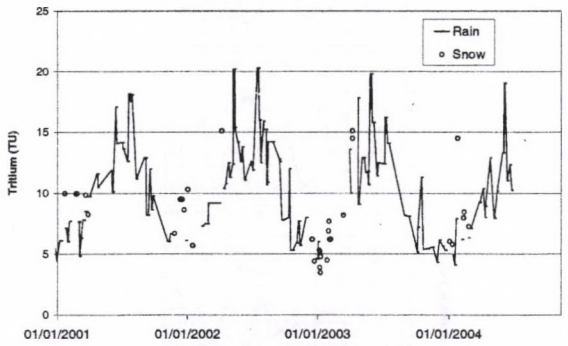

Figure 1. The tritium content of the precipitation

On the basis of satellite images (© EUMETSAT 2001-2004) we determined trajectories in order to decide which moisture source brought the water vapor. On the one hand the isotopic composition of precipitation depends on the moisture source, which provides the rainfall. On the other hand, the seasonal, continental and latitude effects have to be taken into account to explain the temporal changes.

The samples from rainfall events were separated into four groups according to the source of water vapor determined from the trajectories. The four groups are the following: the Mediterranean group contains precipitation samples originated from the Mediterranean Moisture Source, the trajectories of these events pass through the Mediterranean Sea. The tritium curve of this group is plotted in Fig. 2 as dotted line with full circles. The Atlantic and the North-Western groups include water samples from Atlantic and North-Western streams from the mid-latitude Atlantic region and the Arctic region over the Northern Sea, respectively. The corresponding tritium curve can be seen in Fig. 2 as thick line with full squares and thin line with triangles. The other air mass streams, like streams from the Asian continent and local, very slow streams called 'static streams' belong to the Continental group. The tritium data of the Continental group are represented in Fig. 2 by thick solid line with open circles.

The seasonal changing can be seen in each curve, which implies that the tropospheric and stratospheric tritium has a reliable influence to the tritium content of the precipitation independently on the moisture source. While in 2001 and 2002 the tritium curve of the Mediterranean group was similar to the Atlantic and the North-Western, from 2003 its tritium values were lower than those in the other groups. The precipitation from continental and static streams had the highest tritium content, which could be explained with the continental effect.

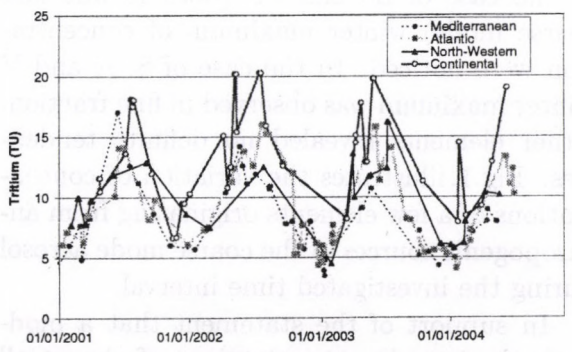

Figure. 2. The tritium content of the precipitation samples separated into four groups

a) Univ. of Debrecen, Dept of Environmental Physics

5.9 Changes in the elemental concentration of PM10 and PM2.5 aerosol during the last seven years

I. Borbély-Kiss, E. Dobos, Zs. Kertész E. Koltay Gy. Szabó

For the qualification of local air at a given region the total particulate mass and its elemental composition are usually used. The aim of this work was to follow the variation of the elemental concentration in the region, both in PM10 (coarse mode) and PM2.5 (fine mode) aerosol fractions.

Aerosol samples were collected in Debrecen between 1996 and 2003 twice a week with a two-stage "GENT" SFU (stacked filter unit) sampler. Total airborne particulate mass (PM10 and PM2.5) was measured using a Sartorius microbalance. The black carbon content of fine aerosol was determined by a Smokestain reflectometer. Samples were analyzed by PIXE and elemental concentrations of Al, Si, P, S, Cl, K, Ca, Ti, V, Cr, Mn, Fe, Ni, Cu, Zn, As, Br, Pb were calculated.

Monthly average concentrations of the above elements were calculated from the database obtained by the analyses. From the variation of the monthly average concentrations the following conclusions were drawn. Concentrations of Si, Ca, Ti and Fe elements both in fine and coarse mode have their maximum in summer, and it seems their values are decreasing from 1996 to 2000. From 2000 to 2003 stagnation or moderate increase can be observed. In the case of Zn and Pb (both in fine and coarse mode) winter maximum of concentration were noticed. In the case of S, K and V winter maximum was observed in fine fraction. Other elements revealed no definite tendencies. Fig.1. illustrates the variation of concentrations of a few elements originating from anthropogenic sources in the coarse mode aerosol during the investigated time interval.

In support of the statement that a moderate decrease in concentrations of almost all elements can be observed correlation coefficients between the elemental concentrations and elapsed days were calculated for the total 1996-2003, and also for the 2000-2003 time periods. Coefficients indicate definite decrease in concentration of almost all elements in both aerosol fractions for the whole period (1996 to 2003) and do not show significant decrease in concentrations in 2000-2003 time period. These results and the fact that in the last four/five years the number of cars increased with about 20000 in Debrecen indicate that trafic as an emission source is increasing in the region from 2000.

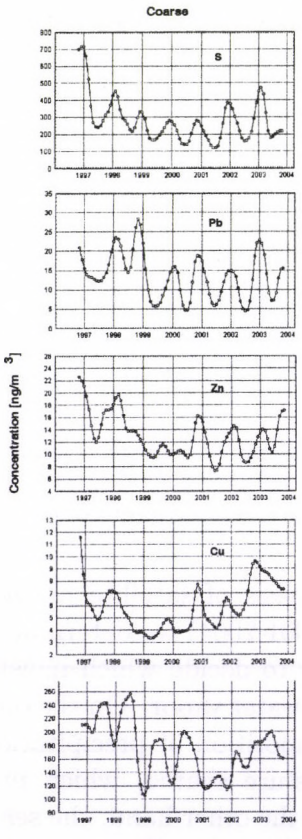

Figure 1. Monthly average concentrations of S, Pb, Zn, Cu and K in the coarse mode aerosol from 1996 to 2000.

Acknowledgements

This work was supported by the Hungarian National Foundation for Scientific Research (OTKA No. T032264) and National Research and Development Program (NRDP 3/005/2001).

5.10 Atmospheric aerosol sampling campaign in Budapest and K-puszta: Part I. Elemental concentrations and size distributions

E. Dobos, I. Borbély-Kiss, Zs. Kertész, Gy. Szabó, I. Salma[a)]

Atmospheric aerosol samples were collected in a sampling campaign from 24 July to 1 August, 2003 in Hungary. The sampling were performed in two places simultaneously: in Budapest (urban site) and K-puszta (remote area). Two PIXE International 7-stage cascade impactors were used for aerosol sampling with 24 hours duration. These impactors separate the aerosol into 7 size ranges.

The elemental concentrations of the samples were obtained by proton-induced X-ray Emission (PIXE) analysis. Size distributions of S, Si, Ca, W, Zn, Pb and Fe elements were investigated in K-puszta and in Budapest. Average rates (shown in Table 1) of the elemental concentrations was calculated for each stage (in %) from the obtained distributions. The elements can be grouped into two parts on the basis of these data.

The majority of the particle containing Fe, Si, Ca, (Ti) are in the 2-8 μm size range (first group). These soil origin elements were found usually in higher concentration in Budapest than in K-puszta (Fig.1.). The second group consisted of S, Pb and (W). The majority of these elements was found in the 0.25-1 μm size range and was much higher in Budapest than in K-puszta. W was measured only in samples collected in Budapest. Zn has uniform distribution in Budapest and does not belong to the above mentioned groups.

Acknowledgements

This work was supported by the National Research and Development Program (NRDP 3/005/2001).

a) ELTE, Environ. Chem., Budapest, Hungary

Table 1. Average rate of the elemental concentration for each stage in %.

Stage	Size	Fe		S		Si		Ca		Zn		Pb		W	
	[μm]	K-p	Bp	K-p	Bp	K-p	Bp	K-p	Bp	K-p	Bp	K-p	Bp	K-p	Bp
1	0.25-0.5	4.6	4.4	**45.6**	**62.2**	3.7	2.2	0.5	0.9	14.5	***19.6***	**26.2**	**43.1**	-	**37.3**
2	0.5-1.0	12.5	5.6	**32.3**	**20.9**	8.3	4.8	2.2	1.8	**28.8**	***14.7***	**40.8**	**16.2**	-	**12.0**
3	1.0-2.0	**24.3**	16.6	12.1	5.4	**28.6**	12.9	22.3	9.3	**25.4**	***19.4***	16.7	14.2	-	11.2
4	2.0-4.0	**30.2**	**35.2**	3.7	4.8	**24.0**	**30.5**	**36.9**	**32.0**	15.8	***18.0***	7.5	9.2	-	13.9
5	4.0-8.0	**21.6**	**31.3**	2.8	5.2	**19.5**	**36.1**	**34.9**	**43.0**	10.1	***18.4***	4.7	10.5	-	10.8
6	8.0-16	3.3	6.4	1.6	1.4	8.0	11.2	1.7	12.5	3.0	8.3	0.8	4.4	-	8.4
7	>16	3.6	0.5	1.8	0.1	7.9	2.4	1.6	0.6	2.5	1.7	3.3	2.4	-	6.3

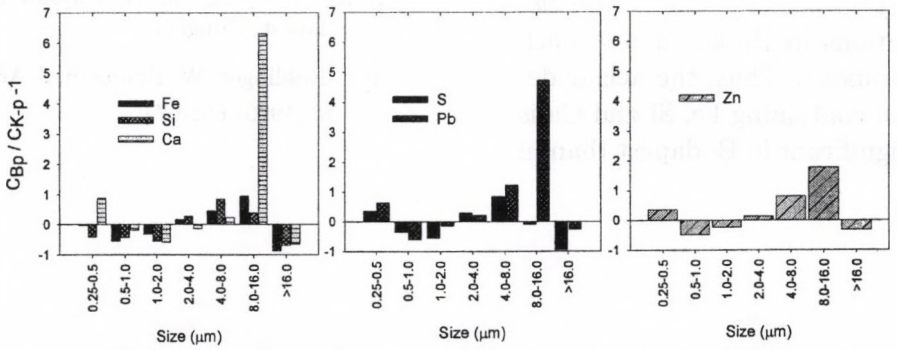

Figure 1. Comparison of average concentrations of Fe, Si, Ca, S, Pb and Zn in the seven size fractions measured in Budapest (CBp) and K-puszta (CK-p) from 24 July to 1 August 2003.

5.11 Atmospheric aerosol sampling campaign in Budapest and K-puszta: Part II. Application of Stochastic Lung Model

E. Dobos, I. Borbély-Kiss, Zs. Kertész, I. Balásházy[a)]

The Stochastic Lung Model [1] is a new important tool for the investigation of the health impact of atmospheric aerosols. The obtained concentrations of urban and rural aerosols (see part I.) were applied for lung deposition calculations with this model.

The health effects of the inhaled particles may strongly depend on the location of deposition within the lung. This model was applied in order to calculate the deposition efficiencies of the measured aerosols in the tracheobronchial and the acinar regions of human respiratory system. In the acinar regions takes place the gas-exchange. In this model a lot of parameters can be adjusted and changed. For example: tidal volume, aerosol diameter and density, time of breathing cycle, etc. So can be calculation some cases among others males, females or children, sleep, sitting, light or heavy exercise, etc.

As example the Figure 1. demonstrates that the acinar deposition has a maximum at 1-3 μm aerosol size and above 10 μm the practically do not reach the acinar region at sitting breathing conditions for male person.

In the part I. the elements have been grouped. The first group was composed of Fe, Si and Ca. These elements can be found in 2-8 m size range with the largest rate. The deposition of Fe, Si and Ca elements has the largest probability in acinar region. The elemental concentrations in Budapest are much larger than in K-puszta. Thus, the acinar deposition of aerosol containing Fe, Si and Ca is relatively more significant in Budapest than in K-puszta.

The second group was composed of S, Pb and W. The majority of these elements was in the 0,25-1 μm size range. These elements also deposit in acinar region but with less probability. Because their particles have large concentration they can also deposit in large amount.

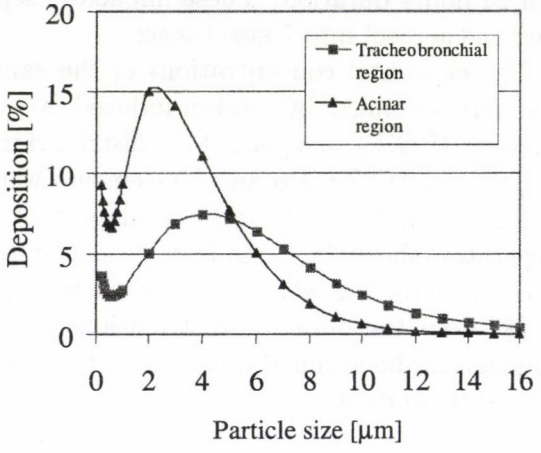

Figure 1. Deposition probabilities of the measured aerosols in the tracheo-bronchial and acinar regions

Acknowledgements

This work was supported by the National Research and Development Program (NRDP 3/005/2001).

a) KFKI AERI, Health Physics Department, Budapest, Hungary

[1] L. Koblinger, W. Hofmann, J. Aerosol Science, 21, 5, (1990) 661-674

6.1 The study of methanol transformation over Cu-modified ZSM-5, Beta zeolite and MCM-41 mesoporous silica using ^{11}C-radioisotope labeling

É. Sarkadi-Pribóczki, N. Kumar[a)], T. Salmi[a)], D.Yu. Murzin[a)], Z. Kovács

The copper-containing zeolites and mesoporous silica, among other metals, are suitable for dehydrogenation of methanol. The Cu transition metal determines the route of methanol conversion on supports of ZSM-5 and Beta zeolite as well as MCM-41 mesoporous silica. The catalysis mechanism and the catalytic property are concluded from the composition of methanol derivates over Cu-modified catalysts.

The Cu ion-exchanged ZSM-5 and Beta zeolite and MCM-41 mesoporous silica were synthesized and characterized using X-ray power diffraction, scanning electron microscope, nitrogen and pyridine adsorption, X-ray fluorescency and FTIR spectroscopy.

The ^{11}C-radioactive labeling method (^{11}C radioisotope, $T_{1/2} = 20$ min, is a gamma emitter by annihilation of its positron) is suitable for following the process of ^{11}C-methanol conversion i.e. adsorption, desorption and catalytic transformation as well as for investigation of small amounts of molecules over catalysts by very sensitive radioactivity detectors.The ^{11}C radioisotope was produced at cyclotron and the ^{11}C-methanol was synthesized by a classical radiochemical method. After catalysis the ^{11}C-radioactive and non radioactive volatile products were identified by radiogas chromatography hereby radiolabeled compound and -derivates were distinguished from other participant natural, nonradioactive carbon compounds.

Along radioactive products dimethyl ether and small hydrocarbons products were formed by Brønsted acid sites of catalysts while formaldehyde and small methyl formate were formed by Cu metal over bifunctional Cu-ZSM-5, Cu-Beta zeolite and mesoporous Cu-MCM-41 silica at 240 °C. The detection of methoxy methanol and dimethoxy methane confirmed the simultaneous presence of acid and basic sites of catalysts. At higher temperature (400 °C) the CO and CO_2 final products were dominated.

In our previous works, methanol conversion to hydrocarbons was observed by dehydration over acid H-formed ZSM-5, Beta and MCM-41. The methanol transformation to dimethoxymethane and dimethyl ether was resulted by dehydrogenation and dehydration simultaneously over Cs-formed ZSM-5, Beta and MCM-41 catalysts. The methanol conversion over Cu-formed ZSM-5, Beta and MCM-41 catalysts gives a new information for clearing of the roles of H, Cs as alkali metal and Cu as transition metal in ZSM-5, Beta and MCM-41 supports.

The acid-basic properties of the supports and the oxidation state and dispersion of copper was investigated effectively by methanol conversion using ^{11}C-radioactive labeling.

Acknowledgements

This work was financially supported by the Hungarian Scientific Research Fund No. T031764.

6.2 Calcium deposits in the common carotid artery

Z. Szikszai, Zs. Kertész, I. Uzonyi, G.Á. Szíki, M.T. Magyar[a)], S. Molnár[a)], Y. Ida[b)], L. Csiba[a)]

Arterial calcification consists mainly of calcium apatite and takes place at two sites in the vessel wall: the intima and the media. Intimal calcification occurs exclusively within atherosclerotic plaques, while medial calcification may develop independently [1]. Ultrasound examination of the carotid arteries is performed routinely to assess pathological alterations. Large calcified plaques in the carotid arteries can be detected by B-mode ultrasonography easily as high frequency ultrasound does not penetrate calcium and have been investigated extensively. In this study our aim was to determine the calcium distribution in the vessel wall itself, excluding large plaques, and to make the first step towards investigating the relationship between the calcium distributional maps and the respective ultrasonic images.

The carotid arteries of five elderly (age 71±9 years) and one young (age 27 years) deceased patients were excised at autopsy and were investigated with a medical ultrasound equipment in a tank containing saline solution. Scan sequences were videotaped and images of previously marked cross-sections were transferred to a computer. Small pieces of the arteries were cut and quench frozen. Sections of 60μm from the middle of the scanned segments (30mm proximal to the bifurcation) were cut in a cryostat. The cryosections were transferred to microprobe target holders. The elemental distribution of the samples were determined by particle induced X-ray emission (PIXE) at the Debrecen microprobe [2]. True elemental maps and absolute concentration values were evaluated with a new software (True Pixe Imaging) [3].

The average calcium content of the scanned areas varied between 1000 and 9000μg/g in the slices of the common carotid arteries of the elderly patients. In contrast, scanned areas in the slices from the young subject contained only 600-800μg/g calcium. The concentration of calcium could reach even 3.75% along the wide and long arcs in the medial layer of the carotid arteries in the elderly patients. Note, that the calcium content of bone varies around 15%. However, at this stage of the study no firm conclusion can be drawn concerning the relationship between the elemental maps and the ultrasonic images. An improved *in vitro* ultrasound setup and better image quality are required to clarify the potential in the ultrasound imaging to provide sensitive calcification assessment.

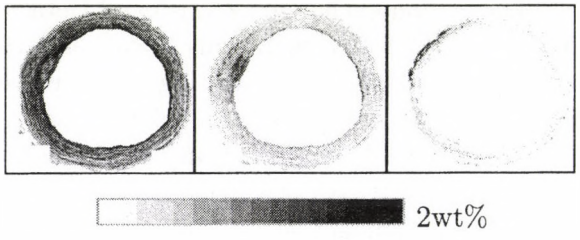

Figure 1. S, P and Ca distributional maps of a complete cut. The pictures are composed of 21 scans (1.25×1.25 mm^2 each). Sulphur distribution provides information about the extension of the sample and helps to identify atherosclerotic inclusions in the intima. Phosphorus is a component of calcium apatite. Lipids are also rich in P. This sample contains a not-calcified atheroslerotic lesion in the intima and a long calcified arc in the media.

Acknowledgements

Grants from the Hungarian Research Foundation (OTKA A080, M041939) as well as from the Health Science Council of the Ministry of Health of Hungary (ETT 122/2003) are gratefully acknowledged.

a) Dept. of Neurology, University of Debrecen, H-4012 Debrecen, PO Box 24, Hungary

b) Fukuoka Memorial Hospital, 1-1-35, Nishijin, Sawara-ku, Fukuoka, 814-8525, Japan

[1] D. Proudfoot, C.M. Shanahan, Herz 26 (2001) 245.

[2] I. Rajta, I. Borbély-Kiss, Gy. Mórik, L. Bartha, E. Koltay, Á.Z. Kiss, NIMB 109-110 (1996) 148.

[3] I. Uzonyi, Gy. Szabó, NIMB, accepted for publication

6.3 Nuclear microprobe study of TiO_2-penetration in the epidermis of human skin xenografts

Zs. Kertész, Z. Szikszai, E. Gontier[a,b], P. Moretto[a], J.-E. Surlève-Bazeille[b], B. Kiss[c], I. Juhász[c], J. Hunyadi[c], and Á.Z. Kiss

Titanium-dioxide is a widely used physical photoprotective component of various cosmetic products. However, very few experiments have been carried out on its penetration through the human epidermal barrier and its possible biological effects in vivo and in vitro.

In the frame of the NANODERM EU5 project, the penetration of TiO_2-nanoparticles through the epidermis of human foreskin grafts transplanted into SCID (Severe Combined Immune Deficiency) mice was investigated in the nuclear microprobe laboratories of Debrecen and Bordeaux. Transmission electron microscope studies of the same samples were also carried out in the DMPFCS laboratory.

The skin grafts were treated with a hydrophobic emulsion (Anthelios XL F60) containing micronised TiO_2-nanoparticles in occlusion, for 1, 24 and 48 hours time periods. Quantitative elemental concentrations and distributions have been determined in 14-16 μm thick freeze-dried sections obtained from quick frozen punch biopsies using PIXE (Particle Induced X-ray Emission), STIM (Scanning Transmission Ion Microscopy) and RBS (Rutherford Backscattering) analytical methods.

The different layers of the epidermis can be well identified on the STIM energy maps and on the obtained elemental maps since the different cell layers can be characterized with different elemental composition. The outermost layer, the stratum corneum, which consists of the remains of dead keratinocytes, is characterised by high amount of S and Cl. The vital layers contain phosphorus in high concentration.

In most cases it was found that the remnant of the liposome crčme together with the outermost stratum corneum was removed during the sample preparation. When the crčme remained on the skin the Ti was quasi homogeneously distributed in the outermost layers, and the penetration seemed to be limited to the outermost part of the stratum corneum.

However, in two cases, both after 48 h exposure, penetration through the stratum corneum to the limit of the vital stratum granulosum was observed, as shown in figure 1. The sample originates from the entry of a sweat gland.

With both ion microscopy and electron microscopy we have observed nanoparticles down to the innermost corneocyte layers, nevertheless no particle was observed in the cytoplasm of the granular cells so far.

The further goal is to investigate the existence of other routes of penetration, e.g. though hair follicles, sebaceous or sweat glands.

Acknowledgements

This work was supported by the 5FP project NANODERM QLK4-CT-2002-02678.

a) Centre d`Etudes Nucléaires de Bordeaux-Gradignan, France

b) Laboratoire DMPFCS, Université Bordeaux

b) Dept. of Dermatology, Univ. of Debrecen

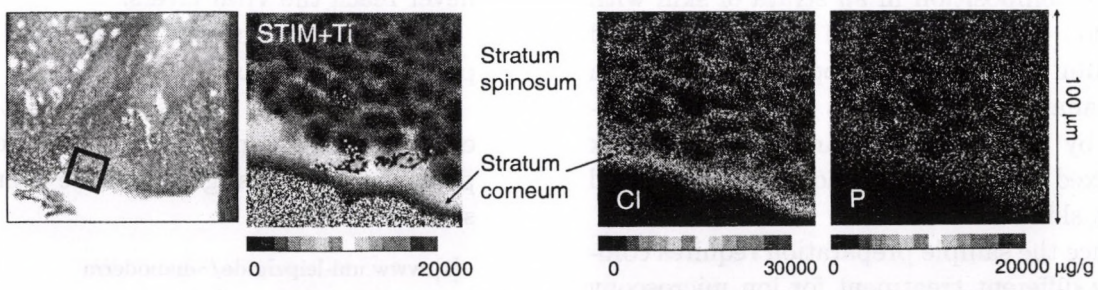

Figure 1. Optical image of the sample and its surrounding, STIM image and true elemental maps.

6.4 Quality of skin as a barrier to ultra-fine particles

Contribution of the IBA group to the NANODERM EU-5 project in 2003-2004

Zs. Kertész, Z. Szikszai, and Á.Z. Kiss

Micronised titanium-, zinc- or silicon-oxide is a widely used physical photoprotective agent as a component of various cosmetic products. Due to the small particle size (down to 15 nm) it is supposed, that the particles may pass through the uppermost horny skin layer, and penetrate into deeper vital skin layers. However, only a few experiments have been carried out on its penetration through the human epidermal barrier and its possible biological effects *in vivo* and *in vitro*, using the tape stripping method which has no lateral and limited depth resolution.

A consortium consisting of 12 European universities and scientific institutes has been established under the leadership of the Fakultät für Physik und Geowissenchaft Universität Leipzig, whose goal is to get quantitative information on the penetration of ultrafine particles in all strata of skin, on their penetration pathways as well as on their impact on human health [1]. The IBA group of the Atomki takes part in this project as a subcontractor of the Department of Dermatology, University of Debrecen, Hungary.

Ion microscopy, electron microscopy and autoradiography are used to trace the penetration of the nanoparticles into the skin layers, molecular and cell-biological methods are applied to assess the skin response and activation of dermal cells.

The IBA group of the Atomki takes part in WP3: Ion Microscopy Work Package together with five other nuclear microprobe laboratories. The participants provide quantitative elemental composition in all strata of skin with detection limits of about 1 μg/g and lateral resolution of 1-2 μm by applying various ion beam analytical techniques. Samples investigated by ion microscopy are 14-16 μm thick cryo-fixed freeze-dried sections of porcine and human skin.

Since the sample preparation requires completely different treatment for ion microscopy than for conventional microscopy, the members of the IBA group, who already have experience in this field, take part in the sample preparation work of WP2 at the Department of Dermatology, Univ. Debrecen.

In order to provide quantitative elemental concentrations and distributions a new measurement setup and data evaluation system has been developed at the Debrecen nuclear microprobe facility [2].

All the participating laboratories took part in an intercomparison study in order to demonstrate, that the results obtained using different facilities and different analytical techniques are consistent and reliable. The result of the analysis of two gelatin "standard" samples showed a fairly good agreement between the six groups (17% and 20% SD from the mean value).

The penetration studies using different formulations were started on domestic pig skin, which resembles human skin closest. As a next step, human skin xenografts transplanted into SCID mice were applied. This murine model was developed in the Department of Dermatology of the University of Debrecen because of the difficulties to obtain human skin biopsies from healthy volunteers. Experiments on healthy human skin provided by the Lisbon group started at the end of 2004.

In 2004 22 pig skin, 11 transplanted human skin and 13 human skin samples were investigated in Debrecen.

The results obtained by ion microscopy or electron microscopy shows that in the case of healthy skin the nanoparticles penetrate into the deepest corneocyte layer of the skin, but never reach the vital layers.

Further experiments are planned with repeated exposure and on atopic skin.

On the bases of the results obtained by electron microscopy and ion microscopy, cell physiological investigations have been already started.

[1] www.uni-leipzig.de/~nanoderm

[2] Zs. Kertész et al. accepted for publ. in NIM B

7.1 Status Report on Cyclotron Operation

P. Kovács, I. Szűcs, I. Ander, T. Lakatos, F. Tárkányi

The operation of the cyclotron in 2004 was concentrated to the usual 9 months; January, July and August were reserved for maintenance and holidays. The overall working time of the accelerator was 3554 hours, the time used for systematic maintenance was 450 hours. The breakdown periods amounted to 70 hours last year, included in it a 50 hours repair of RF control module under garantee. The cyclotron was available for users during 3034 hours. The effectively used beam-on-target time statistics is summarized in Table 1.

Table 1. Statistics of the irradiation time (beam-on-target) for different research groups

Projects	**Hours**	**%**
Nuclear spectroscopy	269	24.8
Nuclear astrophysics	176	16.2
Nuclear reaction data	157	14.4
Medical isotope production	280	25.8
Radiation tolerance tests	79	7.3
This layer activation (TLA)	125	11.5
Total	**1086**	**100**

Notes to Table 1:

- The users were the same as in 2003.
- 55.4 % of the accelerator time was used for basic science and 44.6 % for applications.
- The weight of medical isotope production decreased due to the start of the operation of the new cyclotron of the PET Centre of the University of Debrecen.

Developments

- A new measuring site with a HPGe detector based gamma spectrometer is under installation in the basement of the Cyclotron Laboratory.
- A two channel pneumatic rabbit system is also under development to enable fast transport of samples between the new measuring site and two irradiation sites (the low intensity fast neutron irradiation site and the beam line used for Thin Layer Activation).

7.2 Activities at the Van de Graaff Accelerator Laboratory

L. Bartha

During 2004 the beam time of the VdG-1 machine amounted to 66 hours. The accelerator delivered helium beam used for low energy atomic physics experiments. The beam time of the hollow cathode ion source - which is also operated on the beam transport of VdG-1 accelerator - is excluded.

The 5 MV Van de Graaff machine was operating for 2247 hours during this period. Proton (64.97 %), H_2^+ (2.50 %), D^+ (2.50 %), $^3He^+$ (21.91 %) $^4He^+$ (5.58 %) and $^{14}N^+$ (2.54 %) particles were accelerated.

The beam time was distributed among different research subjects as shown in Table 1.

Table 1. Time distribution among different research activities at VdG-5

Field	**Sign**	**Hours**	**%**
Atomic physics	AP	278	12.37
Nuclear physics	NP	483	21.50
Nuclear astrophysics	NAP	211	9.39
Analytical studies	IBA	984	43.79
Micromachining	MM	248	11.04
Machine tests	MT	43	1.91
Total		**2247**	**100**

The installation of the 4130A Tandetron AMS made by General Ionex Corporation has been continued in this year.

7.3 SNMS/SIMS – a new surface analytical device in ATOMKI

Z. Berényi, K. Vad, G.L. Katona, Á. Kövér, G.A. Langer[a)], D.L. Beke[a)], A. Hüpfer[b)]

A Secondary Neutral Mass Spectrometer (SNMS) was installed in the institute in 2004. The aim of the investment was to complement the surface analytical methods of the Section of Electron Spectroscopy and Materials Sciences of ATOMKI (eg. preparation, characterization and depth profiling of thin layer and thin multilayer samples) as well as to establish a new surface analytical technique in the institute to be offered for other internal and external users. This equipment is the first SNMS apparatus in Hungary.

The device is capable to measure the elemental composition of the surface region (i.e. the topmost 1 μm) of conductor, semiconductor and insulator surfaces with a unique in-depth resolution of some nanometers. As an example figure 1. shows a measured depth profile of a Ru-Co multilayer sample, consisting of 25 bilayers of Co(3nm)-Ru(3nm) sandwiched between two Ru(10nm) layers on the top of a Si substrate. This SNMS method is based on the mass spectrometry of the neutral particles of the analyzed material removed by ion bombardment and ionized in a radio-frequency plasma generated above the sample.

In addition to the SNMS method the apparatus is equipped with a Specs IQE 12/38 scanning ion gun and offers the application of elemental mapping of surface layers using Secondary Ion Mass Spectrometry (SIMS) technique with moderate lateral resolution ($\sim$ 120 μm), as well.

Application for financial support was submitted to the R&D Programme of the Ministry of Education of Hungary together with the Department of Solid State Physics of the University of Debrecen. Besides the 59.5 MFt supported by the programme a significant contribution of 25.5 MFt from the two applying institutes had to be made.

The device was purchased in accordance with the public procurement procedure. Out of the three candidates answering the call for the tender the one submitted by Specs GmbH offering their Specs-INA device was the most appropriate to meet our needs and financial potentials. The installation and users training started in the beginning of June and the official handover was made in November 24, 2004.

During the time of installation all main features and capabilities listed in the technical specifications of the apparatus were successfully demonstrated. Minor electrical and mechanical errors were corrected and tested together with the technical expert of the manufacturer. Some requirements of further development of the technical features were stated in the final report of the installation.

Test measurements introducing various multilayer samples and composition calibration samples have been going on since the installation and to be continued in the year of 2005. We are open for competent and fruitful applications and partners in order to exploit the potentials of the new apparatus as much as possible.

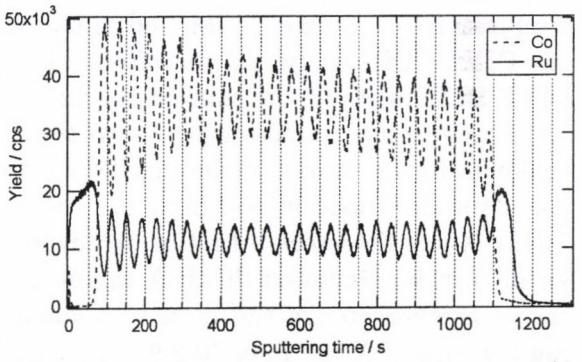

Figure 1. Measured SNMS depth profile of Ru-Co multilayer sample

a) Dept. of Solid State Physics, Univ. of Debrecen

b) Specs GmbH, Berlin

7.4 The bio-PIXE setup on the Debrecen scanning proton microprobe

Zs. Kertész, Z. Szikszai, I. Uzonyi, A. Simon and Á.Z. Kiss

Besides the ongoing applications in archeometry, geology, material science and atmospheric aerosol study, in recent years the IBA Group in Debrecen has joined several biological and biomedical research projects. Such studies require the knowledge of accurate quantitative elemental concentrations and distributions in organic, inhomogeneous thin samples on a microscopic scale.

In most cases, to carry out quantitative investigations on biomedical samples down to the cell level, the combination of proton induced X-ray emission (PIXE), Rutherford backscattering (RBS) spectrometry and scanning transmission ion microscopy (STIM) analytical methods are used simultaneously. STIM provides information on the density and structure of the sample, PIXE measures the concentration of the inorganic major and trace elements, and finally RBS serves to characterize the organic matrix, to determine the beam dose, and sometimes the sample thickness. The drawback of this combined method is that to evaluate the RBS data the hydrogen to carbon ratio in the sample must be known.

The setup developed at the Debrecen microprobe facility [1] is based on the combined application of on-axis STIM and simultaneous PIXE-PIXE analytical techniques. In the PIXE-PIXE method the sample matrix is determined directly by measuring X-rays from all elements in the sample including the light elements such as carbon and oxygen, using two Si(Li) X-ray detectors. In this arrangement an ultra thin windowed Si(Li) X-ray detector serves to characterize the matrix by measuring low energy X-ray lines (0.2-9 keV) while a large area Be-windowed detector is used to detect the medium and high energy X-ray lines (>4 keV). In this way elements with atomic number higher than 5 can be detected simultaneously, reducing both radiation damage of the sample and measurement time. In addition, the knowledge of the hydrogen content of the sample is not needed, since it influences the concentration values of the inorganic trace elements in negligible extent.

The beam current is measured by a compact beam chopper.

The morphology and area density of the samples are determined by analyzing STIM spectra and maps. Different detectors and geometries were tested and finally the application of a surface barrier detector in on-axis geometry was found to be optimal [2].

For cross-checking the validation of the obtained data, in a few cases RBS technique was applied simultaneously to determine the thickness of the sample, the concentration of the matrix elements, and to control the reliability of the beam current measured by the chopper.

Signals from all detectors are recorded event by event in list mode. The extraction of pixel information and the imaging is done with a new software package developed for true elemental mapping [3]. The new computer code, based on the upgraded PIXEKLM program, generates off-line quantitative true elemental maps and calculates absolute concentration values considering the varying thickness of the sample.

The newly developed bio-PIXE setup proved to be a powerful tool in the analysis of biological samples, and has been successfully applied for studying the penetration and clearance of ultra-fine particles containing heavy metals of physical bodycare cosmetics in the different layers of skin within the frame of the NANODERM EU5 project, and for the investigation of calcium distribution in carotid arteries.

Acknowledgements

This work was supported by the 5FP projects NAS-MICRO-XRF and NANODERM as well as the Hungarian Research Foundation under contracts Nos. A080, M041939, M36324.

[1] Zs. Kertész et al, accepted for publ. in NIM B

[2] P. Aguer et al, accepted for publ. in NIM B

[3] I. Uzonyi, Gy. Szabó, acc. for publ. in NIM B

7.5 Optimisation of particle fluence in micromachining of CR-39

I. Rajta, E. Baradács[a)], A.A. Bettiol[b)], I. Csige, K. Tőkési, L. Budai, Á.Z. Kiss

Polyallyl diglycol carbonate (PADC, also known as CR-39 etched track detector) material was irradiated with various doses of 2 MeV protons and alpha-particles in order to optimise the fluence for P-beam writing of CR-39 [1]. Irradiation were performed at Atomki and at the National University of Singapore.

Post irradiation work has been carried out in Debrecen. The samples were etched in 6.25N NaOH solution at 70 °C. Etching was interrupted at every 5 seconds for monitoring the process of the 3D structure development by optical microscopy observations. The fluence in the irradiated area was sufficiently high that the latent tracks overlapped and the region could be removed collectively by short etching times of the order of less than one minute.

Theoretical calculations based on analytical and Monte Carlo simulations were performed in order to calculate the probability of multiple latent track overlap. Optimal particle fluence was found by minimising the fluence and etching time at which collective removal of latent tracks could be observed.

We have found that the optimum etching time for proton irradiated PADC samples is 60 s. At this etching time the damaged region exposed to the highest fluences were collectively removed, while the ones exposed to the lowest fluences were still not removed at all. Etching times shorter than about 1 minute are difficult manage accurately. In the applied range of particle fluences we found the optimum fluence for the given etching conditions by analysing the geometrical properties of the etched structures by optical microscopic observations.

Using this method both the Singapore and Debrecen samples gave 600 nC/mm^2 charge density as the best fluence for 2 MeV protons. The optimal fluence for alpha particles was found at 60 nC/mm^2. The irradiated region of the samples was collectively removed and there was a smooth bottom at the end of the latent ion tracks. At lower fluences the removal was not complete, and at higher fluences the bottom of the removed pit had an uneven surface. At the highest applied fluences we observed sample melting. In some cases not only the irradiated but a spherical shape drop-like portion on the bottom side of the irradiated region have been melted, which was removed by etching collectively with the irradiated region.

We concluded that the CR-39 etched track detector can be also used as a resist material for P-beam writing both for proton and alpha irradiation. If one needs very shallow micromachined structures in positive resist, alpha-particle irradiation of CR-39 is a nice solution: it does not need much fluence, and it is more resistant to unwanted damage.

Acknowledgements

This project was supported by the Hungarian National Research Foundation OTKA (A080, M41939, M36324 and F42474). I. Rajta and K. Tőkési are grantees of the Bolyai János Scholarship.

a) Univ. of Debrecen, Dept. of Environmental Physics

b) National University of Singapore, Department of Physics, Centre of Ion Beam Applications

[1] I. Rajta et al, accepted for publication in NIM B.

7.6 PMMA melting under proton beam exposure

S.Z. Szilasi, E. Baradács[a)], I. Daruka[b)], P. Raics[c)], C. Cserháti[d)], E. Dobos and I. Rajta

PMMA (polymethylmethacrylate) is one of the most commonly used resist material in Proton Beam Micromachining. The aim of this work was the systematic investigation of the melting of PMMA, thus one may design the parameters of an experiment to avoid unwanted melting.

Numerical finite difference calculations including conductive heat transport, heat radiation and the fluence dependence of the polymer's melting temperature were implemented to model the melting process of thin irradiated polymer films.

Various irradiations have been performed at different beam fluence rates and different fluences. The irradiations have been performed on the PIXE beamline of the homemade 5 MV Van de Graaff accelerator of ATOMKI. The beam current was varied between 1-50 nA, and the collected charge was up to 5500 nC.

Differential Interference Contrast microscopy showed that the original surface of the samples was slightly rough, and the high-fluence samples had smooth surface where the beam hit them. Low-fluence samples did not change, i.e. they still had the original rough surface. Twyman-Green interferometry showed the same results, i.e. the same samples proved to have been melted. Moreover, refraction index change was observed with the interferometry method. This way we could also conclude which samples received sufficient charge to consider them micromachined.

Interferometry pictures and a phase diagram (i.e. the fluence vs. beam density) are shown on Fig. 1. The samples are labelled as: × - underexposed, □ - refractive index changed, ○ - partly melted, • - completely melted. The solid curve shows the results of our numerical calculations, the critical fluence above which the samples melt as a function of the beam density. The horizontal dashed line at 100 nC/mm^2 indicates the typical fluence for PMMA micromachining.

It was found experimentally that the samples melt if the fluence exceeds a beam intensity dependent value. The model calculations are in good agreement with the experimental results.

Acknowledgements

This project was supported by the Hungarian National Research Foundation OTKA (A080, M41939, M36324, T37212 and F42474). C. Cserháti, I. Daruka and I. Rajta are grantees of the Bolyai János Scholarship; P. Raics has a Széchenyi István professorship.

a) Univ. of Debrecen, Dept. of Environmental Physics

b) Univ. of Debrecen, Dept. of Theoretical Physics

c) Univ. of Debrecen, Inst. of Experimental Physics

d) Univ. of Debrecen, Dept. of Solid State Physics

[1] S.Z. Szilasi et al, accepted for publ. in NIM B.

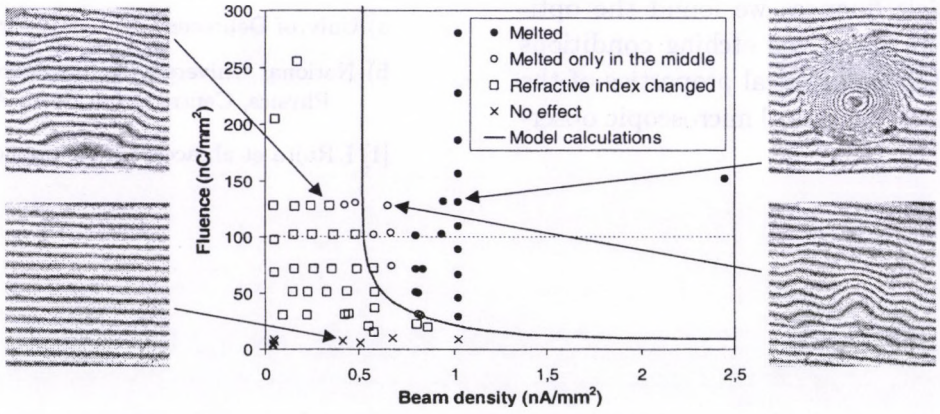

Figure 1. Interferometry pictures and a phase diagram (i.e. the fluence vs. beam density).

7.7 Proton beam micromachining on strippable aqueous base developable negative resist

I. Rajta, E. Baradács[a)], M. Chatzichristidi[b)], E.S. Valamontes[c)], I. Uzonyi, I. Raptis[b)]

Proton Beam Micromachining (PBM, also known as P-beam writing), a novel direct-write process for the production of 3D microstructures, can be used to make multilevel structures in a single layer of resist by varying the ion energy. The interaction between the bombarding ions and the target material is mainly ionization, and very few ions suffer high angle nuclear collisions, therefore structures made with PBM have smooth near vertical side walls.

The most commony applied resists in PBM are the positive, conventional, polymethyl methacrylate (PMMA); and the negative, chemically amplified, SU-8 (Micro Chem Corp). SU-8 is an epoxy based resist suitable also for LIGA and UV-LIGA processes, it offers good sensitivity, good process latitude, very high aspect ratio and therefore it dominates in the high aspect ratio micromachining applications.

SU-8 requires 30 nC/mm^2 fluence for PBM irradiations at 2 MeV protons. Its crosslinking chemistry is based on the eight epoxy rings in the polymer chain, which provide a very dense three dimensional network in the presence of suitably activated photo acid generators (PAGs) which is very difficult to be stripped away after development. Thus, stripping has to be assisted with plasma processes or with special liquid removers. Moreover, the SU-8 developer is organic, propylene glycol methyl ether acetate (PGMEA), and thus environmentally non-friendly.

To overcome the SU-8 stripping limitations, design of a negative resist system where solubility change is not based solely on crosslinking but also on the differentiation of hydrophilicity between exposed and non-exposed areas is desirable. A new resist formulation, fulfilling the above specifications has been developed recently [1]. This formulation is based on a specific grade epoxy novolac (EP) polymer, a partially hydrogenated poly-4-hydroxy styrene (PHS) polymer, and an onium salt as photoacid generator (PAG), and has been successfully applied for UV-LIGA. This epoxy resist is aqueous base developable (IC standard aqueous developers (tetramethyl ammonium hydroxide TMAH 0.26N)) and presents limited or no swelling and reduced roughness problems compared to the pure epoxy novolac resists.

In order to test these novel resist materials in the PBM technique, irradiations have been performed on the nuclear microprobe facility at ATOMKI, Debrecen, Hungary. The proton energy was 2 MeV. Beam currents of 5-60 pA were focused down to 2-3 μm spotsize. The scan size was typically 1 mm.

The tested formulations in the present work need about 120-240 nC/mm^2 fluence. This is higher than that of the SU-8, but these new formulations have the advantage of using IC industry developer solutions and easy stripping in acetone.

The resist formulation consisted of polymer mix of 78% (w/w) PHS with 12% degree of hydrogenation and 22% (w/w) EP and 1-(4-hydroxy-3-methylphenyl) tetrahydrothiophenium triflate (o-CS-triflate) 3% (w/w) as PAG provided the best patterning results. Using this formulation 5-8 μm wide lines with aspect ratio 4-6 were resolved [2].

Acknowledgements

This project was supported by the Hungarian National Research Foundation OTKA (A080, M41939, M36324 and F42474), the Hungarian TéT (Greek-Hungarian Bilaretal Project GR-3/03) and the Greek General Secretariat for R&D (Greek-Hungarian Bilaretal Project). I. Rajta is a grantee of the Bolyai János Scholarship.

a) Univ. of Debrecen, Dept. of Environmental Physics

b) IMEL, NCSR-Demokritos, Greece

c) Dept. of Electronics, TEI Athens, Greece

[1] M. Chatzichristidi, Microelectr. Eng. 61(2002)729.

[2] I. Rajta et al, accepted for publ. in NIM B.

7.8 PIXEKLM-TPI – a software package for quantitative elemental imaging with nuclear microprobe

I. Uzonyi and Gy. Szabó

Production of true elemental images using PIXE and the scanning nuclear microprobe is a complex and still challenging problem. Ryan and his co-workers were the first who developed a software package (GeoPIXE) for quantitative mapping, which was the only available in this field [1]. It is based on a rapid matrix transform method called Dynamic Analysis which directly converts the spectrum vector (S) into the concentration vector (C) in terms of the matrix Γ: $C = Q^{-1}\Gamma S$ (Q is the accumulated charge). This linear equation system allows to produce true elemental images $M_k(x, y)$ by incrementing each image k (at beam position x, y) by Γ_{ki} ki for each event at channel i.

Based on our Oxford-type scanning nuclear microprobe facility we realized a special μPIXE set-up consisting of an ultra thin windowed (UTW) and a Be windowed Si(Li) X-ray detectors a few years ago. Then with the modification of our PIXEKLM program package we solved the efficiency calibration of UTW detectors and quantitative analysis down to C-K_α line by PIXE.

In this report we present our new method and software package (PIXEKLM-TPI) developed for true elemental imaging [2]. The method is based on the above-mentioned ideas and measuring system. The software allows off-line data processing from list mode files. The Γ matrix is calculated by the PIXEKLM program package for any sample composition and thickness from C to U for K, L and M characteristic X-ray lines. True elemental images are produced by a frame program called True PIXE Imaging (TPI). It allows advanced image processing and multivariate statistical analysis in order to help the interpretation and presentation of concentration data.

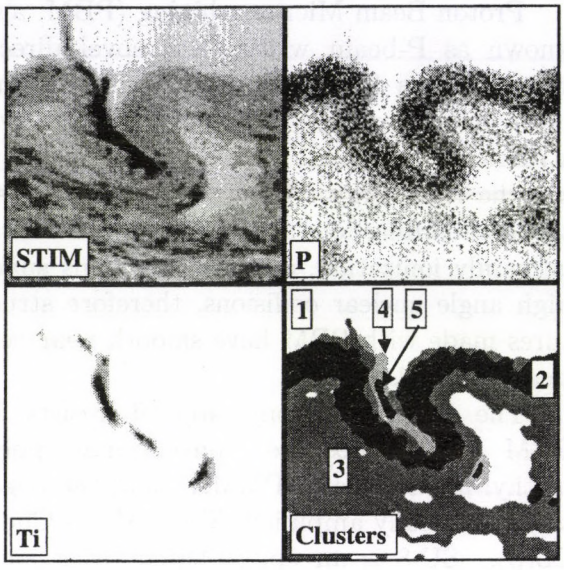

Figure 1. Application of the PIXEKLM-TPI program package in the field of biology. The figure shows a STIM image, selected true elemental images (P, Ti) and a cluster map of a thin skin section around a hair follicle (scan size=250×250 μm^2, high concentration/thick sample is shown black, Q=1 μC). The sample was treated by TiO_2 rich physical body care cosmetics [3]. From (all) TEI-s the sample was decomposed into five clusters: "1": stratum corneum (plus thin tissue); "2": stratum spinosum, enriched in P (and K); "3": dermis; "4" and "5": hair follicle with medium and high Ti content.

Acknowledgements

Support from the 5FP projects NAS-MICRO-XRF and NANODERM (Contract Nos. G4RDCT-2000-00402 and QLK4-CT-2002-02678) is gratefully acknowledged.

[1] C.G. Ryan, D.N. Jamieson, Nucl. Instr. and Meth. B 77 (1993) 203.

[2] I. Uzonyi, Gy. Szabó, accepted for publication in Nucl. Instr and Meth. B.

[3] Zs. Kertész et al., accepted for publication in Nucl. Instr and Meth. B.

7.9 A new micro-DIGE set-up for the analysis of light elements

G.Á. Szíki, I. Uzonyi, E. Dobos, I. Rajta, K.T. Biró[a)], S. Nagy[b)], Á.Z. Kiss

A relatively simple and inexpensive way of converting the sample chamber of a conventional OM type microprobe into an easily useable micro-DIGE set-up was worked out at the Debrecen scanning nuclear microprobe facility [1]. The basic idea of this new set-up is to increase the image distance of the microprobe by moving the focus out of the sample chamber into an extension tube, which is connected to the 0° port of the chamber. This new position of the focus and so the sample, enables the use of different type of gamma-ray detectors in enlarged solid angles increasing the sensitivity of the technique. The increase in detection efficiency was a factor of nine at 1173 keV gamma-ray energy. The degradation of the lateral resolution of the system as a consequence of the increased image distance was theoretically and experimentally investigated. The measured geometric spot size (15×17 μm^2) was poorer than the one attainable with a conventional experimental arrangement. Considering the fact that in several cases, a μ-DIGE measurement is only possible with the new set-up, this price is often worth paying. Archaeological and ecological applications of the new set-up was also presented.

Acknowledgements

Support from the Hungarian Research Foundation (OTKA) under contract NOS. A 080, M 041939, M 36324 and partly T 032264 is gratefully acknowledged.

a) Hungarian National Museum, H-1088 Budapest, Múzeum krt. 14-16, Hungary

b) Department of Ecology, University of Debrecen, H-4010 Debrecen, Hungary

[1] G.Á. Szíki et al, NIM B 219-220 (2004) 508.

7.10 A PIN detector array for the determination of boron using nuclear reaction analysis at a nuclear microprobe

G.Á. Szíki, E. Dobos, Zs. Kertész, Z. Szikszai, I. Uzonyi, Á.Z. Kiss

A new micro-NRA set-up for boron analysis via α-particle detection from the $^{11}B(p,\alpha)^{8}Be$ nuclear reaction has been developed at the Debrecen scanning nuclear microprobe facility [1]. The set-up consists of four large area PIN silicon photodiodes in an optimised geometrical arrangement providing 1.87 sr solid angle. This solid angle is slightly larger than the ever reported values (1,63 sr) for annular surface barrier detectors, which detectors are conventionally used for charged particle detection. The new set-up was calibrated for boron with NIST type glass standards and also with a macusanite glass standard in the low concentration region. The calculated MDL value for boron was 5 μg/g for 1 μC accumulated charge in a glassy matrix. The capability of this set-up for precise concentration measurement was demonstrated via the analysis of geological obsidian samples with less than 160 μg/g boron content.

Acknowledgements

Support from the 5FP project NAS-MICRO-XRF (Contract No. G4RDCT-2000-00402) as well as the Hungarian Research Foundation (OTKA) under contract NOS. A 080, M 041939 and M 36324 are gratefully acknowledged.

[1] G.Á. Szíki et al, NIM B 219-220 (2004) 420.

7.11 Efficiency calibration of electron spectrometers by the help of standard spectrum

J. Tóth, I. Cserny, D. Varga, L. Kövér and K. Tőkési

For studying thin films and surface nanostructures quantitative analytical applications of electron spectroscopic techniques have a great importance. The most frequently used techniques are XPS, XAES and AES in quantitative surface electron spectroscopy. Applying these techniques changes in the detection efficiency vs. electron kinetic energy change the measured electron peak intensity ratios and in this way the neglect of the energy dependence of the spectrometer efficiency can influence surface atomic concentrations derived. The importance of the precise determination of the atomic concentrations is very crucial, especially in the determination of non-destructive depth profiles by the help of AR-XPS in which small changes in the relative concentrations can change dramatically the concentration depth profiles of a few nanometer depth ranges.

In the present study the REELS technique was used to determine the relative detection efficiency by the help of a standard spectrum measured on the surface of fine microcrystalline Cu specimen.

The experimental relative efficiency curves vs. electron kinetic energy were compared to the calculated efficiency curve .

The efficiency calibration is discussed from the point of view of quantitative XPS, AR-XPS, AES and from the point of view of IMFP determination by XPS.

Acknowledgements

The work was supported by the Hungarian National Science Foundation, OTKAT038016. For the Cu specimen and the standard spectrum the authors are indebted to the Surface Analysis Society of Japan, to Dr. Shigeo Tanuma and Professor Keisuke Goto (NIT).

Note: The paper was an oral presentation by J. Tóth at JVC-10 Conference (Chairman: Janez Setina), 28 Sep - 02 Oct 2004, Portoroz, Slovenia.

7.12 Iron-fullerene mixture plasma

S. Biri, E. Fekete, A. Kitagawa[a)], *M. Muramatsu*[a)]

In many laboratories new materials useful for nanotechnology and medical applications are searched and studied. In the ECR laboratory one of our future goals is to produce endohedral fullerene molecules (e.g $Fe@C_{60}$) in large quantity. If this comes true, it will be possible to make building blocks for nanoparts, an ultra-contrast medium of MRI, and a magnetic nano-particle for treatment of cancer.

For this experiment some modifications were carried out on the ATOMKI-ECRIS [1]. The waveguide of the 14.5 GHz microwave generator was divided in order to couple very low powers (1 watt or less) into the plasma. The C_{60} component of the plasma was produced by using a simple oven. Among known methods (oven, sputtering, electron bombardment, compounds containing Fe), we have chosen the evaporation of ferrocene [$Fe(C_5H_5)_2$] powder to introduce Fe atoms into the plasma. The ferrocene chamber was connected to one of the two gas feeding lines and the evaporation rate was controlled by needle valve. The extraction voltage had to be kept as low as 600V, because of the low mass-energy product of our bending magnet.

First we developed independently the rough working conditions for single-charged dense iron and fullerene plasmas. Then a clean fullerene plasma was made. The temperature of the oven was about 450°C. The bending magnet was set to the C_{60} peak (M=720) and about 50-100 nA intensity of single-charged fullerene peak was obtained. Then the magnet was set to the position of the searched $Fe@C_{60}$ or FeC_{60} peak (M=776) and the ferrocene valve was opened. A very difficult and long tuning followed. Finally we found a new large peak with higher mass than C_{60}.

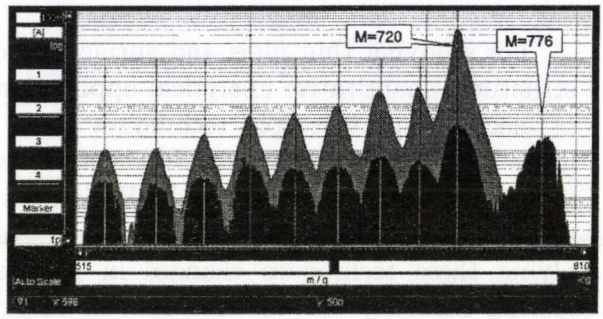

Figure 1. A typical C_{60}+Fe beam spectrum (red) together with an original (clean) C_{60} (grey) spectrum

In Figure 1 the centre of the new big peak on the right side is located at M=776 which corresponds to FeC_{60} and/or $Fe@C_{60}$ molecules. The peak is wide and shows some structure. We think it may contain impurities attached to the C_{58}, C_{59}, C_{60} and FeC_{60} molecules. We can not tell at this moment whether the iron atoms are inside or outside the carbon cage.

As a conclusion our experiment demonstrated that the ECR ion source generally can be used to produce mixed iron-fullerene plasma and FeC_{60} molecules both in the plasma and in the beam.

These results are encouraging, but at lower frequencies and with larger plasmas we expect to achieve better results. Very recently we replaced our 14.5GHz/2000W klystron based microwave generator by a variable 8-12GHz/20W TWT system. So far we studied He and Ar plasmas with this device, the investigation of fullerene plasmas follows at the beginning of 2005. Another project in the near future is the application of other methods (e.g oven) to produce the Fe component of the plasma.

a) Nat. Inst. Rad. Sci. Sci. (NIRS), Chiba, Japan

[1] S. Biri et al., Rev Sci. Instrum. 73 (2002) 881-883.

[2] S. Biri et al., Proc. 16th Int. Workshop on ECR Ion Sources, Berkeley, USA, 26-30 Sept. 2004. Will be published by AIP, Feb. 2005.

7.13 Determination of charge carrier trapping times in Si(Li) X-ray detectors

G. Kalinka, M. Novák

In high quality Si(Li) X-ray detectors the influence of charge trapping is usually negligible. Recently, however, in order to thoroughly characterize two liquid nitrogen cooled Si(Li) detectors a sensitive measurement of charge carrier trapping times have been performed.

The determination was based on the the bias dependence of the charge collection efficiency for a wide energy range of photons incident on one side, whereby the fractional contribution of the charge carriers in the collection process is varied, enabling to determine trapping data for both carriers simultaneously [1].

On the basis of the high degree of Li^+-compensation as checked by C-V measurents, nearly uniform electric fields in the applied 100-1000 V bias range for both detectors were assumed. At the same time the low temperature and the $\sim$ 5 mm detector thicknesses provide transit times much shorter (30-100 ns) than the peaking times applied (40-50 μs), therefore the influence of ballistic deficit was neglected, and so was the detrapping due to the intense cooling, independent of the long shaping. Despite the constancy of detector capacitances, nonnegligible bias dependent gain changes were corrected for by a reference pulser.

With the above assumptions and for low charge collection loss, which was the case here, the collection efficiency η can be written in the following linear approximation

$$\eta(U_d, E_x) \approx 1 - w \left[\frac{F_0'(E_x)}{\tau_e^+ v_e(U_d)} + \frac{L_0'(E_x)}{\tau_h^+ v_h(U_d)} \right],$$

where w is the depleted region thickness, τ_e^+ and τ_h^+ are the trapping times sought, v_e and v_h are the charge collection velocities, U_d is the applied bias voltage, E_x the energy of the photon detected, F_0' and L_0' are first order series expansion terms for electrons and holes, respectively, characterizing their contribution to the total charge carrier collection efficiency.

The positions of 9 major peaks in the 6-60 keV region were determined by spectrum fitting, using the MEWA interactive spectrum evaluation code [2]. Fortuitously, in the particular temperature and electric field strength region $v_e \sim 2.3 v_h$, so the originally 2D fitting problem of Eq. can be reduced to 1D, as can be seen in the figure. Charge carrier velocities at the estimated ~90 K temperature were taken from [3].

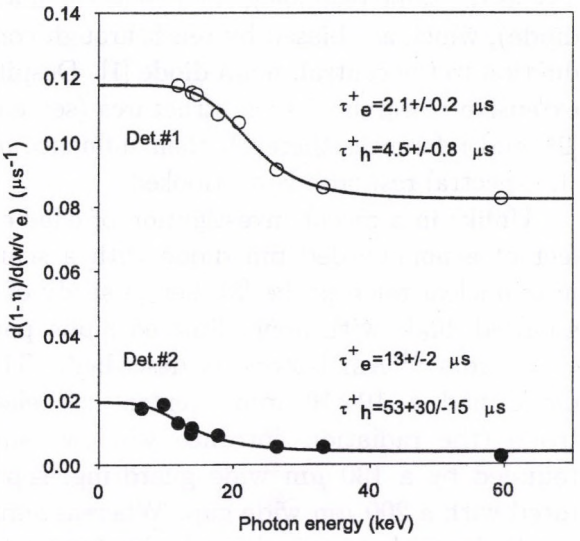

Note that for the better quality detector (♯2) at 1000 V the mean free pathlengths before trapping $\tau_i^+ v_i$ are in the order of 1 m for electrons and holes alike, while the charge losses are 0.12 % and 0.06 % in the low ($E_x \rightarrow 0$) and high ($E_x \rightarrow \infty$) energy limits, respectively. For 60 keV this translates to 36 eV deficit, or corresponds to 1 channel at the 1700th one in a MCA spectrum.

The advantage of the method applied is that it comes as a spin-off of a "simple" bias dependent energy calibration procedure of X-ray detectors [4].

[1] G. Kalinka, ATOMKI Bulletin 21 (1979) 291

[2] J. Végh, ECASIA '95, Wiley, 1996, p.680

[3] C. Jacoboni et al, Solid-State Electr. 20 (1977) 77

[4] M. Novák, Diploma Thesis, Debrecen University, 2004

7.14 Edge effect in single floating field ring terminated silicon pin diode

G. Kalinka, M. Novák

In order to ensure uniform and highly efficient charge collection in semiconductor radiation detectors, the vital requirement for high performance, they are operated at the highest bias they can withstand without significant increase of leakage current or without breakdown. An efficient solution to improve high voltage behavior and increase the breakdown voltage is the application of one or more concentric floating guardrings (manufactured usually in the same technological step as the main diode), which are biased by reachthrough conduction to the central, main diode [1]. Despite extensive research of such structures (see e.g. [2], and references therein), their influence on the spectral response is overlooked.

Unlike in a recent investigation of edge effect of a nonguarded pin diode with a scanning nuclear microprobe [3], here a study of a guarded diode with noncollimated alpha particles from ^{241}Am isotope is described. The diode had a 10×10 mm^2 central p^+ electrode (the radiation entrance window) surrounded by a 130 μm wide guardring, separated with a 200 μm wide gap. Whereas similar diodes without guardring broke down typically slightly above 200 V, the particular one tested withstood in excess of 500 V.

Uniform irradiation with the 5.5 MeV alpha particles at 250 V and using semigaussian shaping with 400 ns time constant resulted in the spectrum shown in the figure. Below reachtrough voltage (~150 V) spectra consist of only peak P_0, originating from the central, uncovered diode part, and P_1, from the rim of the centre, the metallization (~ 1 μm Al) of which causes the observed energy shift and straggling. The intensity of P_0 and P_1 slowly increases with the increase of the bias applied to the central part, as the depleted region extends not only in depth, but laterally too. At reachthrough their intensities drop back a little bit, as from now on the guardring and the centre share those events being detected between them. In addition, there appear two new peaks, P_2 and P_3, stemming from the uncovered and metallized parts of the extended depleted zone, belonging to the attraction region of the guardring. These peaks are further downshifted with respect to P_0 and P_1, since the ring is only loosely coupled to the centre via their interelectrode capacitance $C_{G,C}$ and an effective reachthrough resistance R_{RT} [4], causing remarkable ballistic deficit at the short shaping time used.

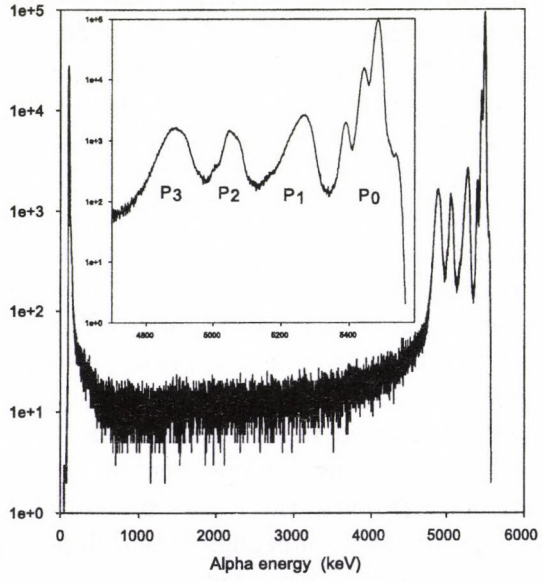

Risetime spectra taken simultaneously by measuring CFD signals with TAC clearly show slow pulses from the ring region. Surprising though at first, with increasing bias the risetime, and consequently the separation of P_2 and P_3 from P_0 and P_1 also increases, in accord with the above model. In order to eliminate P_2 and P_3 as artefacts, the guardring has to be capacitively grounded.

[1] J. Baliga, Power Semiconductor Devices, PWS Publishing, Boston, 1995

[2] M. Da Rold, *et al.*, IEEE Trans. Nucl. Sci. NS-46 (1999) 1215

[3] A. Simon, G. Kalinka, this Annual Report (Investigation of charge collection in a Silicon PIN photodiode)

[4] A. Castoldi *et al.*, Nucl. Instrum. and Methods A439 (2000) 483

7.15 A time-of-flight electron spectrometer for studies of forward electron emission in ion-atom collisions

L. Sarkadi, A. Orbán

We designed and constructed a new kind of time-of-flight electron spectrometer for measurements of the spectra of electrons emitted in forward direction in ion-atom collisions. The principle of operation of the spectrometer is shown in Figure 1. The electrons ejected in a small angular range (typically $\pm 1°$) around 0° from a gas jet target by a well-collimated ion beam (diameter: 0.5 mm) are reflected by an electrostatic mirror in backward angles. The angle between the normal of the mirror and the direction of the ion beam is 10°, so the angle of the backscattering is 160°. The backscattered electrons are detected by an array of channel electron multipliers (CEMs) mounted at a distance of about 30 cm from the mirror. The detector array consists of four CEMs allowing the measurement of the angular distribution of the electrons. Choosing a pair of CEMs, one can also carry out electron-electron coincidence measurements. The time of flight of the electrons is measured by detecting the electrons in coincidence with the charge-state analysed outgoing projectiles.

The electrostatic mirror consists of eight electrodes. The optimal electrode potentials were determined by calculating the electron trajectories with help of the SIMION program. To avoid the production of secondary electrons, we did not use any grid in the mirror.

The spectrometer was tested by C^+ on Ar collisions in the impact energy range between 100 and 300 keV. A typical velocity spectrum taken by 200 keV C^+ ions is shown in Figure 2. The electrons were detected in coincidence with the outgoing C^{2+} ions. The broad peak at $v = 0.81$ a.u. (electron energy = 9.08 eV) is the "Electron Loss to the Continuum" cusp. [1]. The narrower peaks located symmetrically on the low- and high-velocity wing of the cusp are autoionization lines originating from the projectile. The time resolution of the spectrometer (determined from the width of the autoionization lines) is about 6 ns.

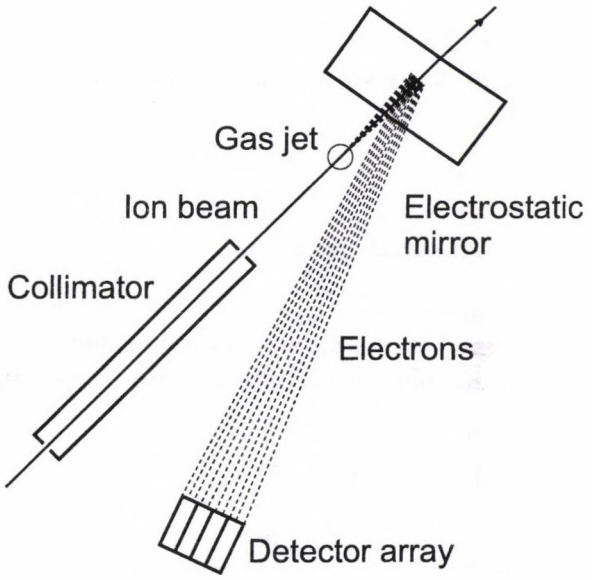

Figure 1. Scheme of the time-of-flight electron spectrometer.

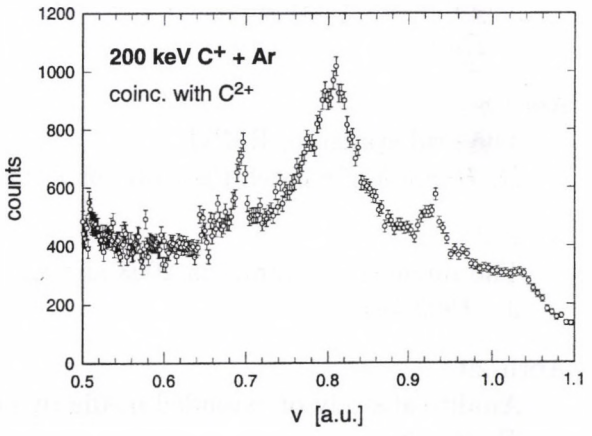

Figure 2. Velocity spectrum of the electrons emitted from 200 keV C^+ on Ar collisions at 0°.

[1] L. Víkor et al., *Nucl. Instr. Meth.* B **107**, 79 (1996).

8.1 Hebdomadal Seminars

January 8
Beyond Skyrme mean-field: Why and How
P.-H. Heenen (Universite Libre de Bruxelles)

January 15
Controlled nuclear fusion research: status and perspectives
S. Zoletnik (Research Institute for Particle and Nuclear Physics /RMKI/, Budapest)

January 29
Beta decay studies using total absorption spectroscopy
A. Algora

March 18
Pions in the neutron skin
A. Krasznahorkay

March 23
Quantum mechanics: a picturesque approach to the nonpicturesque
F. Károlyházy (Eötvös Loránd University /ELTE/, Budapest)

March 26
State of affairs
R.G. Lovas

March 30
Powell and the discovery of π meson; the present status of meson physics
T. Toró (Temesvár, Romania)

April 1
Angular distribution of photo electrons of Xe- and Ar-atoms
S. Ricz

April 8
The grid system of RMKI
D. Horváth (Research Institute for Particle and Nuclear Physics /RMKI/, Budapest)

April 27
The finances of Atomki in 2003 and the budget for 2004
M. Pálinkás

April 29
Analitical study of extended media by neutrons
B. Király

May 6
Are physical constants constant?
A. Csótó (Eötvös Loránd University /ELTE/, Budapest)

May 20
Influence of H_2- and D_2-molecules on the lifetime of antiprotonic He-atoms
B. Juhász

May 27

Ede Teller and the Hungarian secondary school
Gy. Radnai (Eötvös Loránd University /ELTE/, Budapest)

June 3

Renormalization group theory of cultural evolution
G. Fáth (Research Institute for Solid State Physics and Optics /SZFKI/, Budapest)

June 10

Mofette: a carbon dioxide spa in the Mátra Hills, Hungary
I. Csige

June 15

Reports of young scientists
Zs. Kertész, D. Novák, A. Orbán, L. Rinyu

September 9

Shedding light on nuclear structure with AFRODITE
S. Mullins (iThemba LABS, South Africa)

September 28

Study of the microscopic mechanisms of atomic movements in thin films or superficial regions of solids using isotopic tracing and Ion Beam Analysis. Retrospection and prominent results
G. Amsel (Université Pierre et Marie Curie and FNRC, Paris)

October 7

Energy from vacuum
P. Hraskó (University of Pécs /PTE/, Pécs)

October 14

Developments in Nuclear Reaction Analysis and interdisciplinary investigations with ion beam methods
G.Á. Szíki

October 19

New developments in hadron spectroscopy
F. Csikor (Eötvös Loránd University /ELTE/, Budapest)

October 21

Magnetic and electric properties of $Eu_{0.8}Sr_{0.2}CoO_3$ perovskite
J. Hakl

October 28

'Unreadness'
L. Zolnai

November 2

Has the quark-guon plasma been discovered?
I. Lovas (University of Debrecen)

November 4

Hunt for axions
A. Krasznahorkay

November 25

Coulomb displacement of neutron rich light nuclei
Á. Kiss (Eötvös Loránd University /ELTE/, Budapest)

December 2

Study of light exotic nuclei by radioactive ion beams
Z. Elekes

December 9

Introduction of new colleagues in Atomki
Á. Bihari, H. Czédli, É. Fekete, G. Katona, G. Kiss, M. Novák

December 16

Martians in radiation danger
I. Csige

8.2 List of Publications

The list of the Institute's publications can be found on-line at:

http://www.atomki.hu/PH/years/yea02004.htm

Contents

Author index